Development of a System for Testing Grid-Connected Doubly Fed Induction Generators with Implementation of a Three-level Neutral-Point-Clamped Converter

Prepared by:

Name: **Xiao Ming Hu**

Student Number: **HXXXIA001**

Supervised by:

A/Prof Azeem Khan

Dissertation submitted to the Department of Electrical Engineering, University of Cape Town, in complete fulfilment of the requirements for the degree of Master of Science in Electrical Engineering

October 2017

Department of Electrical Engineering

Faculty of Engineering & the Built Environment

University of Cape Town

Declaration

This dissertation is submitted to the Department of Electrical Engineering, University of Cape Town, in complete fulfilment of the requirements for the degree of Master of Science in Electrical Engineering. It has not been submitted before for any degree or examination at this or any other university.

I know the meaning of plagiarism and declare that all the work in the document, save for that which is properly acknowledged, is my own. This thesis/dissertation has been submitted to the Turnitin module (or equivalent similarity and originality checking software) and I confirm that my supervisor has seen my report and any concerns revealed by such have been resolved with my supervisor.

Signature: …… Signed by candidate ……

Date: ……19/02/2018……

EBE Faculty: Assessment of Ethics in Research Projects

Any person planning to undertake research in the Faculty of Engineering and the Built Environment at the University of Cape Town is required to complete this form before collecting or analysing data. When completed it should be submitted to the supervisor (where applicable) and from there to the Head of Department. If any of the questions below have been answered YES, and the applicant is NOT a fourth year student, the Head should forward this form for approval by the Faculty EIR committee: submit to Ms Zulpha Geyer (Zulpha.Geyer@uct.ac.za; Chem Eng Building, Ph 021 650 4791). Students must include a copy of the completed form with the thesis when it is submitted for examination.

Name of Principal Researcher/Student: Xiao Ming Hu Department: Elec Eng

If a Student: Degree: Msc Elec Eng Supervisor: Prof M.A. Khan

If a Research Contract indicate source of funding/sponsorship:

Research Project Title: Development of a grid-connected wind energy system.

Overview of ethics issues in your research project:

Question 1: Is there a possibility that your research could cause harm to a third party (i.e. a person not involved in your project)?	YES	(NO)
Question 2: Is your research making use of human subjects as sources of data? If your answer is YES, please complete Addendum 2.	YES	(NO)
Question 3: Does your research involve the participation of or provision of services to communities? If your answer is YES, please complete Addendum 3.	YES	(NO)
Question 4: If your research is sponsored, is there any potential for conflicts of interest? If your answer is YES, please complete Addendum 4.	YES	(NO)

If you have answered YES to any of the above questions, please append a copy of your research proposal, as well as any interview schedules or questionnaires (Addendum 1) and please complete further addenda as appropriate.

I hereby undertake to carry out my research in such a way that

- there is no apparent legal objection to the nature or the method of research; and
- the research will not compromise staff or students or the other responsibilities of the University;
- the stated objective will be achieved, and the findings will have a high degree of validity;
- limitations and alternative interpretations will be considered;
- the findings could be subject to peer review and publicly available; and
- I will comply with the conventions of copyright and avoid any practice that would constitute plagiarism.

Signed by:

	Full name and signature	Date
Principal Researcher/Student: Xiao Ming Hu	Signed by candidate	02/02/2015

This application is approved by:

Supervisor (if applicable):	Signed by candidate	02/02/15
HOD (or delegated nominee): Final authority for all assessments with NO to all questions and for all undergraduate research.	Signed by candidate	5/2/15
Chair : Faculty EIR Committee For applicants other than undergraduate students who have answered YES to any of the above questions.		

Acknowledgements

I would like to give a sincere thank you to my supervisor A.Prof. M.A Khan for his guidance, understanding and financial support throughout the duration of my master's degree.

A special token of gratitude go to Mr. C. Wozniak and Mr. P. Titus for your technical support in the laboratory. Their vast well of practical experiences are truly astounding and without it I would not have been able to complete my dissertation in due time.

Many thanks go to Mrs. S Sabodien, for taking care of all the administrative work.

Acknowledgements are also due for the lab technicians who helped me in the construction of my project.

To my fellow members of the AMES group, especially AK, Dr. Dehnavifard, Malao and Darren, thank you for your company throughout the years. Your friendship are highly valued and appreciated.

Finally, I would like to thank my family and friends for your continued support and understanding during my studies. Without all of you, it would have been a lonely journey to the finishing line, so with all of my heart, thank you.

Abstract

Consistent international efforts have been made over the past few decades to move the world towards an environmentally sustainable society. Wind energy conversion systems (WECSs) are one of the largest contributors within this movement. Furthermore amongst existing wind turbine power generation technologies, the doubly fed induction generator (DFIG) has been distinctively popular for its lower capital costs especially in higher power applications. In order to study the integration of this type of generator into the grid, a laboratory based DFIG test rig was developed where its complete design process is presented in this dissertation.

Mathematical modelling of related system components were thoroughly investigated so as to facilitate controller design based on the internal model control (IMC) methodology. In addition, a complete soft grid synchronisation procedure for the DFIG was investigated. It was found that the application of active damping within the IMC control law resulted in reduced stator current transients during synchronisation.

Control voltage excitation for the DFIG rotor circuit was achieved by the implementation of two voltage source converters (VSC's) connected in a back-to-back configuration via a common DC-link. The rotor-side converter (RSC) was responsible for regulating the machine speed whereas the grid-side converter (GSC) was responsible for regulating the DC-link voltage. In addition, these converters provided decoupled and bidirectional power flow control which enabled the DFIG to operate at sub synchronous and super synchronous speeds. A three-level VSC was chosen for the GSC control, where a resource conservative modulation algorithm that eliminates DC-link neutral voltage unbalance was implemented.

The DFIG system design was simulated, and the results were verified through experimental tests performed on a 1.5kW wound rotor induction machine (WRIM). A detailed description of the laboratory setup of the DFIG is presented, and various practical limitations are discussed.

It was found that the performance of the developed DFIG test rig correlated well with results of the simulations. Stable operation was achieved for various system test conditions, which indicated the system's robustness to serve as a practical platform for future DFIG related research.

Table of Contents

List of Figures

List of Tables

List of Symbols

T_a - Aerodynamic torque

P_a - Aerodynamic power

V_w - Wind velocity

β - Turbine blade pitch angle

ρ - Air density

R - Turbine blade radius

C_p - Maximum power coefficient

λ - Tip speed ratio

V_H - Hub-height wind speed

α_w - Empirical wind shear exponent

H - Hub height

J - Rotor inertia

T_e - Electromagnetic torque

$\vec{V}_s, \vec{V}_r$ - Stator and rotor supply voltage space vector

$\vec{E}_s, \vec{E}_r$ - Stator and rotor induced voltage space vector

$\vec{I}_s, \vec{I}_r$ - Stator and rotor current space vector

R_s, R_r - Stator and rotor resistance

L_{ls}, L_{lr} - Stator and rotor leakage inductance

ω_s - Stator voltage and current electrical angular frequency

ω_m - Rotor mechanical angular speed

ω_r - Rotor electrical angular speed

P_p - Machine pole pairs

ω_{slip} - Rotor voltage and current electrical angular frequency

s - Machine slip

θ_m - Rotor mechanical angular position

k_s, k_r - Stator and rotor winding factor

N_s, N_r - Number of turns on stator and rotor windings

f_s, f_r - Stator and rotor electric frequencies

$\vec{\phi}_m$ - Magnetizing flux space vector

P_s, Q_s - Stator active and reactive power

P_r, Q_r - Rotor active and reactive power

a_s, b_s, c_s - Stator natural reference frame axis

a_r, b_r, c_r - Rotor natural reference frame axis

α, β - Stationary reference frame axis

d_s, q_s - Synchronous reference frame axis

θ_s - Synchronous angle

θ_g - Grid angle

θ_r - Rotor electrical angle

θ_{slip} - Rotor slip angle

I_{sd}, I_{sq} - Stator dq-axis current

I_{rd}, I_{rq} - Rotor dq-axis current

V_{sd}, V_{sq} - Stator dq-axis voltage

V_{rd}, V_{rq} - Rotor dq-axis voltage

$\vec{\phi}_s^{\,e}, \vec{\phi}_r^{\,e}$ - Stator and rotor flux space vectors

R_s - Stator resistance

R_r - Rotor resistance

L_m - Magnetizing inductance

L_s - Stator synchronous inductance

L_r - Rotor synchronous inductance

$\dot{E}_g$ - GSC output voltage

$\dot{V}_g$ - Grid voltage

$\dot{I}_g$ - Grid current

L_g - Grid filter inductance

R_g - Grid filter parasitic resistance

ω_g - Grid electrical angular frequency

I_{gd}, I_{gq} - Grid dq-axis current

V_{gd}, V_{gq} - Grid dq-axis voltage

W_{dc} - Energy stored in DC-link capacitor

V_{dc} - DC-link voltage

C_{dc} - DC-link capacitance

ω_n - Natural frequency

ζ - Damping ratio

t_s - Settling time

t_r - Rise time

t_p - Peak time

$\%OS$ - Percent overshoot

k_p - Proportional gain

k_I - Integral gain

R_a - Active damping gain

T_{samp} - Sampling time

α_r - Rotor current control bandwidth

α_ω - Speed control bandwidth

α_g - Grid current control bandwidth

α_{dc} - DC voltage control bandwidth

m_a - Modulation index

List of Abbreviations

DFIG	- Doubly fed induction generator
IMC	- Internal model control
VSC	- Voltage source converter
RSC	- Rotor side converter
GSC	- Grid side converter
WRIM	- Wound rotor induction machine
WECS	- Wind energy conversion system
REIPP	- Renewable energy independent power producer
PMSG	- Permanent magnet synchronous generator
SVPWM	-Space vector pulse width modulation
SPWM	- Sinewave pulse width modulation
MPPT	- Maximum power point tracking
FOC	- Field oriented control
BEM	- Blade Element Momentum
PI	- Proportional Integral
PLL	- Phase locked loop
EMF	- Electromotive force
NPC	- Neutral point clamped
NTV	- Nearest three vectors
FPGA	- Field programmable gate array

1. Introduction

1.1 Background

The projected shortage of fossil fuels and environmental concerns has placed renewable energy sources under increasing attention as a sustainable alternative for fulfilling global energy needs. By the end of 2016, 19.3% of the global energy consumption was provided through renewable means [1]. Electricity production from renewable sources exceeded 2000GW worldwide where wind energy stands as the third largest contributor with a global installed capacity of 487GW. Figure 1-1 below details all renewable energy capacities around the globe between 2015 and 2016 [1].

		2015	2016
Investment			
New investment (annual) in renewable power and fuels[1]	billion USD	312.2	**241.6**
Power			
Renewable power capacity (total, not including hydro)	GW	785	**921**
Renewable power capacity (total, including hydro)	GW	1,856	**2,017**
Hydropower capacity[2]	GW	1,071	**1,096**
Bio-power capacity	GW	106	**112**
Bio-power generation (annual)	TWh	464	**504**
Geothermal power capacity	GW	13	**13.5**
Solar PV capacity	GW	228	**303**
Concentrating solar thermal power capacity	GW	4.7	**4.8**
Wind power capacity	GW	433	**487**

Figure 1-1: Global renewable energy status at the end of 2016 [1]

The 55GW growth of wind power capacity from 2015 to 2016 resulted in a gross international investments of about USD 112.5 billion. This multi-billion dollar industry has continuously provided direct or indirect job opportunities, which has stimulated economic growth in many countries. That being said, the capital costs for WECS's has been declining over the past decade. Key reasons for the improvements in economic viability of WECS's include various government incentive programs and technological advancements [2].

South Africa's energy mix has traditionally been dominated by coal, which is solely sourced by Eskom, a state run utility. As a result, South Africa has been ranked as the 19th largest global CO_2 emitter according to a study conducted for the period between 1970 and 2013 shown in Figure 1-2 below [3].

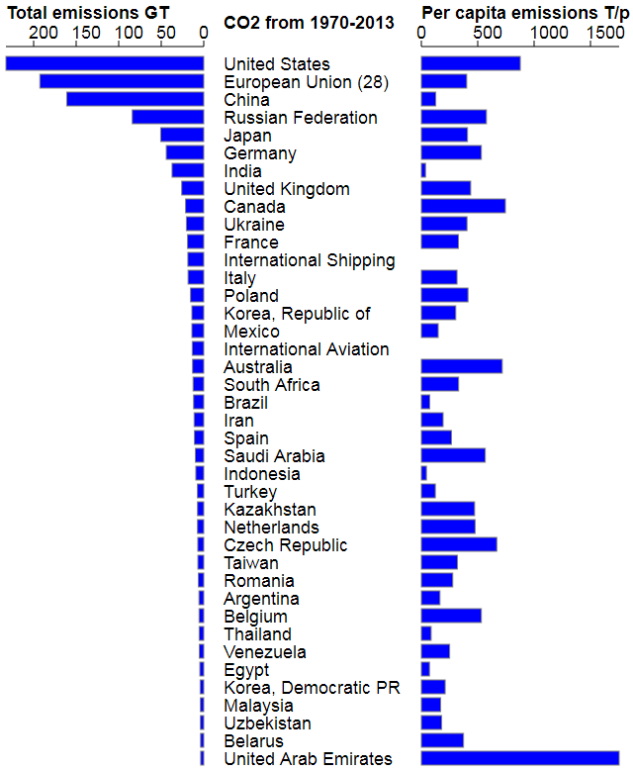

Figure 1-2: Global CO_2 emission ranking for the period between 1970 – 2013 [3]

Due to national power demand reaching the limit of its supply capacity at the end of 2008, the Independent Power Producer (IPP) programme was legislated by the government of South Africa in 2010. The bill has created a competitive environment in which the Department of Energy could procure power generated by private entrants to the market. This decision was motivated by the need to increase and diversify SA's energy mix whilst attracting local and foreign investments. Within the IPP programme, major emphasis has been placed on the renewable energy IPP (REIPP) sector in order to reduce coal usage. The national renewable energy target is set for 18800MW generating capacity to be achieved by 2030 [4].

Wind energy plays a major role in the current renewable segment of SA's energy mix. This is largely due to its associated technologies being less costly compared to other renewable energy systems such as hydro and solar. Furthermore, South Africa has large coastal regions as well as high lying areas with wind sources where abundant energy may be extracted. The percentage share for wind energy in SA's power mix by 2030 is estimated to be 9.47% shown in Figure 1-3 below [5].

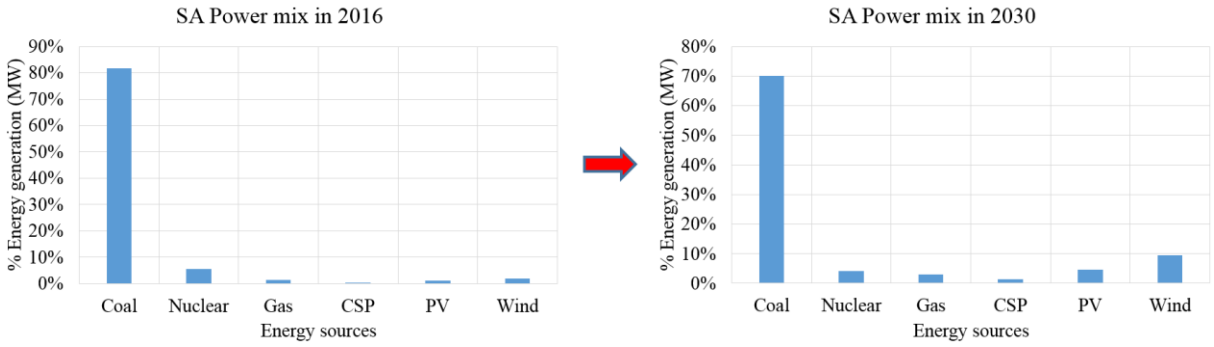

Figure 1-3: SA power mix in 2016 VS estimated power mix in 2030

Wind power generation in South Africa is estimated to grow by 7.63% within the next decade from the current capacity of 1.84%. This shows some commitment by government to integrate renewable energy into the grid. This will result in an appreciable reduction in fossil fuel based electricity generation sources.

Although wind energy utilisation has obvious advantages, its implementation is not without challenges due to its intermittent nature. Wind energy is constantly varying and dependent on the weather, therefore the grid to which it is integrated must be flexible to ensure optimal power transmission. Such a task often requires complex control systems to be put in place to regulate the varying energy supply. Additional issues for WECS's can be attributed to non-ideal operating conditions associated with this type of system, which include: grid faults, equipment degradation and wind turbulences etc.

When the above mentioned issues are considered, and taking cognisance of South Africa's interest in wind energy, a system that can emulate large-scale WECS's within a controlled laboratory environment can be beneficial for investigating related issues experienced in the industry. This is the motivation behind various research projects undertaken by the Advanced Machines and Energy Systems (AMES) group at the University of Cape Town.

In particular, the contribution of this dissertation will produce a DFIG test rig, which will add to various existing WECS's developed by predecessors within the AMES research group. The resulting laboratory system will provide a robust platform for future studies on DFIG related issues for wind energy applications.

1.2 Literature Review

A brief review of literatures related to the development of a DFIG system is presented in this section. The concepts are discussed further in chapters 2, 3, 4 and 5.

Energy is extracted from the wind by means of a turbine coupled to a generator. In particular the turbine blades capture kinetic energy from the wind which drives the generator resulting in electrical energy output [6]. WECS can be categorised into two groups, namely constant speed turbines and variable speed systems. The main difference between these two WECS types is the manner in which aerodynamic power is captured by the turbine rotor. The aerodynamic efficiency of a wind turbine is dependent on

the ratio of rotor speed to wind speed. Therefore in order to achieve maximum wind energy capture, the rotor speed should be varied accordingly with respect to the incident wind speed. This is a feature exclusively seen in variable speed wind turbines thus making it a more attractive option for WECS applications [7].

Two variable speed wind turbine topologies, namely permanent magnet synchronous generator (PMSG) and the doubly fed induction generator (DFIG), are widely applied in industry. For the PMSG a full-scale power converter is required for connecting stator windings of the machine to the grid. For the DFIG its stator windings are directly connected to the grid, whilst its rotor windings are brought out by slip rings which are then connected to the grid via a partially-rated converter [7], [8]. The advantages and disadvantages for both of these topologies are listed in Table 1-1 below [7]–[9].

Table 1-1: Advantages and disadvantages between PMSG and DFIG

Variable speed wind turbine topology	Advantages	Disadvantages
PMSG	• Can achieve wider range of speed control • Do not need slip rings therefore less maintenance are needed • Associated Control scheme is relatively simple to implement	• The generator construction require permanent magnets which complicates its design and results in increased costs • The need for full-rated power converters introduce higher switching losses and also increase capital costs for the system • Demagnetisation of magnets may occur at high temperature
DFIG	• The construction of a WRIM is simpler and cheaper than that of the PMSG • The generator can be controlled via its rotor at a much lower power rating resulting in reduced converter and filter costs • Has improved efficiency with respect to converter losses	• Need slip rings to access rotor windings leading to the need for frequent maintenances • Has limited range for speed variations typically rated around ±25% of the machine synchronous speed • Associated control scheme is complex when compared to that of the PMSG

As a result of these characteristics, the PMSG is usually considered for low to medium power applications where the DFIG provides attractive solutions for high power wind turbine applications in the MW range. For the work presented in this dissertation the focus will be exclusively on the DFIG where details about its control and operations are investigated.

The control for a wind turbine driven DFIG can be separated into three levels in ascending order of superiority as: (1) generator control, (2) Turbine control, (3) Operator control [10]. Each control level provides operating references for the level directly below thus forming a cascaded hierarchy. Level (3) is dedicated to dealing with grid integration issues whereas level (2) focuses on power optimisation for the DFIG wind turbine. Level (1) can be seen as the most complex control layer as it is responsible for achieving proper component level operations such as speed and power factor control. Work presented in this dissertation is dedicated to achieving a robust generator control design for a DFIG wind turbine hence allowing higher control levels to be implemented in the future.

The DFIG can be controlled, at the generator level, using well-known space vector principles where its decoupled active and reactive power regulation can be achieved [11]–[13]. Various alternative control strategies have been proposed in literature such as direct torque control [14], [15], sensor-less control [16] and the model predictive algorithms based on non-linear control principles [17], [18]. However, the classical vector control scheme based on PI compensators with feed-forward decoupling is still predominantly used for its relatively simple implementation. The vector control is physically realised by the implementation of a back-to-back converter which connects the DFIG rotor windings to the grid. This controller can be separated into two subsystems, namely rotor side converter (RSC) and grid side converter (GSC) control.

The main challenge in the design of a DFIG vector controller is providing proportional and integral gain values for the PI compensator in order to achieve desired system response. Many tuning methodologies have been proposed so far, amongst them pole placement [12], [19] and internal model control (IMC) [20], [21] have received much attention due to their standard application to second-order closed loop dynamics. The IMC technique is much easier to realise in comparison with the pole placement method, thus it is adopted to tune the PI compensators. However, it has been shown that disturbance rejection for the closed loop system, resulting from IMC, display poor characteristics [22]. A method discussed in [23] for improving the IMC disturbance rejection, known as active damping, is thus implemented in the control law for better overall system performances.

The references produced by the controller must be converted to switching commands for the converter IGBT's so as to produce PWM averaged voltage excitations required for various system components. For this conversion task, the space vector pulse width modulation (SVPWM) algorithm has shown superior voltage utilization and harmonic distortion features when compared to the conventional sinewave pulse width modulation (SPWM) [24], [25]. However, SVPWM is computationally intensive

to implement and its complexity increases exponentially with number of levels within the converter. One of the objectives in this dissertation is to correctly implement a three-level voltage source converter (VSC) in the development for the DFIG system. A three-level SVPWM algorithm presented in [26] is adopted in this dissertation to achieve switching operations for the three-level VSC. This algorithm uses a novel vector projection method for duty cycle calculations which is extremely easy to implement using an embedded digital controller. In addition, the algorithm also provides a solution for dealing with DC-link voltage unbalance which is a common operating issue with a three-level VSC.

For a wind-turbine-driven DFIG, electrical connection and disconnection from the grid occurs frequently due to wind velocity exceeding or falling below its operating speed range. The inrush stator current during these re-connections to the grid should be kept below acceptable limits. Therefore, soft synchronization between the DFIG and grid is essential to avoid excessive stress on the mechanical drive train as well as the electrical circuits. Only a limited number of contributions have dealt with the importance of soft DFIG grid connection. The general solution, described in [27]–[33], produces an induced stator voltage equal to the grid voltage by adjusting rotor currents prior to synchronization, resulting in a low-impact connection to the grid. However the negative impact on DFIG synchronisation dynamics caused by mismatch in the controller feedforward terms has not been investigated in relevant literatures. This issue is discussed in detail in chapter 5.

1.3 Research objectives

The research objectives in this dissertation focuses on the development of a DFIG system and are listed below:

- Modelling of various components in a DFIG system so as to facilitate the controller design.
- Develop SVPWM algorithms for the back-to-back converters. In particular, the three-level SVPWM must be resource efficient and cater for DC-link voltage unbalance.
- Develop a soft synchronisation procedure for the DFIG with additional investigation into the effect of DFIG control for feedforward mismatch during synchronisation.
- The developed DFIG system must be simulated first and then validated experimentally in the laboratory.

1.4 Scope and Limitations

The project scope as well as limitations encountered during the experimental stage of this dissertation are listed below:

- A wound rotor induction machine and DC machine, available for this project was rated at 1.5kW.
- Due to mechanical constraints of the machines, the variable speed range for the DFIG is limited to ±20% of the synchronous speed.

- The physical implementation for the DFIG system uses existing equipment in the laboratory. Therefore system components are not optimised for the power rating of the machine. Those equipment includes the power converters and grid filters.
- The control design for the DFIG is limited to the generator level.

1.5 Dissertation Structure

The subsequent chapters in this dissertation are laid out as follows:

Chapter 2: The complete mathematical model for a DFIG system, including various components, is presented in this chapter based on fundamental principles. In addition, a brief discussion with respect to turbine maximum power point control (MPPT) is presented to provide insight into DFIG operating conditions.

Chapter 3: This chapter presents fundamental principles that are applied in this dissertation for the design of both RSC and GSC control system.

Chapter 4: SVPWM algorithms are presented in this chapter for both two-level and three-level voltage source converters. However, emphasis has been placed on the three-level case.

Chapter 5: A complete DFIG grid soft synchronisation procedure is provided in this chapter based on a modified rotor current controller. Various machine dynamics specifically related to the synchronisation period are investigated here.

Chapter 6: The components of the DFIG system are simulated in this chapter where observations are made on the results obtained.

Chapter 7: The laboratory setup for the DFIG implementation is described in this chapter with great detail. Some practical limitations encountered are discussed where corresponding variations in the system design are justified.

Chapter 8: Experimental results obtained from the DFIG laboratory implementation are presented in this chapter. Analysis performed on these results refers back to the simulated results in chapter 6, where a comparative validation for the physical system is presented.

Chapter 9: Conclusions and recommendations for possible future research using the developed system are presented here.

2. Modelling and Analysis of a DFIG based Wind Energy System

Proper system identification is essential for any type of controller design. The DFIG system consists of various components that exhibit different behaviours, therefore each subsystem must be analysed with care so as to enable smooth component interactions within the overall system.

This section details the theoretical analysis on the DFIG system. Mathematical models are derived for individual components in order to facilitate a proper controller design, as well as providing insight into system operational characteristics.

2.1 Overview of the DFIG wind energy system

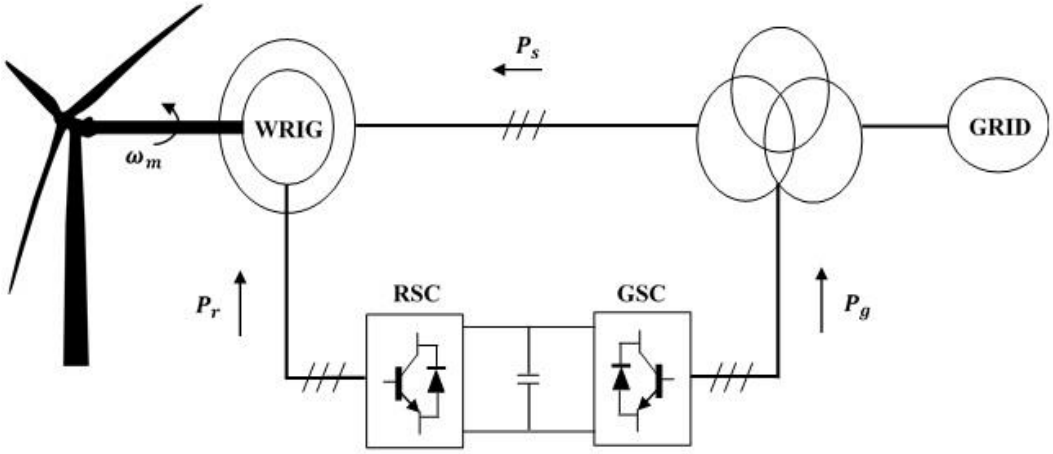

Figure 2-1: Typical DFIG system overview

Figure 2-1 presents the overview for a typical DFIG wind turbine system which can be separated into discrete subsystems discussed in the following subsections.

2.1.1 Mechanical drive-train

The mechanical system of the DFIG wind turbine includes the turbine blades and the turbine shaft connected to the generator rotor through a gear box. The shaft can be mathematically represented by a drive-train model that describes its rotational dynamics [34], [35]. For accurate mechanical transient analysis of the turbine-generator sub-system, the six-mass drive train has shown better results compared to reduced order models, such as the three, two and lumped-mass drive train [34]. With each reduced order, certain characteristics of the turbine are neglected. From a control design point of view, the lumped mass model sufficiently describes the shaft rotational characteristics therefore it is adopted in this dissertation.

The turbine aerodynamic characteristics should also be considered since it provides the fundamental understandings for achieving Maximum Power Point Tracking (MPPT) on the turbine energy output [36], [37].

2.1.2 Generator system

The generator, or DFIG, is actually a wound rotor induction machine, shown in Figure 2-1. This component converts the mechanical energy from the wind turbine to electrical energy that can be transferred to the grid. Its stator windings are connected directly to the grid. The rotor windings are accessed through slip rings and actively controlled by a bidirectional converter typically sized to 30% of the total system power rating. The converter must be capable of supporting the DFIG operating speed range from cut-in to rated wind speed [38].

The DFIG, although asynchronous in nature, can be controlled using the well-known field-oriented control principle (FOC) developed for synchronous machines, therefore achieving decoupled active and reactive power outputs [39], [40].

In normal operation, the stator always supply its power to the grid. The rotor power is injected into and drawn from the grid for super-synchronous and sub-synchronous speed operations respectively. It is important to note that the convention for positive power flow is extremely important for the controller design. In this dissertation a motoring convention is adopted i.e. positive power flow is towards the generator.

2.1.3 Converter and DC link

The bidirectional converter consists of two PWM controlled voltage-source converters (VSC) connected via a common DC-link. The rotor-side converter (RSC) is responsible for regulating the generator speed and apparent power, this is achieved by exciting the rotor windings with a variable voltage at the slip frequency ω_{slip}. The grid-side converter (GSC) is responsible for maintaining the DC-link voltage whilst regulating active and reactive power exchange with the grid. The frequency and magnitude of the GSC output voltage must be synchronized to the grid voltage [41], [42].

So far, the two-level converter with IGBT's is the most popular technology for variable speed drive applications, mainly due to its simple implementation and well understood characteristics. It has been shown that multilevel converters may provide better performances with respect to output voltage level and harmonics [43], [44]. However, their implementation complexity increases exponentially with increasing number of levels. A three-level NPC converter was chosen for implementation on the grid-side in this system.

2.1.4 Grid

The electrical connection between DFIG stator and the grid is assumed to be direct, therefore only the electrical connection between RSC and the grid is analysed in detail. In general, the grid-side system structure is quite similar between different the wind turbine topologies [45].

A step-up transformer is usually used to raise the generator output voltage to appropriate levels for transmission. For a laboratory scaled system this is not necessary, therefore it is neglected and a direct connection between generator and grid is considered.

A line filter must be placed at the output of the GSC to attenuate switching frequency harmonics. Popular filter topologies include the L-type [41], [42] and LCL-type [46], [47] where the latter has better attenuation properties in the higher frequency range, therefore reducing the size of inductors needed. For the DFIG system, an L-type filter is sufficient since the converters only need to handle a fraction of the system power therefore potential losses across the inductors can be regarded as negligible.

2.1.5 Overall control system

The control system does not form one of the physical aspects of the DFIG system, however it is just as important. The three layer control hierarchy described in [10] is shown in **Error! Reference source not found.** below.

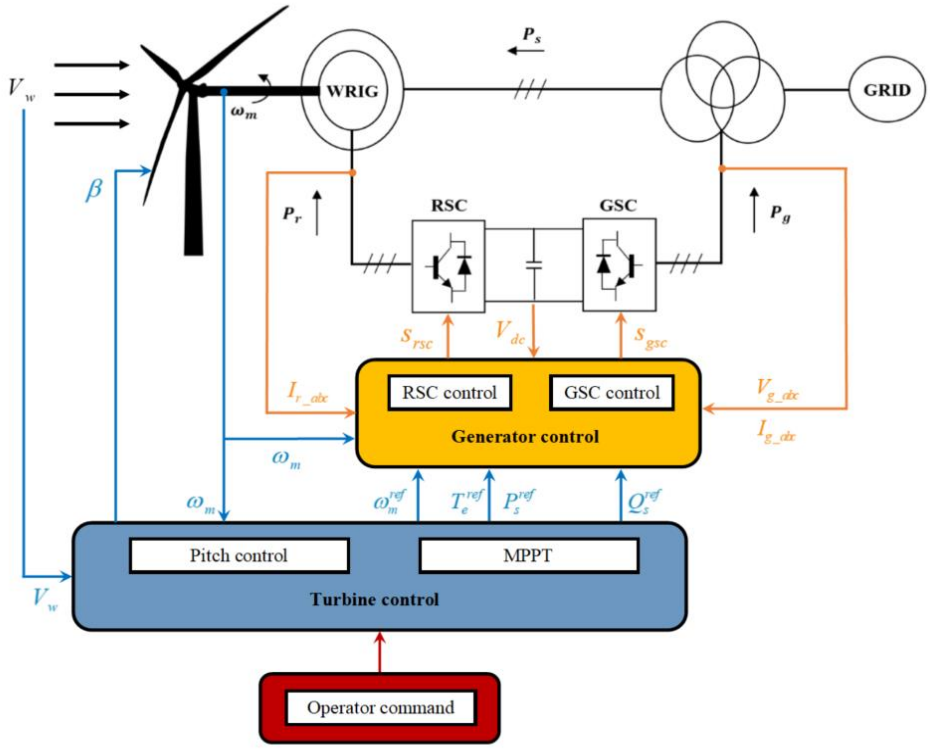

Figure 2-2: DFIG overall control system

Generator control influences immediate DFIG dynamics. This control level uses electrical and mechanical measurements from the machine as feedback signals. The output control signals are provided in terms of switching commands for the RSC and GSC, enforcing each converter to perform their respective tasks.

The generator control references are provided by the second tier turbine control, where a MPPT algorithm is usually followed to provide speed, torque or active power references [35]. Pitch angle

control is an additional feature of this control level, which alters turbine blade angles during high wind speeds so as to keep DFIG output power within rated conditions.

The top level operator command is dedicated for large-scale wind farm grid integration issues. Generally interaction between top level and the rest of the control system only occur if extra services, such as reactive power support, are required from the generator.

2.2 DFIG mechanical models

As discussed in section 2.1.1, the DFIG mechanical system consists of the aerodynamic and drive-train models. These are mathematically presented in this section.

2.2.1 Wind turbine aerodynamic model

The relationship between the turbine mechanical torque T_a, incoming wind speed V_w and blade pitch angle β can be represented by [35]:

$$T_a = \frac{\rho}{2}\pi R^3 \left(\frac{C_P(\lambda,\beta)}{\lambda} \right) V_w^2 \tag{1}$$

Where the power extracted from the wind can be described as:

$$P_a = \frac{\rho}{2}\pi R^2 C_P(\lambda,\beta) V_w^3 \tag{2}$$

The variables ρ, R, C_P, λ and β respectively represent the air density, turbine blade radius, maximum power coefficient, tip speed ratio and turbine blade pitch angle. The power coefficient C_P is a function of λ and β, and can be approximated for a three-bladed wind turbine using the following expressions [35]:

$$C_P(\lambda,\beta) = 0.22\left(\frac{116}{\lambda_i} - 0.4\beta - 5\right) e^{-\frac{12.5}{\lambda_i}} \tag{3}$$

$$\frac{1}{\lambda_i} = \frac{1}{\lambda + 0.08\beta} - \frac{0.035}{\beta^3 + 1} \tag{4}$$

The tip speed ratio λ is the ratio of blade circumferential speed to wind velocity expressed by [35]:

$$\lambda = \frac{\omega_m R}{V_w} \tag{5}$$

Expression (3)-(4) forms a numerical approximation method for C_P, which is sufficient to model the general characteristics of a wind turbine [48], [49]. A more complex method, based on Blade Element

Momentum (BEM), can be found in [50]. Using (3) the C_P characteristic for the wind turbine can be found for varying λ at different blade angle positions, this is simulated in Figure 2-3 below.

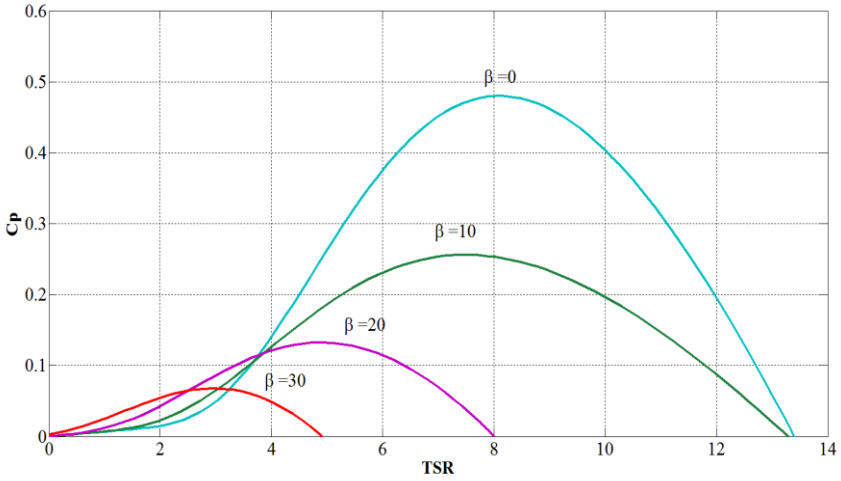

Figure 2-3: C_P vs λ for varying pitch angle

It is seen that for a pitch angle of 0, optimum power coefficient can be produced, which is analogous to optimal wind power extraction. This is a reasonable assumption for lower wind speeds where the effect of varying wind on the pitch angle is minimal. Equations (1) and (2) describes the behaviour of turbine aerodynamic torque and power due to various wind speeds. However, it does not include power pulsations often observed in a three-bladed wind turbine [37]. These pulsations may affect turbine control stability, and can be regarded as periodic processes characterised by two dominant effects:

- Wind shear
- Tower shadow

The wind shear phenomenon occurs due to the increase in wind speed at higher altitudes. Since the turbine blades rotate in a circular motion, each element experiences non-uniform wind field at any given position relative to the vertical axis of the turbine. Therefore turbine power and torque output displays periodic amplitude oscillations as each blade complete one cycle of rotation.

The presence of the tower affects the distribution of wind directly in front of the turbine tower. This effect is termed tower shadow. Since wind is redirected around the tower when the turbine blades reaches the tower, torque production is decreased at that point.

In [37], a model for simulating wind shear and tower shadow effects, based on the 'equivalent wind speed' concept, was developed. This model represents the actual spatial wind with an equivalent wind speed that allows for computation without radial dependence. The complete wind field model including the effects of wind shear and tower shadow is represented by the following equations [37]:

$$v_{eq}(t,\theta) = v_{eqo} + v_{eq_{ws}} + v_{eq_{ts}} \tag{6}$$

$$v_{eqo} = V_H \tag{7}$$

$$v_{eq_{ws}} = V_H \left[\frac{\alpha_w(\alpha_w - 1)}{8} \left(\frac{R}{H} \right)^2 + \frac{\alpha_w(\alpha_w - 1)(\alpha_w - 2)}{60} \left(\frac{R}{H} \right)^3 \cos(3\theta) \right] \tag{8}$$

$$v_{eq_{ts}} = \frac{mV_H}{3R^2} \sum_{b=1}^{3} \left[\frac{a^2}{\sin^2(\theta_b)} \ln\left(\frac{R^2 \sin^2(\theta_b)}{x^2} + 1 \right) - \frac{2aR^2}{R^2 \sin^2(\theta_b) + x^2} \right] \tag{9}$$

Equation (6) is the total wind field which can be decomposed into components as shown in (7)-(9) where $V_H, \alpha_w, H, R, a, x$ are the hub-height wind speed, empirical wind shear exponent, hub height, turbine radius, tower radius and distance between the blade origins to tower midline respectively. The normalised torque oscillations caused by wind shear and tower shadow can be expressed by the following equation [37]:

$$T_{a(oc)} = 1 + \frac{2}{mV_H} \left[v_{eq_{ws}} + v_{eq_{ts}} + (1-m)V_H \right] \tag{10}$$

Where m is the transformation coefficient between mean wind velocity and hub height wind. Using (6)-(10) the torque oscillations for a complete rotation of the turbine blades are simulated for a turbine with the following test specifications: $R = 20m$, $H = 40m$, $a_w = 0.3$, $a = 0.85$ and $x = 2.9m$. The results obtained are shown in Figure 2-4 below.

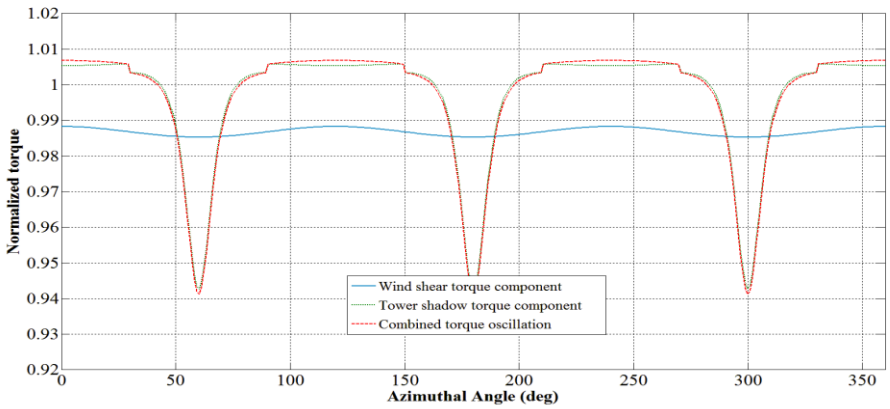

Figure 2-4: Normalized aerodynamic torque including effects of wind shear and tower shadow

Both wind shear and tower shadow causes the torque to oscillate three times per rotation which is expected for a three-bladed turbine. The effect of wind shear contributes much less towards torque pulsations compared to the effect of tower shadow. It can also be seen that the oscillations are most severe when one blade is pointed downwards, note the north-pole is considered to be at 0^o.

2.2.2 Turbine shaft

The lumped-mass model for the mechanical drive train is considered. Generally the higher order models are used for transient stability analysis, which is not required for the controller design [34]. The lumped-mass model for the DFIG can be expressed as:

$$J\frac{d\omega_m}{dt} = T_e - T_a \tag{11}$$

Equation (11) regards all inertias in the drive-train system as a single rotating mass, where all the mechanical quantities are referred to the turbine-side. The variables J, ω_m, T_e and T_a represents total shaft inertia, shaft angular mechanical speed, electromagnetic torque produced by the machine and aerodynamic torque defined in (1). It is important to say that (11) has been expressed using the motoring convention, thus a negative T_e or T_a represents generating torque.

2.3 DFIG electrical models

The DFIG can be simulated easily in MATLAB Simulink, where the standard Simscape block set includes common wind turbine generator models. Mathematical models describing the DFIG electrical dynamics are presented in this section to provide insight with respect to its operating principles.

2.3.1 Steady state model

The DFIG electrical circuit and the corresponding per phase steady state equivalent circuit are presented in Figure 2-5.

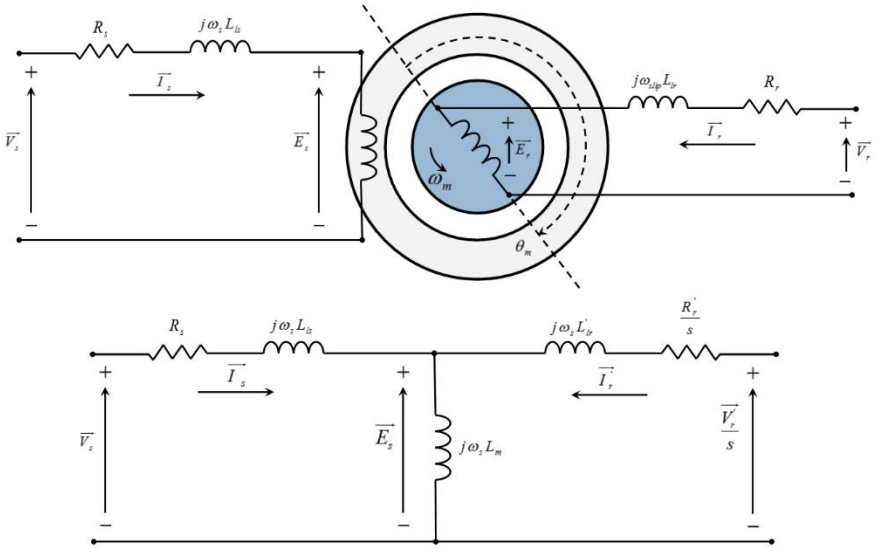

Figure 2-5: Per phase DFIG equivalent circuit

The magnetizing branch resistance is assumed to be very large as if it is an open circuit, therefore it is neglected. The parameters shown represent the following machine characteristics:

$\vec{V}_s, \vec{V}_r$ = Stator and rotor supply voltage space vector $[V]$

$\vec{E}_s, \vec{E}_r$ = Stator and rotor induced voltage space vector $[V]$

$\vec{I}_s, \vec{I}_r$ = Stator and rotor current space vector $[V]$

R_s, R_r = Stator and rotor resistance $[\Omega]$

L_{ls}, L_{lr} = Stator and rotor leakage inductance $[H]$

ω_s = Stator voltage and current electrical angular frequency $[rad/s]$

ω_m = Rotor mechanical angular speed $[rad/s]$

$\omega_r = \omega_m P_p$ = Rotor electrical angular speed $[rad/s]$ where P_p = machine pole pairs

$\omega_{slip} = \omega_s - \omega_r$ = Rotor voltage and current electrical angular frequency $[rad/s]$

$s = \dfrac{\omega_s - \omega_r}{\omega_s}$ = Machine slip [%]

θ_m = Rotor mechanical angular position $[rad]$

The induced voltages in the stator and rotor windings can be expressed by [51]:

$$\vec{E}_s = \sqrt{2}\pi k_s N_s f_s \vec{\phi}_m \left| \vec{V}_{s(rms)} \right| \tag{12}$$

$$\vec{E}_r = \sqrt{2}\pi k_r N_r f_r \vec{\phi}_m \left| \vec{V}_{s(rms)} \right| \tag{13}$$

Where

k_s, k_r = Stator and rotor winding factor

N_s, N_r = Number of turns on stator and rotor windings

f_s, f_r = Stator and rotor electric frequencies $[Hz]$

$\vec{\phi}_m$ = Magnetizing flux space vector $[Wb]$

By considering machine stand still condition, it can be approximated that $k_s \approx k_r$, therefore the induced stator and rotor voltages are related by the effective turns-ratio given by:

$$n = \frac{\vec{E}_s}{\vec{E}_r} = \frac{N_s}{N_r} \tag{14}$$

For the equivalent circuit shown in Figure 2-5, all the rotor quantities are referred to the stator windings using the following expressions:

$$\begin{aligned} \underset{\sim}{E}_r' &= \underset{\sim}{E}_s = \frac{\underset{\sim}{E}_r}{n} & R_r' &= \frac{R_r}{n^2} \\ \underset{\sim}{V}_r' &= \frac{\underset{\sim}{V}_r}{n} & L_{lr}' &= \frac{L_{lr}}{n^2} \\ & \underset{\sim}{I}_r' = n\underset{\sim}{I}_r \end{aligned} \tag{15}$$

For ease of presentation, prime superscripts used to represent referred rotor quantities will be neglected from this point onwards. All rotor quantities are to be assumed referred to the stator unless indicated otherwise. The steady state stator and rotor active power, in accordance to the motoring convention, are given by:

$$\begin{aligned} P_s &\cong T_e \frac{\omega_s}{P_p} \\ P_r &\approx -sP_s \approx -sT_e \frac{\omega_s}{P_p} \end{aligned} \tag{16}$$

Note P_r in (16) increases in proportion with the machine slip. If $s > 0$ (DFIG sub-synchronous operation) then the rotor power is positive, indicating current flow from grid to the machine. The opposite is true for $s < 0$ (DFIG super-synchronous operation). If $s = 0$ (DFIG synchronous operation), then there will be no power exchange between the grid and rotor.

2.3.2 Stationary and synchronous reference frame transformations

The steady state per-phase model described before does not reliably demonstrate machine characteristics under transient operating conditions. In order to formulate an appropriate dynamic model for the DFIG, the concept of stationary and synchronous reference frame transformations must be used [52]. The general concept is to present time-dependent three phase quantities with a rotating space vector in an arbitrary reference frame. The selection of the reference frame is dependent on application requirements. Relevant reference frames for the DFIG, superimposed on top of an induction machine cross section, are presented in Figure 2-6.

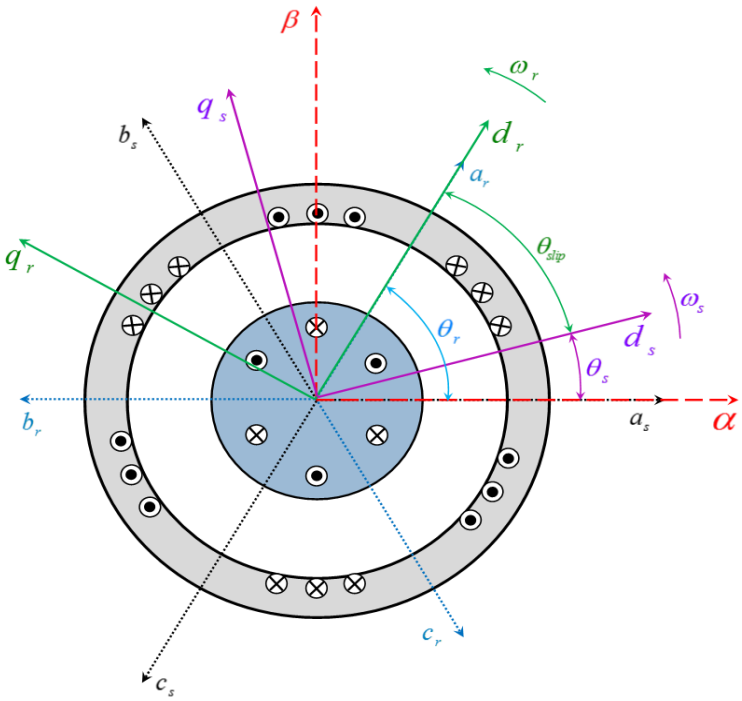

Figure 2-6: Reference frames of the DFIG

The stator and rotor windings are distributed in space by 120^o and assumed to have a single pole pair for simplified analysis. There are five reference frames which are listed below:

- Stator natural reference frame - a_s, b_s, c_s are the stator winding axis, defined as perpendicular to the plane where their respective stator coils are situated.
- Rotor natural reference frame - a_r, b_r, c_r are the rotor winding axis, defined as perpendicular to the plane where their respective rotor coils are situated. This reference frame rotates at the rotor electrical angular speed ω_r .
- Stationary reference frame - α, β are a set of orthogonal axis with α aligned to a_s .
- Rotor reference frame - d_r, q_r are a set of orthogonal axis where d_r is aligned with a_r . This reference frame also rotates at the speed ω_r .

- Synchronous reference frame - d_s, q_s are a set of orthogonal axis that rotates at the same angular speed as stator electrical space vectors.

The relative angular positions of the orthogonal rotating reference frames (i.e. d_r, q_r & d_s, q_s) with respect to the stationary axis are:

θ_s = Angle of the synchronous frame with respect to the stationary frame

$\theta_r = \theta_m P_p$ = Angle of the rotor frame in electrical radians with respect to the stationary frame

And with respect to each other:

$\theta_{slip} = \theta_s - \theta_r$ = Slip angle of the DFIG in electrical radians

Consider a set of balanced three phase stator currents in the natural reference frame presented by:

$$\begin{aligned} I_{sa}(t) &= \hat{I}_s \cos(\omega t) \\ I_{sb}(t) &= \hat{I}_s \cos(\omega t - \frac{2\pi}{3}) \\ I_{sc}(t) &= \hat{I}_s \cos(\omega t + \frac{2\pi}{3}) \end{aligned} \tag{17}$$

Where $\hat{I}_s$ represents the peak amplitude of the currents. These electrical quantities can be transformed to the stationary α, β frame by using Clarke's Transform expressed by the following [10]:

$$\begin{bmatrix} I_{s\alpha}(t) \\ I_{s\beta}(t) \end{bmatrix} = k \begin{bmatrix} 1 & -\frac{1}{2} & -\frac{1}{2} \\ 0 & \frac{\sqrt{3}}{2} & -\frac{\sqrt{3}}{2} \end{bmatrix} \begin{bmatrix} I_{sa}(t) \\ I_{sb}(t) \\ I_{sc}(t) \end{bmatrix} \tag{18}$$

The coefficient k in (18) can be chosen arbitrarily, however often it is selected either as $\sqrt{\frac{2}{3}}$ or $\frac{2}{3}$, these scaling factors enforce power and magnitude invariant transformations respectively. The latter results in peak amplitudes to remain consistent across all reference frames and is adopted in this dissertation. The resultant current space vector viewed from the $\alpha\beta$ frame rotates at ω_s, its relative position with respect to the α axis is θ_s.

The stator current space vector in the stationary frame can be further transformed to the synchronous d_s, q_s frame by using Park's Transform expressed by the following expression [10]:

$$\begin{bmatrix} I_{sd} \\ I_{sq} \end{bmatrix} = \begin{bmatrix} \cos(\theta_s) & \sin(\theta_s) \\ -\sin(\theta_s) & \cos(\theta_s) \end{bmatrix} \begin{bmatrix} I_\alpha(t) \\ I_\beta(t) \end{bmatrix} \tag{19}$$

The resultant current space vector viewed from the dq_s frame is stationary, therefore its synchronous components (I_{sd} , I_{sq}) become constant numerical values suitable for linear control applications. If the magnitude invariant coefficient is used in the stationary transformation, then the following expression is true:

$$\left| I_{sd} + jI_{sq} \right| = \hat{I}_s \tag{20}$$

In this particular case, the angle for the synchronous transformation is θ_s . However since rotor electrical quantities exhibit dynamics at the slip frequency ω_{slip} , therefore when applying synchronous transformation to rotor signals, θ_{slip} should be used instead. The same transformation can be applied to any other balanced three phase sinusoidal signals.

2.3.3 Dynamic model

Using the synchronous transformation, the steady state DFIG model in Figure 2-5 can be presented by the following set of differential equations in the synchronous frame [53]:

$$\begin{aligned}
\vec{V}_s^e &= R_s \vec{I}_s^e + \frac{d\vec{\phi}_s^e}{dt} + j\omega_s \vec{\phi}_s^e \\
\vec{V}_r^e &= R_r \vec{I}_r^e + \frac{d\vec{\phi}_r^e}{dt} + j\omega_{slip} \vec{\phi}_r^e \\
\vec{\phi}_s^e &= L_s \vec{I}_s^e + L_m \vec{I}_r^e \\
\vec{\phi}_r^e &= L_r \vec{I}_r^e + L_m \vec{I}_s^e
\end{aligned} \tag{21}$$

Where

$\vec{\phi}_s^e, \vec{\phi}_r^e$ = Stator and rotor flux space vectors

L_m = Magnetizing inductance

$L_s = L_{ls} + L_m$ = Stator synchronous inductance

$L_r = L_{lr} + L_m$ = Rotor synchronous inductance

Note the superscript e in (21) indicates that the associated vector is viewed from the synchronous frame, therefore they are composed of their respective dq components. The electromagnetic torque produced by the machine is expressed as [52]:

$$T_e = \frac{3}{2} P_p \frac{L_m}{L_s} \mathrm{Im}[\vec{\phi}_s^{\,e} \vec{I}_r^{\,e*}] \tag{22}$$

Note T_e in (22) is exactly the same as that in (11), however it is computed from an electrical perspective here, which in turn serves as correlation between the DFIG electrical and mechanical models.

Active and reactive power in a three-phase system can be computed by using complex equations:

$$\begin{aligned} P &= \mathrm{Re}[\vec{V}^{\,e} \vec{I}^{\,e*}] \\ Q &= \mathrm{Im}[\vec{V}^{\,e} \vec{I}^{\,e*}] \end{aligned} \tag{23}$$

Since voltage and current space vectors in the synchronous frame can be presented by complex dq components as:

$$\begin{aligned} \vec{V}^{\,e} &= V_d + jV_q \\ \vec{I}^{\,e} &= I_d + jI_q \end{aligned} \tag{24}$$

It follows that stator and rotor power can then be expressed by:

$$\begin{aligned} P_s &= \frac{3}{2}(V_{sd} I_{sd} + V_{sq} I_{sq}) \quad Q_s = \frac{3}{2}(V_{sq} I_{sd} - V_{sd} I_{sq}) \\ P_r &= \frac{3}{2}(V_{rd} I_{rd} + V_{rq} I_{rq}) \quad Q_r = \frac{3}{2}(V_{rq} I_{rd} - V_{rd} I_{rq}) \end{aligned} \tag{25}$$

The scaling coefficient $\frac{3}{2}$ stems from magnitude invariant transformation. The modulus of all the voltage and current space vector components is equal to their respective peak amplitudes, shown in (20), therefore proper scaling is needed to compute the actual three-phase power.

2.4 Grid filter model

As discussed in section 2.1.4, the L-type filter is considered for GSC PWM harmonics attenuation. Synchronous transformation can be applied to the grid filter electrical dynamics in the exact same manner as that in the DFIG case.

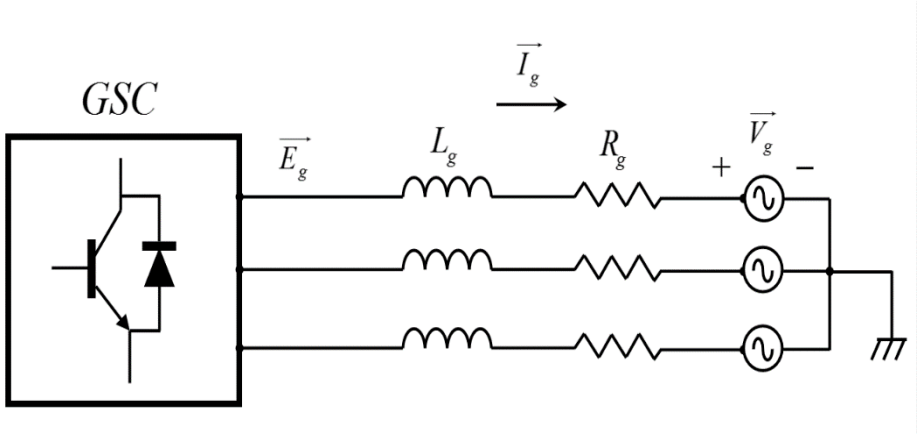

Figure 2-7: Grid filter circuit diagram

A schematic circuit diagram for the grid filter connection between GSC and the grid is shown in Figure 2-7. Note the motoring convention is used here. Applying Kirchhoff's voltage loop law, the following voltage equations in the natural reference frame of the grid can be obtained:

$$\underset{\mathrm{r}}{E}_g^n = \underset{\mathrm{r}}{I}_g^n R_g + L_g \frac{d\underset{\mathrm{l}}{I}_g^n}{dt} + \underset{\mathrm{r}}{V}_g^n \tag{26}$$

The parameters in (26) are:

$\underset{\mathrm{l}}{E}_g^n$ = GSC output voltage

$\underset{\mathrm{l}}{V}_g^n$ = Grid voltage

$\underset{\mathrm{l}}{I}_g^n$ = Grid current

L_g = Grid filter inductance

R_g = Grid filter parasitic resistance

Here the superscript *n* represents natural reference frame space vectors. Applying (18) and (19), in order, to (26), then the grid filter electrical dynamics can be expressed in the synchronous frame by [45]:

$$\underset{\mathrm{r}}{E}_g^e = \underset{\mathrm{r}}{I}_g^e R_g + L_g \frac{d\underset{\mathrm{l}}{I}_g^e}{dt} + j\omega_g L_g + \underset{\mathrm{r}}{V}_g^e \tag{27}$$

In (27) ω_g is the electrical angular frequency of grid currents and voltages. The grid active and reactive power, using the same logical derivation shown in (23)-(25), can be expressed by:

$$\begin{aligned} P_g &= \frac{3}{2}(V_{gd}I_{gd} + V_{gq}I_{gq}) \\ Q_g &= \frac{3}{2}(V_{gq}I_{gd} - V_{gd}I_{gq}) \end{aligned} \tag{28}$$

Where

$V_{gd}, I_{gd}, V_{gq}, I_{gq}$ = The dq components of synchronous grid voltage and current space vectors

2.5 DC-link model

The GSC is responsible for regulating the DC-link voltage constant with varying power flow. Therefore the dynamics of the DC-link voltage with respect to the power equilibrium between RSC and GSC must be accurately modelled. The energy storage in the DC-link capacitor is given by [41]:

$$W_{dc} = \frac{1}{2} C_{dc} V_{dc}^2 \tag{29}$$

Where

W_{dc} = Energy stored in DC-link capacitor

V_{dc} = DC-link voltage

C_{dc} = DC-link capacitance

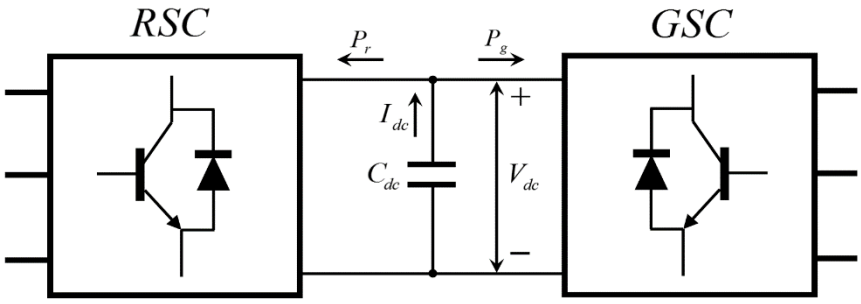

Figure 2-8: DC-link capacitor circuit

A schematic circuit diagram for the DC-link capacitor is shown in Figure 2-8, where P_g and P_r represents grid and machine power flow, respectively. Note their positive direction results from the motoring convention employed on both grid and DFIG dynamic models. If losses across the converters are considered negligible, then the power equilibrium between GSC and RSC with respect to the DC-link stored energy can be expressed by:

$$\frac{dW_{dc}}{dt} = V_{dc} C_{dc} \frac{dV_{dc}}{dt} = P_r + P_g \tag{30}$$

Since DC-link voltage must be regulated by the GSC, P_r in (30) can be considered as a disturbance. Thus, the DC-link voltage dynamics with respect to P_g defined in (28), can be expressed as:

$$V_{dc} C_{dc} \frac{dV_{dc}}{dt} = P_r + \frac{3}{2}(V_{gd} I_{gd} + V_{gq} I_{gq}) \tag{31}$$

It can be seen from (30) and (31) that V_{dc} will remain constant when a power equilibrium is reached between the GSC and RSC i.e. $P_g = -P_r$.

2.6 Dynamic operation of DFIG wind energy system

This section details the overall operation for a DFIG wind turbine with respect to its mechanics and MPPT. However it should be emphasized that turbine control is not within the scope of this dissertation. The analysis provided here is aimed at providing a comprehensive understanding for the DFIG wind energy system.

2.6.1 Power flow

The power flow within a DFIG system can be shown by correlating the aerodynamic, stator and rotor powers defined in (2) and (16). It should be noted that the motoring convention is adopted, therefore positive power flow is towards the generator. Given the assumption that the losses within the system can be neglected, then the following approximations are true:

$$\begin{aligned} P_a &\approx -P_s - P_r \\ P_s &\approx \frac{-P_a}{(1+s)} \\ P_r &\approx -s\frac{P_a}{(1+s)} \end{aligned} \tag{32}$$

A simplified DFIG power flow diagram is shown in Figure 2-9 demonstrating the relationship in (32).

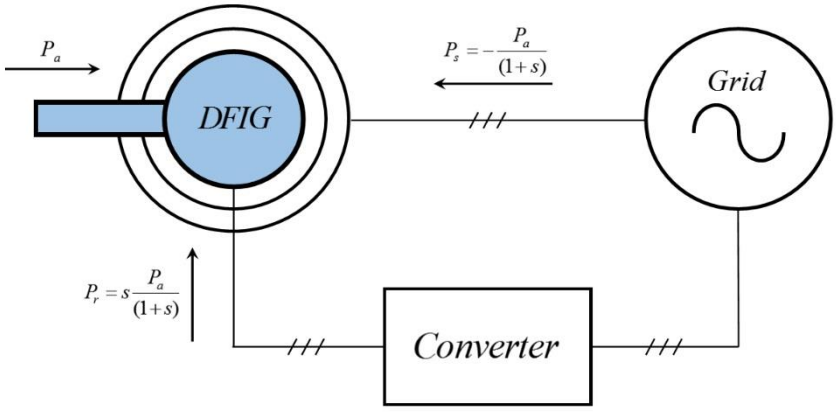

Figure 2-9: DFIG power flow

Assuming the turbine pitch angle is optimal at 0^o, then P_a described in (2) becomes a function of wind velocity V_w and shaft mechanical speed ω_m which is a control variable. Since the machine slip s is directly related to ω_m, therefore a relationship exists between the shaft speed and wind velocity where maximum aerodynamic power can be extracted.

2.6.2 MPPT operating curve description

For the turbine control level discussed in section 2.1.5, its main task is to provide reference signals for the generator control level as well as providing pitch angle control for high wind speed conditions. Figure 2-10 below shows simulated results for P_a with varying ω_m for discrete wind velocities.

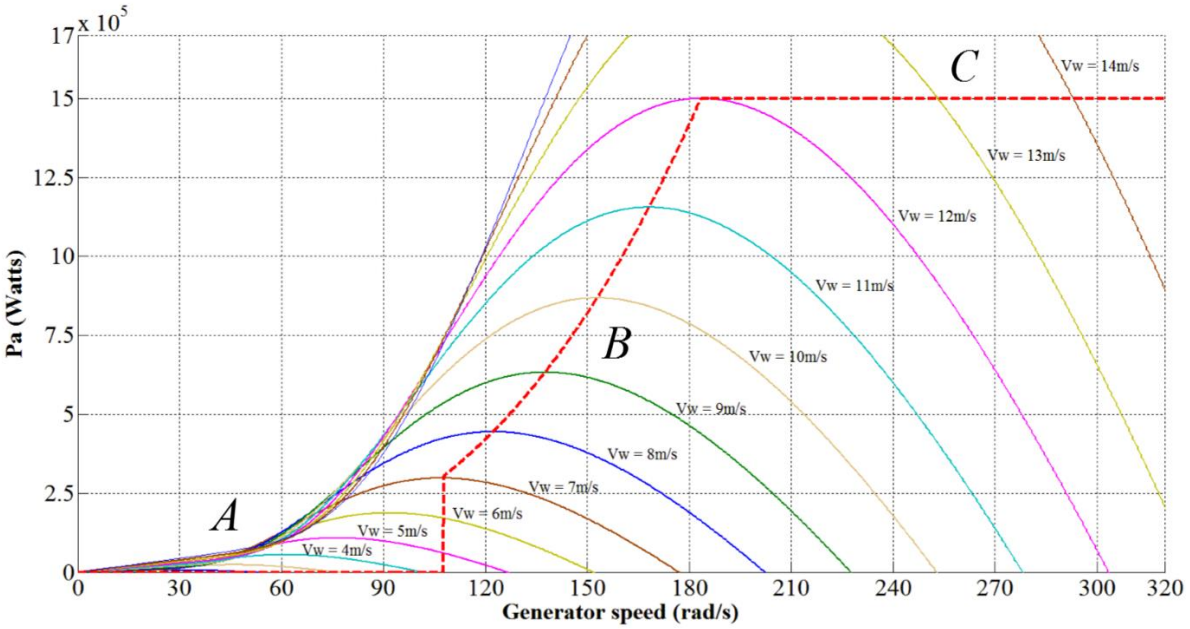

Figure 2-10: DFIG wind turbine MPPT

The simulation was based on a 1.5MW 4 pole DFIG data given in [54]. The cut-in and rated wind velocities are 7m/s and 12m/s respectively. The corresponding generator variable speed range is rated at 25% of the synchronous speed, ranging from $\omega_m = 118(rad/s)$ to $196(rad/s)$. There are three main operating regions displayed in Figure 2-10:

- A – For wind speeds below the cut-in velocity, the generator is disconnected from the grid therefore no power is generated in this region.
- B – Between cut-in and rated wind speeds of the turbine, the generator speed is controlled to follow the MPPT curve (red dotted line) so as to extract maximum power from the wind.
- C – When the wind speed exceed rated condition, turbine pitch control should be activated so as to keep generator power at rated condition. However, generator must be disconnected from the grid when the wind speed exceed limits defined by the pitch controller.

The MPPT curve in region B is actually consequential to a constant turbine tip speed ratio which is kept at an optimal level through generator speed control. The optimal tip speed ratio λ_{opt} can be found from turbine characteristic curves such as the one shown in Figure 2-3. Once λ_{opt} is known, then the speed reference for the generator control level can be provided by rearranging (5):

$$\omega_{opt}^{ref} = \frac{\lambda_{opt} V_w}{R} \tag{33}$$

In reality (33) is most often implemented as a look-up table, with predefined ω_{opt}^{ref} values for any wind speed within the operating speed range of the DFIG [54].

3. Generator Control Architecture

It is well known for variable speed drive systems, such as the DFIG, vector control architecture is an industry standard due to its robust closed loop performance [11]–[13]. **Error! Reference source not found.** below demonstrates the generic vector control implementation for a DFIG wind turbine.

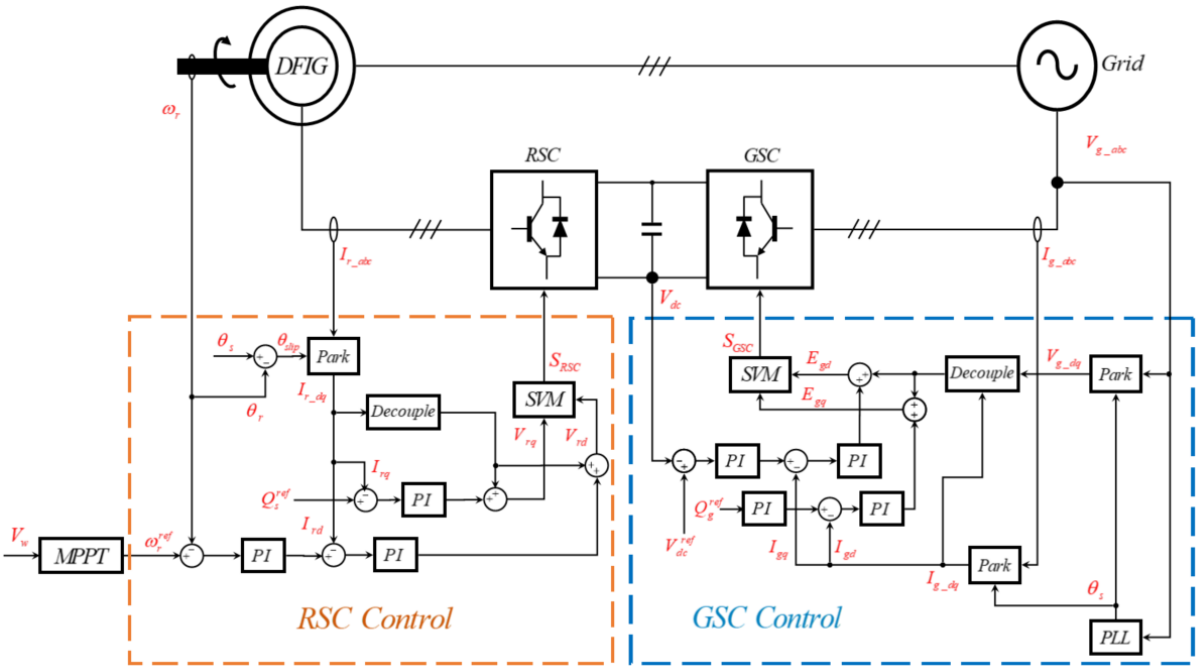

Figure 3-1: Vector controller implementation for wind-turbine-driven DFIG

The generator control level discussed in section 2.1.5 can be further broken down into two components:

- RSC control – Responsible for regulating generator speed, stator active and reactive power by providing control voltages via the RSC.
- GSC control – Responsible for regulating DC-bus voltage, grid active and reactive power by providing control voltages via the GSC.

Each component of the generator control level consists of a dual closed loop controller based on proportional-integral (PI) compensators as shown in **Error! Reference source not found.**. For the GSC, the inner and outer control loops are responsible for regulating grid currents and DC-bus voltage respectively. For the RSC, the inner and outer control loops are responsible for controlling DFIG rotor currents and machine speed respectively. In addition, the outer loops provide current references for the inner loops, thus their dynamics must be much slower than that of the inner current loops so as to enable decoupled control design [11].

The vector control concept can be implemented based on the synchronous dynamic models presented in chapter 2, where corresponding dq voltage components are individually commanded for decoupled active and reactive power regulation. Therefore, accurate acquisition of grid voltage and rotor

mechanical angles are essential for the synchronous reference frame transformation. Grid angle can be captured by a phase locked loop (PLL) [55] whereas the rotor mechanical angle can be obtained by an encoder.

This section first details the general controller design process based on pole placement and IMC tuning techniques. These concepts are then extended to controller design for the vector control of a DFIG, in particular with respect to the dynamic models developed in chapter 2. Practical implementation issues with the controller, such as integrator anti-windup, discretization and command voltage limiting are also presented in detail.

3.1 Pole placement design

For most control applications, the 'classical' feedback system [22] shown in Figure 3-2 is used. This corresponds to an individual loop structure for the dual loop controllers shown in **Error! Reference source not found.**.

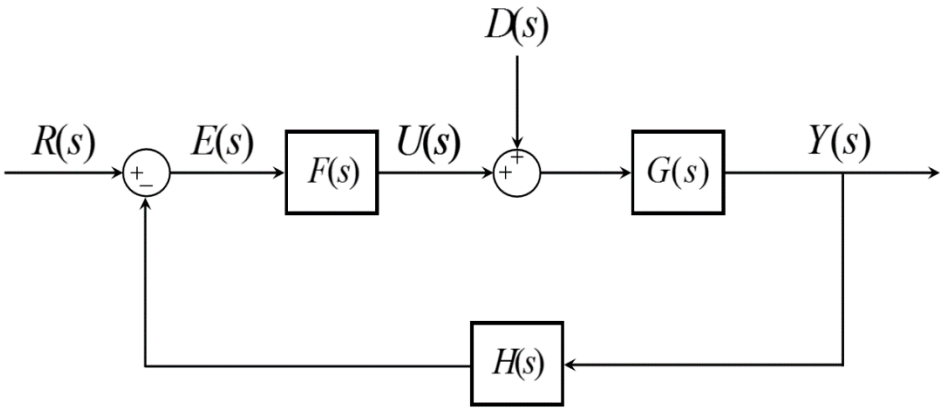

Figure 3-2: Classical feedback control structure

Note the structure shown is based on Laplace representation of time domain systems. The functions $F(s), G(s)$ and $H(s)$ are transfer functions for the controller, plant process and feedback filter respectively. Whereas $R(s), E(s), U(s), D(s)$ and $Y(s)$ are system signals representing the set-point, feedback error, plant input, system disturbance and plant output respectively.

Pole placement tuning involves the matching of closed loop system poles to that of a predefined characteristic equation [12], which contains all the desired transient response information that closely approximates a second order system given by its generic form as [22]:

$$G_{2nd}(s) = \frac{\omega_n^{\,2}}{s^2 + 2\zeta\omega_n s + \omega_n^{\,2}} \tag{34}$$

Expression (34) exhibits an un-damped natural frequency ω_n, and the damping ratio ζ. Changing these two values will result in changes to the system transient response with respect to settling time t_s, rise

time t_r, peak time t_p and percent overshoot $\%OS$ of the system step response respectively. These variables are control design specifications which have the following relationship with ω_n and ζ :

$$t_s = -\frac{\ln(0.02\sqrt{1-\zeta^2})}{\zeta\omega_n}$$
$$t_p = \frac{\pi}{\omega_n\sqrt{1-\zeta^2}} \tag{35}$$
$$\%OS = e^{\left(\frac{-\zeta\pi}{\sqrt{1-\zeta^2}}\right)} \times 100$$

Rise time t_r do not have explicit analytical relationship with respect to ω_n and ζ , generally it increases with increasing ζ and is defined for a percentage band around the steady state settling point. When designing using the pole placement method, each of these design specifications should be considered carefully. In most cases the design focus is centred on a single specification with compromises made for the less imperative requirements. For the purpose of demonstration, consider the following generic form of a first order system transfer function:

$$G_{1st}(s) = \frac{1}{As + B} \tag{36}$$

Reflecting on Figure 3-2, assuming unity feedback (i.e. $H(s) = 1$ and $D(s) = 0$) and the plant resembles a first order system described in (36) (i.e. $G(s) = G_{1st}(s)$), thus the controller $F(s)$ can be implemented as a PI compensator [22] expressed by:

$$PI(s) = k_P + \frac{k_I}{s} \tag{37}$$

Parameters k_p and k_I in (37) are the proportional and integral gain for the PI compensator. Substituting (36) and (37) into the closed loop structure in Figure 3-2, then the open loop system transfer function can be found as:

$$G_{open}(s) = G_{1st}(s)PI(s) = \frac{k_P s + k_I}{As^2 + Bs} \tag{38}$$

The closed loop system transfer function can then be formulated from (38):

$$G_{cl}(s) = \frac{Y(s)}{R(s)} = \frac{G_{open}(s)}{1 + G_{open}(s)} = \frac{\frac{k_P}{A}s + \frac{k_I}{A}}{s^2 + \frac{(B + k_P)}{A}s + \frac{k_I}{A}} \tag{39}$$

Compare (39) to (34), it can be seen that the form for both expressions are of the second order type (i.e. denominator has two poles). The numerator for $G_{cl}(s)$ in (39) indicates there is a closed loop real zero at $s = -\frac{k_I}{k_P}$ determined by $PI(s)$, which means that $G_{cl}(s)$ do not represent $G_{2nd}(s)$ exactly. However, the dynamics caused by any closed loop zeroes can be regarded as negligible given that these zeroes are sufficiently far from the dominant pole pair of a second order system [22]. With this assumption, the following approximation can be made:

$$G_{cl}(s) \approx \frac{\frac{k_I}{A}}{s^2 + \frac{(B+k_P)}{A}s + \frac{k_I}{A}}$$

$$G_{cl}(s) \approx G_{2nd}(s) \tag{40}$$

$$\therefore \frac{\frac{k_I}{A}}{s^2 + \frac{(B+k_P)}{A}s + \frac{k_I}{A}} \approx \frac{{\omega_n}^2}{s^2 + 2\zeta\omega_n s + {\omega_n}^2}$$

If we equate all coefficients in (40) then a clear relationship exists between A, B and ω_n, ζ, which can be expressed by:

$$\begin{aligned} k_I &= \omega_n^2 A \\ k_P &= 2\zeta\omega_n A - B \end{aligned} \tag{41}$$

Equation (41) presents a quantitative method for computing PI compensator gains, provided that the plant model is a first order system with parameters A, B. The values of ζ, ω_n are also required, these can be selected based on their relationship with desired system response properties defined in (35). Since the assumption for a non-dominant zero must hold for an accurate approximation between $G_{cl}(s)$ and $G_{2nd}(s)$, therefore pole placement tuning requires simulation after computing the PI gains, to ensure that the closed loop response is indeed as desired. Typical tools such as the Root Locus and Nyquist chart can be used for validating the final design.

3.2 Internal Model Control design

Internal Model Control (IMC) was originally developed for chemical engineering processes [56]. However, it is shown in [20], [21], [57] that this control methodology can be extended to applications involving variable speed ac machines.

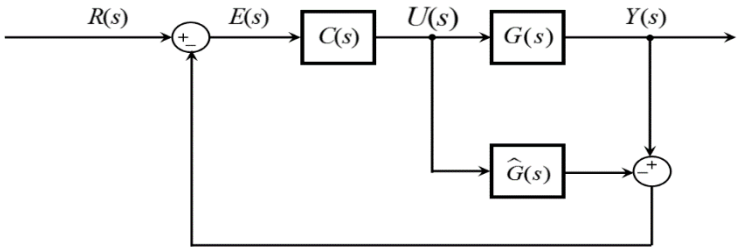

Figure 3-3: IMC structure

Figure 3-3 depicts the IMC structure, where a process model $\hat{G}(s)$ is used internally in parallel with the actual process plant $G(s)$. The closed loop is augmented by the controller $C(s)$. Given that $\hat{G}(s)$ is an exact representation of $G(s)$, then the closed loop transfer function will match the open loop dynamics such that:

$$G_{cl}(s) = G_{open}(s) = C(s)G(s) \tag{42}$$

Note all Laplace functions such as $Y(s), E(s), G_{cl}(s), G(s)$, are generic representations of different system signals, therefore no conflict of variables should be mistaken between different control structures using the same function. For example $G_{cl}(s)$ represents the closed loop transfer function for the classical feedback system, but it is also used to represent the closed loop transfer function for the IMC structure.

It can be recognised from (42) that if we make $C(s) = G^{-1}(s)$, then direct transfer occurs between set-point $R(s)$ and output $Y(s)$. However, this is generally unachievable, due to the fact that both $C(s)$ and $G(s)$ have to be individually stable. Since $C(s)$ is unstable if $G(s)$ contain right-half plane zeroes or has higher denominator order, therefore the controller is rarely suitable.

These issues can be solved by separating $G(s)$ into two components as well as detuning the optimal controller with a low pass filter, this process is detailed in the following expression [56]:

$$\begin{gathered} G(s) = G_A(s)G_M(s) \\ C(s) = G^{-1}(s)L(s) \qquad where \;\; L(s) = \frac{\alpha^n}{(s+\alpha)^n} \end{gathered} \tag{43}$$

$G_A(s)$ and $G_M(s)$ in (43) are components of $G(s)$ where all the right-half plane zeroes are contained in $G_A(s)$. The order of the low-pass filter $L(s)$, denoted by n, should be chosen sufficiently large so as to facilitate a 'proper' $C(s)$ i.e. denominator order must be higher than that of the numerator.

Figure 3-3 describes a completely different control structure when compared to the classical case in Figure 3-2. However, IMC can be related to conventional feedback systems by rearranging its block diagram such that the structure shown in Figure 3-4 results.

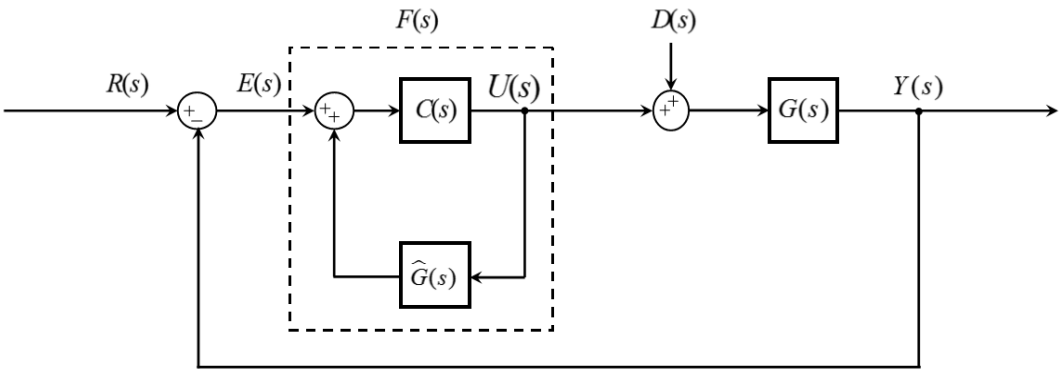

Figure 3-4: 'Classical' IMC structure

The relationship between the classical controller $F(s)$ with respect to the internal model $\hat{G}(s)$ and the IMC controller $C(s)$ can be described by:

$$F(s) = \frac{C(s)}{1 - \hat{G}(s)C(s)} \tag{44}$$

The same process as presented in section 3.1 is carried out here to demonstrate the control design steps based on IMC. The generic first order system from (36) is again considered, and it is obvious that $G_{1st}(s)$ do not have any right-half plane zeroes. Therefore, the internal model controller $C(s)$ can be presented by the exact inverse of the plant model and it is sufficient to choose a first order low pass filter for $L(s)$ (i.e. $n = 1$). From (43) and (44), the 'classical' IMC controller structure, suitable for $G_{1st}(s)$, can be derived as:

$$\begin{aligned} C(s) &= G^{-1}(s)\frac{\alpha}{s+\alpha} \\ \therefore F(s) &= G^{-1}(s)\frac{\alpha}{s} = A\alpha + \frac{B\alpha}{s} \end{aligned} \tag{45}$$

Compare (45) to $PI(s)$ in (37), it is clear that we can simply equate coefficients to find k_P and k_I given by:

$$A\alpha + \frac{B\alpha}{s} = k_P + \frac{k_I}{s}$$
$$\therefore k_P = A\alpha \qquad k_I = B\alpha \tag{46}$$

The open loop transfer function resulting from $F(s)$ in (46) can be found as, assuming $D(s) = 0$:

$$G_{open}(s) = F(s)G(s) = \frac{\alpha}{s} \tag{47}$$

Whereas the closed loop transfer function can then be formulated from (47):

$$G_{cl}(s) = \frac{Y(s)}{R(s)} = \frac{G_{open}(s)}{1 + G_{open}(s)} = \frac{\alpha(As + B)}{(s + \alpha)(As + B)}$$
$$\therefore G_{cl}(s) = \frac{\alpha}{s + \alpha} \tag{48}$$

It can be observed from (48) that the placement of the closed loop zero, based on IMC, will always cancel out the slower system pole at $s = -\frac{B}{A}$. Thus, the resulting closed loop response exhibits first order dynamics, and α is a direct representation of the closed loop system bandwidth. For a first order system, α can be related to the 2% settling time t_s and 10%-90% rise time t_r by the following expressions [22]:

$$t_s = \frac{4}{\alpha} \qquad t_r = \frac{\ln(9)}{\alpha} \tag{49}$$

It should be noted that the procedure of finding the second order closed loop transfer function, required for pole placement tuning, is not needed in the IMC case. It is derived here to provide insight for the IMC principle. The controller design based on IMC is solely dependent on the desired closed loop bandwidth, which is related to system response specifications defined in (49). Compared to the pole placement tuning method it is easy to see that IMC tuning simplifies the control design for a first order system.

3.2.1 Active damping

From Figure 3-4 the closed loop disturbance rejection can be investigated by taking the transfer function from the load disturbance $D(s)$ to output signal $Y(s)$ given as:

$$\frac{Y(s)}{D(s)} = G_{DY}(s) = \frac{G(s)}{1 + G(s)F(s)} \tag{50}$$

Substituting $G_{1st}(s)$ from (36) and $F(s)$ from (45) into (50), the disturbance to output transfer function can be expressed as:

$$G_{DY}(s) = \frac{s}{(s+\alpha)(As+B)} \tag{51}$$

Since $-\frac{A}{B}$ (i.e. plant time constant) is generally much bigger than $-\frac{1}{\alpha}$ (i.e. closed loop time constant) [22], therefore (51) shows that the disturbance rejection of the closed loop system being largely dictated by the slower plant process.

A method for speeding up the closed loop disturbance rejection is presented in [11], [23] known as active damping. An inner feedback loop with constant gain R_a is introduced altering the controller structure in Figure 3-4 slightly. The resulting structure is shown in Figure 3-5.

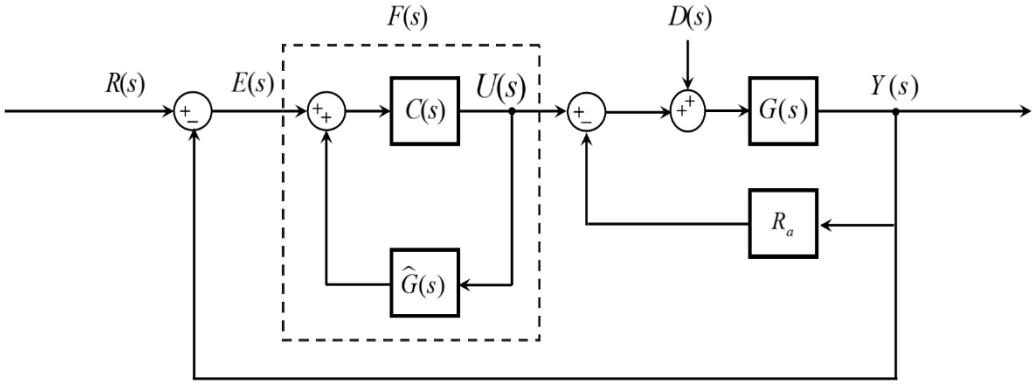

Figure 3-5: Implementation of active damping with 'classical' IMC controller

Note R_a can be dynamic or constant. A constant feedback gain on the inner loop is considered here, which acts as a pure damping coefficient on the disturbance. The transfer function in (51) is thus changed to:

$$G_{DY}(s) = \frac{s}{(s+\alpha)(As+B+R_a)} \tag{52}$$

If R_a is chosen so that $R_a = \alpha A - B$, then (52) can be expressed as:

$$G_{DY}(s) = \frac{s}{A(s+\alpha)^2} \tag{53}$$

The transfer function in (53) shows that for the above chosen value of R_a, the output response due to load disturbance will be damped with the closed loop time constant. It is important to ensure that $R_a > 0$, since if not, the system might become unstable. Therefore the closed loop bandwidth is limited by the implementation of active damping where its minimum value must be:

$$\alpha_{\min} > \frac{B}{A} \tag{54}$$

The computation for PI gains with active damping slightly deviates from that shown in (46). In particular the additional damping term R_a must be considered, which results in the following expressions for k_P and k_I:

$$\begin{aligned} k_P &= \alpha A \\ k_I &= \alpha(B + R_a) \end{aligned} \tag{55}$$

3.3 Controller saturation and Integrator anti-windup

In the practical implementation of any control systems, control signals must have saturation bounds due to physical limitations of hardware. For example in the DFIG system, current and machine speed controller outputs must be limited within acceptable levels to prevent adverse machine operating conditions.

During controller saturation the integral component of a PI compensator will accumulate the increasing error between feedback and reference set-point. This phenomenon is known as integrator-windup [58]. The resulting effect usually manifests itself in overshoots when the controller returns to normal conditions after a saturated step response.

A simple technique, back-calculation [41], provides a robust counter measure for the problem of integrator-windup. Consider the 'classical' feedback control system presented in Figure 3-2, where $F(s) = PI(s)$. If the controller output $U(s)$ has become saturated to $\bar{U}(s)$ due to a large change in $R(s)$, therefore a large $E(s)$ will result where:

$$\begin{aligned} U(s) &= k_P E(s) + k_I I(s) \\ I(s) &= \frac{E(s)}{s} \\ \bar{U}(s) &= U(s)\Big|_{\min}^{\max} \end{aligned} \tag{56}$$

In order for $U(s)$ in (56) to not accumulate all the error during saturation due to the integral component $k_I I(s)$, the error $E(s)$ should be modified to $E^*(s)$ so as to ensure that $U(s) = \bar{U}(s)$:

$$\bar{U}(s) = k_P E^*(s) + k_I I(s) \tag{57}$$

Subtracting $U(s)$ in (56) from $\bar{U}(s)$ in (57), then back calculating [41] for the modified error $E^*(s)$ will result in:

$$E^*(s) = \frac{1}{k_P}[\bar{U}(s) - U(s) + k_P E(s)] = E(s) + \frac{1}{k_P}[\bar{U}(s) - U(s)] \tag{58}$$

The actual control signal $U(s)$ with back-calculation implemented will result in the form as:

$$U(s) = k_P E(s) + \frac{k_I}{s} E^*(s) \tag{59}$$

Note the proportional component $k_P E(s)$ in (59) uses the original error signal since it is just a linear gain, which does not result in wind-up issues like the integral component.

3.4 Discretization

Most modern control systems are implemented with digital electronics that converts analogue signals to discrete data, sampled at constant time intervals T_{samp}. Such conversion introduces signal delays into the system that is dependent on the sampling frequency $f_{samp} = \frac{1}{T_{samp}}$ [22]. For large T_{samp}, the consequent delay cannot be ignored and full discretization of the system model must be performed. Techniques such as the Tustin's trapezoidal method can be used for discrete system stability analysis [58].

The controller design in this dissertation is implemented on a field programmable gate array (FPGA). It is a digital electronic component, capable of achieving highly deterministic processing speed, limited by its on-board clock at 40MHz. Since the control sampling rate can be easily set to at least ten times faster than the closed loop bandwidth of the system, therefore only continuous time domain control analysis is considered in this dissertation. However, the integral component of the PI compensator must be implemented digitally which can be achieved by using shift registers. The general expression for a digital integrator can be expressed by:

$$k_I I(k) = k_I [E^*(k) + E^*(k-1)] \tag{60}$$

$I(k)$ in (60) represents the current sample of the integral component whereas $E^*(k)$ and $E^*(k-1)$ represents the current and previous sample of the modified error.

3.5 Command voltage limiting

The vector controller illustrated in **Error! Reference source not found.** consists of two feedback loops. The controller output for each loop must be limited following the discussion in section 3.3. The outer loops provide current control references for the inner loop on only one of the dq axis components, thus it can be limited easily by saturating its numerical value. The inner loop provides voltage control references, which in turn must be converted into PWM signals for the converter. These control voltages cannot be limited by simple numerical saturation as in the case of outer loop control. This is due to the

fact that the converter output voltage depends on both dq components of the control voltage. Therefore the inner loop output control voltage must be saturated by limiting the modulus of its dq components.

3.5.1 Voltage saturation condition

The condition for saturating the control voltage can be expressed by:

$$\left|\vec{V}_{com}\right| \geq \frac{V_{dc}}{\sqrt{3}}$$
$$\left|\vec{V}_{com}\right| = \sqrt{(V_{com}^{d})^2 + (V_{com}^{q})^2} \tag{61}$$

$\vec{V}_{com}$ in (61) represents the output control voltage vector from the inner loop controllers, where V_{com}^{d} and V_{com}^{q} are its dq axis components. The expression $\frac{V_{dc}}{\sqrt{3}}$ derives from maximum achievable voltage within the linear modulation range for space vector pulse-width modulated (SVPWM) converters [59]. Converter modulation algorithms are presented in great detail in Chapter 4. In this dissertation, over modulation scenarios of the converter are not considered.

3.5.2 Voltage saturation implementation

Given that the condition in (61) is met, the actual saturation voltage command $\left|\vec{V}_{com}\right|_{\max}$ can be given as:

$$\left|\vec{V}_{com}\right|_{\max} = \frac{V_{dc}}{\sqrt{3}} \times \frac{\left|\vec{V}_{com}\right|}{\left|\vec{V}_{com}\right|} = \frac{V_{dc}}{\sqrt{3}} \times \frac{\sqrt{(V_{com}^{d})^2 + (V_{com}^{q})^2}}{\sqrt{(V_{com}^{d})^2 + (V_{com}^{q})^2}} \tag{62}$$

Equation (62) basically states that voltage saturation will happen at the limit of converter linear modulation range, since $\frac{\left|\vec{V}_{com}\right|}{\left|\vec{V}_{com}\right|} = 1$ enforces a unity modulation index, thus no over modulation can occur.

3.6 Phase-locked loop

The phase-locked loop (PLL) is used to extract grid voltage angle information, which is essential for synchronizing the GSC output current with the grid voltage [55]. The most common PLL implementation is the synchronous PI PLL [55], [60], shown in Figure 3-6.

The feedback for this particular PLL structure is the grid q - axis voltage V_{gq}, since its magnitude dictates

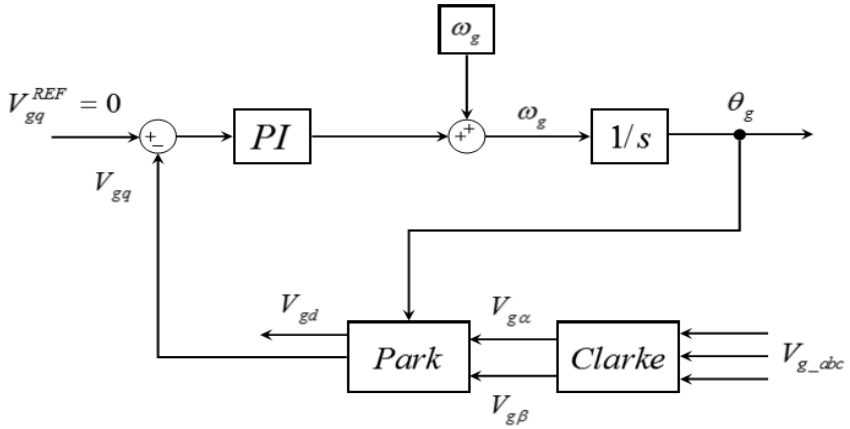

Figure 3-6: Synchronous PI PLL

the converter output current phase angle [60]. The reference V_{gq}^{REF} merely provides a reference point for locking onto the grid voltage at a particular phase angle. The PI compensator reduces any phase angle mismatch, between the grid voltage and converter currents, down to zero. With the reference grid angular frequency ω_g acting as a feedforward term, the PI output is then the grid frequency. The pure integrator $\frac{1}{s}$ serves as a voltage controlled oscillator (VCO), which converts ω_g into the grid voltage angle θ_g needed in the synchronous transformation.

The closed loop transfer function for the PLL in Figure 3-6 can be written as:

$$G_{cl}(s) = \frac{k_p s + k_I}{s^2 + k_P s + k_I} \tag{63}$$

Using the pole placement tuning method given in section 3.1.then the PI gains for the PLL can be computed as:

$$\begin{aligned} k_p &= 2\zeta\omega_n \\ k_I &= \omega_n^2 \end{aligned} \tag{64}$$

The values for ζ and ω_n in (64) can be selected by using (35).

3.7 DFIG dynamic model simplification

The DFIG dynamic model expressed in (21) is in synchronous vector form, which must be decomposed into its dq components in order to facilitate the vector controller shown in **Error! Reference source not found.**. This can be achieved by aligning the synchronous d - axis with any stator electrical space vector [61].

For the DFIG two field alignments are commonly used, namely grid voltage and stator flux orientations. These orientations produce useful simplifications for the DFIG dynamic model, which are demonstrated in this section.

3.7.1 Grid voltage orientation

Expanding on the various reference frames displayed in Figure 2-6, grid voltage oriented alignment for the DFIG synchronous frame is illustrated in Figure 3-7.

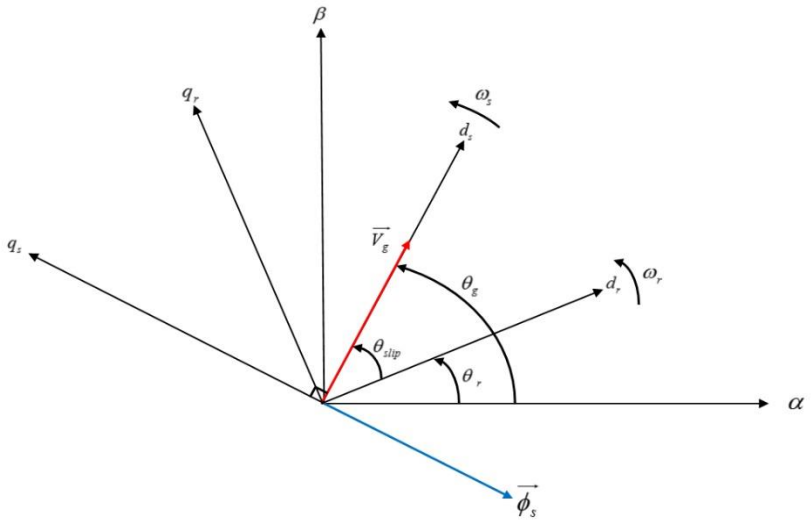

Figure 3-7: Vector diagram for DFIG grid voltage orientation

From the phasor diagram it can be seen that $\vec{d}_s$ is aligned with the grid voltage space vector $\vec{V}_g$, both rotating at an angular frequency ω_s. This is true since during normal operation, stator excitation of the machine is provided by the grid voltage. The synchronous transformation angle used for grid voltage orientation is the grid voltage angle θ_g, which can be obtained from the PLL presented in section 3.6. To transform rotor electrical quantities to the synchronous frame $\theta_{slip} = \theta_g - \theta_r$ must be used. The stator flux has a quadrature relationship with the stator voltage, therefore stator flux $\vec{\phi}_s$ is aligned with $\vec{q}_s$. Reflecting on these observations, the following conditions for the dq components of $\vec{V}_s$ and $\vec{\phi}_s$ can be deduced:

$$\vec{V}_s = \vec{V}_g$$

$$V_{sd} = \left|\vec{V}_g\right| \qquad V_{sq} = 0 \qquad (65)$$

$$\phi_{sd} = 0 \qquad \phi_{sq} = -\left|\vec{\phi}_s\right|$$

$\left|\vec{V}_g\right|$ and $\left|\vec{\phi}_s\right|$ represents amplitude of the grid voltage and stator flux respectively. Substituting (65) into (21), expressing system dynamics with respect to rotor currents, the synchronous dq dynamic equations for the DFIG can be derived as:

$$I_{sd} = \frac{-L_m I_{rd}}{L_s} \qquad I_{sq} = \frac{-\left|\vec{\phi}_s\right| - L_m I_{rq}}{L_s}$$

$$\therefore \phi_{rd} = L_\sigma I_{rd} \qquad \therefore \phi_{rq} = L_\sigma I_{rq} - \frac{L_m}{L_s}\left|\vec{\phi}_s\right|$$

$$\therefore V_{rd} = R_r I_{rd} + L_\sigma \frac{dI_{rd}}{dt} - \omega_{slip} L_\sigma I_{rq} + \omega_{slip} \frac{L_m}{L_s}\left|\vec{\phi}_s\right| \qquad (66)$$

$$\therefore V_{rq} = R_r I_{rq} + L_\sigma \frac{dI_{rq}}{dt} + \frac{L_m}{L_s}\frac{d\left|\vec{\phi}_s\right|}{dt} + \omega_{slip} L_\sigma I_{rd}$$

$$V_{sd} = R_s I_{sd} + \omega_s \left|\vec{\phi}_s\right| \qquad V_{sq} = 0$$

$$L_\sigma = L_r - \frac{L_m^2}{L_s}$$

If we assume stator resistance is negligible as it is generally small when compared to the reactance within the machine [11], [41] and the stator has an undisturbed excitation by $\left|\vec{V}_g\right|$ (i.e. balanced grid), then $\left|\vec{\phi}_s\right|$ and hence ϕ_{sq} will be constant. The voltage dynamics in (66) can then be reduced to:

$$V_{rd} = R_r I_{rd} + L_\sigma \frac{dI_{rd}}{dt} - \omega_{slip} L_\sigma I_{rq} + \omega_{slip} \frac{L_m}{L_s}\left|\vec{\phi}_s\right|$$

$$V_{rq} = R_r I_{rq} + L_\sigma \frac{dI_{rq}}{dt} + \omega_{slip} L_\sigma I_{rd} \qquad (67)$$

$$V_{sd} = \omega_s \left|\vec{\phi}_s\right| \qquad V_{sq} = 0$$

Note that in (67) rotor dq voltage equations are cross coupled, and $\frac{L_m}{L_s}\left|\overset{\mathrm{r}}{\phi}_s\right|$ in the equation for V_{rd} represents the back-EMF produced by the stator. These are considered as inherent machine characteristics and can cause instability for the final controller design. A common method is to feedforward compensate for these disturbances [41], [61], in which the cross coupling and back-EMF component in the rotor dq equations are cancelled out by modifying the controller output voltages. The feedforward compensation terms for both rotor dq axis voltages are given as:

$$\begin{aligned} d-axis: &\qquad -\omega_{slip} L_\sigma I_{rq} + \omega_{slip}\frac{L_m}{L_s}\left|\overset{\mathrm{r}}{\phi}_s\right| \\ q-axis: &\qquad +\omega_{slip} L_\sigma I_{rd} \end{aligned} \tag{68}$$

Assuming all coupling effects for V_{rd} and V_{rq} in (67) are accurately decoupled by applying (68), then the final rotor voltage dynamic equations, suitable for controller design, are given as:

$$\begin{aligned} V_{rd} &= R_r I_{rd} + L_\sigma \frac{dI_{rd}}{dt} \\ V_{rq} &= R_r I_{rq} + L_\sigma \frac{dI_{rq}}{dt} \end{aligned} \tag{69}$$

Since the parameter variables R_r, L_σ in (69) are identical for V_{rd}, V_{rq}, therefore the dq axis rotor current controller can be designed as the same. Considering rotor current as the output and voltage as input, applying Laplace transform to (69) then the rotor electrical plant model is obtained as:

$$G(s) = \frac{I_{rdq}(s)}{V_{rdq}(s)} = \frac{1}{L_\sigma s + R_r} \tag{70}$$

Substituting (65) into (22), the DFIG developed torque can be expressed with respect to the rotor d-axis current as:

$$T_e = -\frac{3}{2} P_p \frac{L_m}{L_s}\left|\overset{\mathrm{r}}{\phi}_s\right| I_{rd} \tag{71}$$

Substituting (65) and (66) into (25), the stator active and reactive power can be expressed with respect to the rotor dq-axis currents as:

$$P_s = -\frac{3}{2}\left|\underset{\rightarrow}{V_g}\right|\frac{L_m}{L_s}I_{rd}$$

$$Q_s = \frac{3}{2L_s}\left(\frac{\left|\underset{\rightarrow}{V_g}\right|^2}{\omega_s} + \left|\underset{\rightarrow}{V_g}\right|L_m I_{rq}\right) \tag{72}$$

Equations (71)-(72) shows that T_e is solely dependent on I_{rd}, and decoupled stator active and reactive power control can be achieved by regulating I_{rd} and I_{rq} respectively.

3.7.2 Stator flux orientation

Stator flux orientation for the DFIG synchronous frame is illustrated in Figure 3-8.

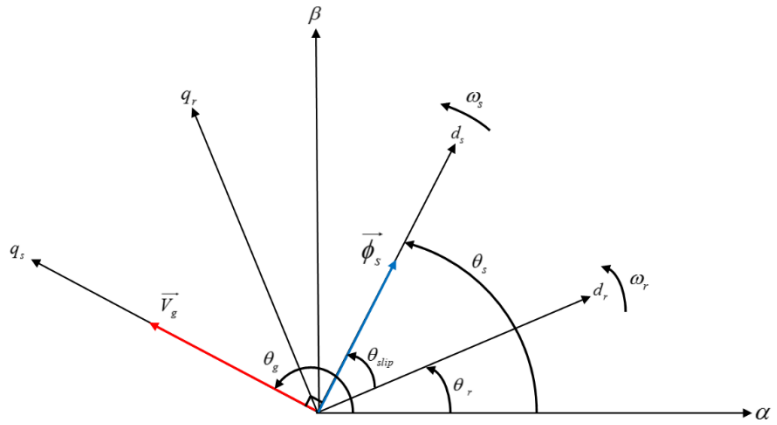

Figure 3-8: Vector diagram for DFIG stator flux orientation

From the vector diagram it can be seen that $\underset{\rightarrow}{d}_s$ is aligned with the stator flux space vector $\underset{\rightarrow}{\phi}_s$, both rotating at an angular frequency ω_s. Note the only difference between grid voltage and stator flux orientation is the $\frac{\pi}{2}$ electrical radians shift in alignment. Therefore the synchronous transformation angle for stator flux orientation is the stator flux angle $\theta_s = \theta_g - \frac{\pi}{2}$. To transform rotor electrical quantities to the synchronous frame $\theta_{slip} = \theta_g - \theta_r - \frac{\pi}{2}$ must be used. From Figure 3-8 the following conditions for the dq components of $\underset{\rightarrow}{V}_s$ and $\underset{\rightarrow}{\phi}_s$ can be deduced:

$$\underset{\rightarrow}{V}_s = \underset{\rightarrow}{V}_g$$

$$V_{sd} = 0 \quad V_{sq} = \left|\underset{\rightarrow}{V_g}\right| \tag{73}$$

$$\phi_{sd} = \left|\underset{\rightarrow}{\phi_s}\right| \qquad \phi_{sq} = 0$$

Assumptions made for the grid voltage orientation, with respect to $\vec{V}_s$ and $\vec{\phi}_s$, can be equally applied in this case. Using (73) as the starting point, the same simplification process detailed in subsection 3.7.1 can be followed. This results in the following DFIG rotor voltage dq equations:

$$\begin{aligned} V_{rd} &= R_r I_{rd} + L_\sigma \frac{dI_{rd}}{dt} - \omega_{slip} L_\sigma I_{rq} \\ V_{rq} &= R_r I_{rq} + L_\sigma \frac{dI_{rq}}{dt} + \omega_{slip} L_\sigma I_{rd} + \omega_{slip} \frac{L_m}{L_s} \left| \vec{\phi}_s \right| \end{aligned} \tag{74}$$

The machine developed torque T_e under stator flux orientation can be derived as:

$$T_e = -\frac{3}{2} P_p \frac{L_m}{L_s} \left| \vec{\phi}_s \right| I_{rq} \tag{75}$$

And the stator active and reactive power are expressed in this case as:

$$\begin{aligned} P_s &= -\frac{3}{2} \left| \vec{V}_g \right| \frac{L_m}{L_s} I_{rq} \\ Q_s &= \frac{3}{2L_s} \left(\frac{\left| \vec{V}_g \right|^2}{\omega_s} + \left| \vec{V}_g \right| L_m I_{rd} \right) \end{aligned} \tag{76}$$

Comparing stator flux orientation to grid voltage orientation, the difference is small except for the fact that the control of T_e, P_s, Q_s require regulation on different rotor dq - axis currents. It is also important to note that the synchronous transformation angle is different between the two orientations.

3.8 RSC control

Based on the prior discussions in this chapter, all the necessary tools have been developed to facilitate a proper DFIG controller design. The grid voltage orientation is adopted since it can be easily applied to both RSC and GSC control. Besides, this orientation can be considered a natural application for DFIG soft synchronization to the grid, which is discussed in great detail in chapter 5. The RSC control can be separated into rotor current and speed control, which are cascaded together such that speed control is the outer loop that provides current references for the inner current control loop. All the controllers are designed using the IMC principle for its ease of implementation. In addition, active damping is applied to all controllers for improved disturbance rejection. This section provides analytical controller structures, however, its practical implementation follows the discussions presented in section 3.3 - section 3.5.

3.8.1 Rotor current control

The feedback structure from Figure 3-5 is adapted for the dq rotor electrical plant model derived in (70). The resulting analytical structure for the rotor current controller, including active damping, is presented in Figure 3-9.

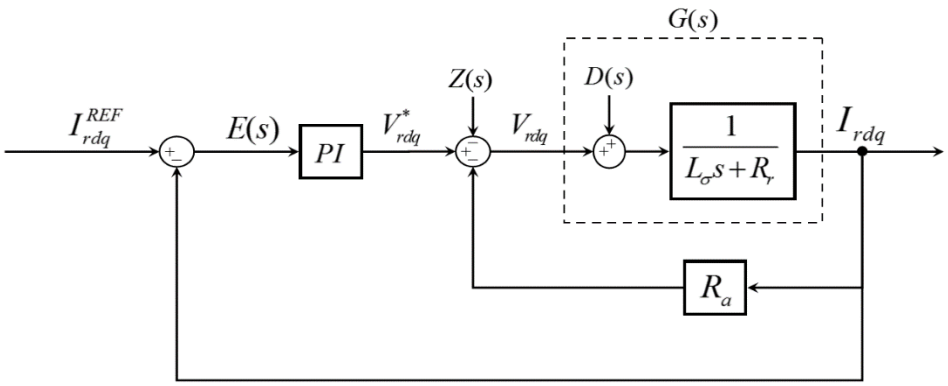

Figure 3-9: Analytical rotor current controller

Machine disturbances are represented by $D(s)$ and the corresponding feedforward compensation, given in (68), is represented by $Z(s)$. Here, I_{rdq}^{REF} is the rotor dq current references which can be obtained from the outer control loop. The PI compensator output V_{rdq}^{*} is first altered by the application of feedforward compensation and active damping, which then results in the actual control voltage V_{rdq}. Assuming perfect decoupling (i.e. $Z(s) = D(s)$) then the gains k_P, k_I for the PI compensator, as well as the value for R_a can be computed as:

$$\begin{aligned} k_P &= \alpha_r L_\sigma \\ k_I &= \alpha_r (R_r + R_a) \\ R_a &= \alpha_r L_\sigma - R_r \end{aligned} \tag{77}$$

The gain expressions in (77) are directly derived from (55) since the rotor electrical plant model $\frac{1}{L_\sigma s + R_r}$ exhibit identical form as the generic first order system $\frac{1}{As + B}$. Therefore the exact design procedure detailed in section 3.2 can be used here. Note α_r in (77) is the closed loop bandwidth for the rotor current controller, which is limited by:

$$\alpha_{r\min} > \frac{R_r}{L_\sigma} \tag{78}$$

The actual selection for α_r can be considered using its relation with system settling time t_s given by:

$$t_s = \frac{4}{\alpha_r} \tag{79}$$

3.8.2 Speed control

The DFIG speed controller can be designed using (11), the plant model can thus be derived as:

$$G(s) = \frac{\omega_m}{T_e} = \frac{1}{Js} \tag{80}$$

The transfer function in (80) has only one pole at the origin, therefore active damping is highly necessary here, since no integral action would result from standard IMC design. This means that the steady state error for the closed loop response cannot be fully eliminated. The analytical speed controller structure, with active damping, is shown in Figure 3-10.

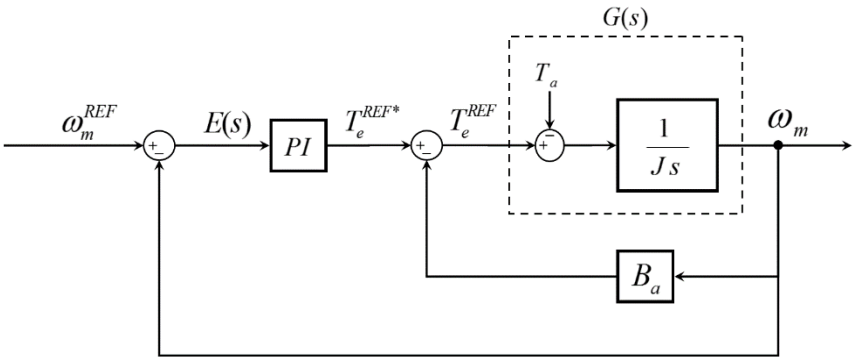

Figure 3-10: Analytical DFIG speed controller

The inner current control loop dynamic is neglected, this can be done as long as the outer loop bandwidth is at least ten time slower than that of the inner loop [10]. In this case B_a is the active damping term for the speed loop, and T_e^{REF} is the torque reference which can be converted to I_{rd}^{REF} for the inner loop as shown below:

$$I_{rd}^{REF} = -\frac{2}{3}\frac{L_s}{L_m}\frac{T_e^{REF}}{P_p\left|\phi_s^{\mathrm{r}}\right|} \tag{81}$$

The k_P, k_I gains for the PI compensator as well as the value for B_a can be computed as:

$$\begin{aligned} k_P &= \alpha_\omega J \\ k_I &= \alpha_\omega B_a \\ B_a &= k_P \end{aligned} \tag{82}$$

The closed loop bandwidth for the speed control loop α_ω, must be chosen so as to ensure much slower outer loop dynamics than the inner current loop, therefore:

$$\alpha_{\omega} \leq \frac{\alpha_r}{10} \tag{83}$$

3.9 GSC control

The GSC controller design process is similar to that of the RSC controller. The cascaded structure consists of DC-link voltage control as the outer loop, and grid current control as the inner loop. By adopting the same grid voltage orientation as the DFIG, the synchronous dynamic model of the grid filter in (27) can be decomposed into its dq components as:

$$\begin{aligned} E_{gd} &= I_{gd}R_g + L_g\frac{dI_{gd}}{dt} + V_{gd} - \omega_s L_g I_{gq} \\ E_{gq} &= I_{gq}R_g + L_g\frac{dI_{gq}}{dt} + \omega_s L_g I_{gd} \end{aligned} \tag{84}$$

The synchronous transformation angle is the grid voltage angle θ_g . Similar to the DFIG dynamic model, cross coupling effect can be observed in (84), which can be eliminated by feedforward compensation terms expressed below for both dq - axis:

$$\begin{aligned} d-axis: &\qquad +V_{gd} - \omega_s L_g I_{gq} \\ q-axis: &\qquad +\omega_s L_g I_{gd} \end{aligned} \tag{85}$$

Assuming perfect decoupling, then the corresponding grid filter plant model can be derived from (84) as:

$$G(s) = \frac{I_{gdq}}{E_{gdq}} = \frac{1}{L_g s + R_g} \tag{86}$$

Grid active and reactive power with respect to grid dq currents can be derived from (28):

$$\begin{aligned} P_g &= \frac{3}{2}\left|\mathrm{r}V_g\right| I_{gd} \\ Q_g &= -\frac{3}{2}\left|\mathrm{r}V_g\right| I_{gq} \end{aligned} \tag{87}$$

Equation (87) shows decoupled active and reactive power control can be achieved on the grid side by regulating I_{gd} and I_{gq} respectively.

The transfer function in (86) serves as the starting point, where a similar design procedure as the one in section 3.8 can be carried out for both grid current and DC-link voltage controllers.

3.9.1 Grid current control

The analytical grid current controller, with active damping, is presented in Figure 3-11.

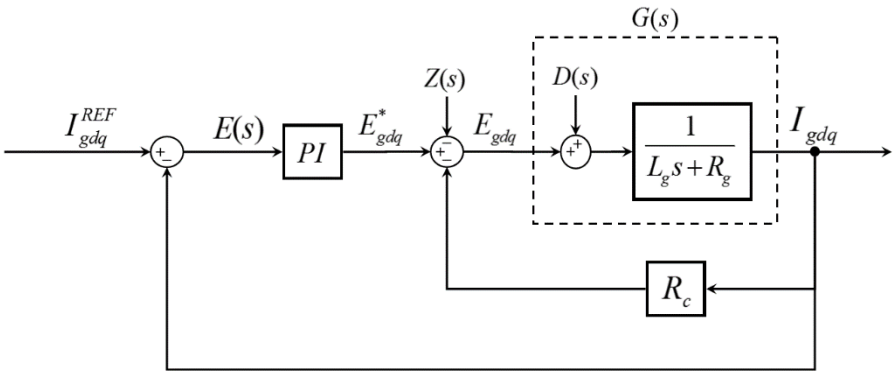

Figure 3-11: Analytical grid current controller

In this case, $D(s)$ and $Z(s)$ represents grid disturbances and feedforward compensation given in (85). The k_P, k_I gains for the PI compensator, as well as the grid current active damping term R_c can be computed as:

$$\begin{aligned} k_P &= \alpha_g L_g \\ k_I &= \alpha_g (R_g + R_c) \\ R_c &= \alpha_g L_g - R_g \end{aligned} \tag{88}$$

Where α_g is the closed loop bandwidth for the grid current controller limited by:

$$\alpha_{g\min} > \frac{R_g}{L_g} \tag{89}$$

The actual value selection for α_g can be done exactly as presented in (79).

3.9.2 DC-bus voltage control

The DC-bus voltage controller can be designed using (31), which can be simplified with grid voltage orientation as:

$$V_{dc} C_{dc} \frac{dV_{dc}}{dt} = P_r + \frac{3}{2} \left| \mathrm{r}_{V_g} \right| I_{gd} \tag{90}$$

The expression in (90) exhibits nonlinear dynamics due to the coexistence of V_{dc} and $\frac{dV_{dc}}{dt}$. Thus to facilitate a linear controller design, feedback linearization must be employed [11]. This is done by introducing a new state variable as:

$$W = V_{dc}^2 \tag{91}$$

Substituting (91) into (30) results in a DC-bus voltage dynamic model expressed as:

$$\frac{1}{2} C_{dc} \frac{dW}{dt} = P_r + \frac{3}{2} \left| \vec{V}_g \right| I_{gd} \tag{92}$$

Equation (92) is linear with respect to W , therefore the same IMC tuning process can be applied. The corresponding plant model for (92) can be derived as:

$$G(s) = \frac{W}{I_{gd}} = \frac{3\left| \vec{V}_g \right|}{C_{dc} s} \tag{93}$$

The resulting analytical DC-bus voltage controller, with feedback linearization and active damping is presented in Figure 3-12.

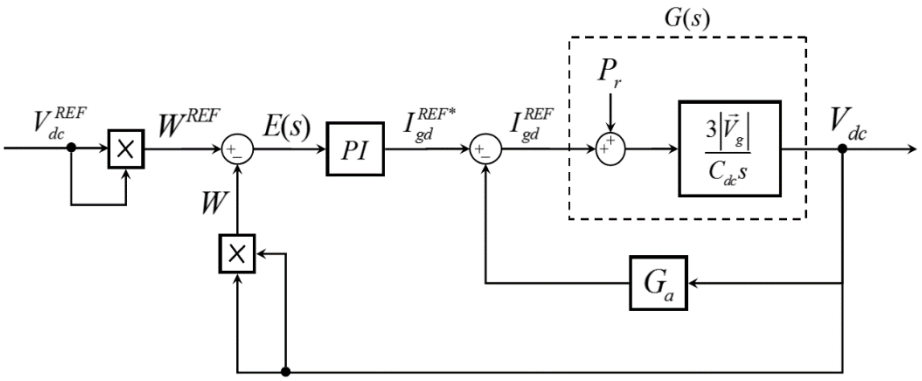

Figure 3-12: Analytical DC-link voltage controller

Again, the inner loop current dynamics are neglected assuming much slower outer loop dynamics. I_{gd}^{REF} is the reference signal for the inner loop d - axis current. The feedback linearization is realised by squaring V_{dc} and V_{dc}^{REF} . The k_P, k_I gains for the PI compensator, as well as the active damping term G_a can be computed as:

$$\begin{aligned} k_P &= \frac{C_{dc} \alpha_{dc}}{3\left| \vec{V}_g \right|} \\ k_I &= G_a \alpha_{dc} \\ G_a &= k_P \end{aligned} \tag{94}$$

To ensure slower outer loop dynamics, closed loop bandwidth for the DC-bus voltage controller α_{dc} must be chosen so that:

$$\alpha_{dc} \leq \frac{\alpha_g}{10} \tag{95}$$

4. Converter Modulation Algorithms

The vector controller outputs the reference voltage $\vec{V}_{ref}$ in the synchronous frame, which must be converted to PWM signals for both GSC and RSC IGBT's. Space vector PWM (SVPWM) is considered in this dissertation for converter modulation. This chapter describes the operating principles for both two-level and three-level voltage source converters (VSC), where corresponding SVPWM algorithms are then developed for each VSC topology. The emphasis is on the three-level VSC modulation due to its complexity, however a brief discussion on the two-level VSC is presented first.

4.1 Two-level converter operating principle

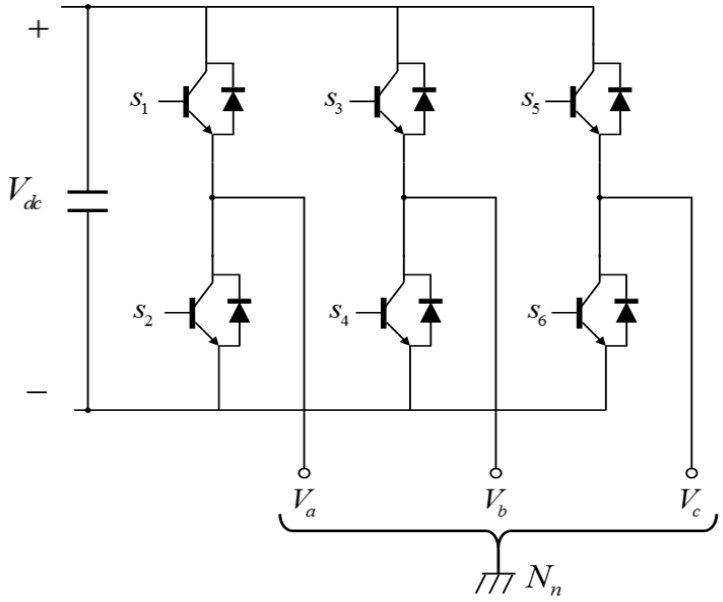

Figure 4-1: Two-level VSC circuit

Figure 4-1 illustrates the circuitry of a typical three-phase two-level VSC. Each leg of the VSC has two switches. Moreover, only one switch can be on at any given time to avoid a DC-bus short circuit. This leads to three switching signals for the top three switches denoted by s_1, s_3, s_5, whereas the bottom switching signals s_2, s_4, s_6 are just complimentary functions of the top PWM signals. The converter phase output voltage with respect to the load neutral N_n, can be expressed as a function of the DC-link voltage V_{dc} and s_1, s_3, s_5 as:

$$\begin{bmatrix} V_{aNn} \\ V_{bNn} \\ V_{cNn} \end{bmatrix} = \frac{V_{dc}}{3} \begin{bmatrix} 2 & -1 & -1 \\ -1 & 2 & -1 \\ -1 & -1 & 2 \end{bmatrix} \begin{bmatrix} s_1 \\ s_2 \\ s_3 \end{bmatrix} \tag{96}$$

Since the converter is controlled by the top switching signals which are binary in nature, therefore from (96) it can be seen that the two-level VSC has $2^3 = 8$ permutations of achievable output voltage states.

Applying the stationary transformation (18) to (96) results in discrete voltage space vectors forming a hexagon in the $\alpha\beta$ reference frame displayed in Figure 4-2

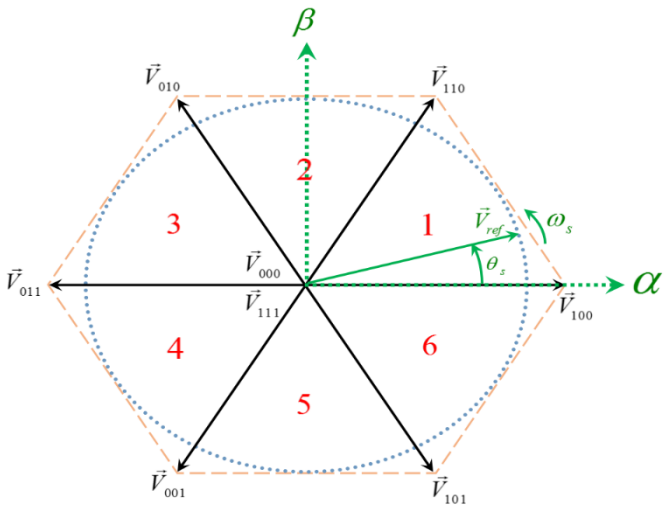

Figure 4-2: Two-level SV diagram

There are six active vectors ($\vec{V}_{100}, \vec{V}_{110}, \vec{V}_{010}, \vec{V}_{011}, \vec{V}_{001}, \vec{V}_{101}$) that separates the hexagon into six sectors. Two zero vectors ($\vec{V}_{000}, \vec{V}_{111}$) produces null current at the output of the two-level VSC. The ones and zeroes in the subscript represents the combination of switching signals required for each phase to produce the corresponding output voltage state.

4.2 Two-level space vector pulse width modulation

Using the Volt/Second balancing principle, $\vec{V}_{ref}$ can be approximated by its nearest three vectors (NTV's) as it rotates across all six sectors at an angular speed of ω_s. This is achieved by applying the PWM averaged voltage equation shown below [59]:

$$T_{samp}\vec{V}_{ref} = T_a\vec{V}_a + T_b\vec{V}_b + T_c\vec{V}_c \tag{97}$$

Controller sampling period T_{samp} must be sufficiently small for (97) to be accurate in its approximation. The selection of NTV's $\vec{V}_a, \vec{V}_b, \vec{V}_c$ is dependent on the sector in which $\vec{V}_{ref}$ lies. For example if $\vec{V}_{ref}$ is in sector one, then the NTV's are $\vec{V}_a = \vec{V}_{100}, \vec{V}_b = \vec{V}_{110}$ and $\vec{V}_c = \vec{V}_{000/111}$. The dwell times for the NTV's are represented by T_a, T_b, T_c, which should not have a combined duration that exceeds T_{samp}. The generic implementation of SVPWM for a two-level VSC, which can be found in literatures [24], [25], [59], has the following order of processing steps:

- Selection of NTV's ($\vec{V}_a, \vec{V}_b, \vec{V}_c$)
- Calculation of dwell time for NTV's (T_a, T_b, T_c)

- Optimal NTV's sequencing

The linear converter modulation range is defined by the largest circle that can be inscribed inside the hexagon shown in Figure 4-2. The magnitude invariant transformation adopted in this dissertation will result in an amplitude of $\frac{2}{3}V_{dc}$ for all the switching vectors, therefore the maximum voltage achievable by SVPWM within the linear modulation range can be expressed by:

$$\left|\vec{V}_{ref}\right| = m_a \frac{V_{dc}}{\sqrt{3}} \tag{98}$$

4.3 Three-level NPC converter operating principle

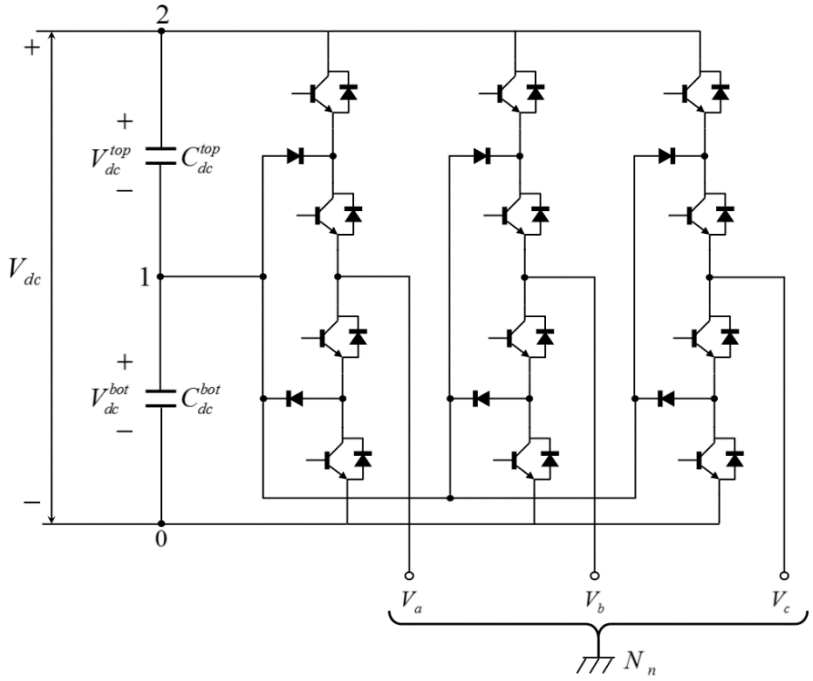

Figure 4-3: Three-level VSC circuit

Figure 4-3 illustrates the circuitry of a three-phase diode clamped three-level VSC. Each leg of the converter has four switches connected by two clamping diodes from midpoint to midpoint. Two consecutive IGBT's of each leg must be in the on-state at any given time, which results in a distinct voltage level from the series capacitors being connected to the output. These connections are described in Figure 4-3 by:

- '2' – VSC output connected to the DC-bus positive terminal, where the top two IGBT's are on.
- '1' – VSC output connected to the midpoint of DC-bus, where the two middle IGBT's are on.
- '0' – VSC output connected to the DC-bus negative terminal, where the bottom two IGBT's are on.

These connections can be mathematically expressed by [62]:

$$\sum_{j=0}^{2} s_{ij} = 1 \qquad i = \{a,b,c\} \tag{99}$$

The variable s_{ij} is a binary representation of the connection status on each leg of the three-level VSC. It will have a unity value if the i output is connected to the j point on the DC-bus. Referring all of the voltages to the negative DC-bus terminal ('0' reference), each output voltage consists of contributions from both, top and lower capacitors $C_{dc}^{top}, C_{dc}^{bot}$. Assuming the DC-bus is balanced (i.e. $V_{dc}^{top} = V_{dc}^{bot}$) then the phase output voltages can be expressed as:

$$V_{i0} = \frac{V_{dc}}{2} \sum_{j=0}^{2} j s_{ij} \qquad i = \{a,b,c\}$$
$$V_{dc}^{top} = V_{dc}^{bot} = \frac{V_{dc}}{2} \tag{100}$$

Three variations exists for both i and j, therefore the phase output voltage V_{i0} from a three-level VSC has $3^3 = 27$ permutations. Applying Clarke's transform to (99), the three-level space vector diagram in $\alpha\beta$ reference frame can be obtained. This is shown in Figure 4-4.

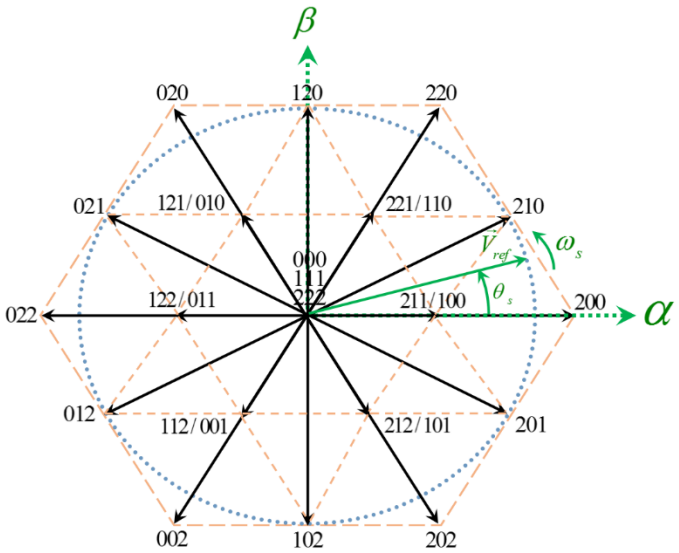

Figure 4-4: Three-level SV diagram

All the discrete voltage space vectors are labelled by their phase connection statuses with the DC-bus. For the three-level SV diagram, there are six sectors which can be individually divided into four regions to show the NTV's for $\vec{V}_{ref}$. There are four groups of three-level switching vectors which are described below:

- Large vectors ($\vec{V}_{200}, \vec{V}_{220}, \vec{V}_{020}, \vec{V}_{022}, \vec{V}_{002}, \vec{V}_{202}$) – these vectors connect phase output voltages to either positive or negative terminals of the DC-bus.

- Medium vectors ($\vec{V}_{210}, \vec{V}_{120}, \vec{V}_{021}, \vec{V}_{012}, \vec{V}_{102}, \vec{V}_{201}$) – these vectors individually connect phase output voltages to a different point on the DC-bus. One neutral point connection always exists.
- Short vectors ($\vec{V}_{100/211}, \vec{V}_{110/221}, \vec{V}_{010/121}, \vec{V}_{011/122}, \vec{V}_{001/112}, \vec{V}_{101/212}$) – these vectors consecutively connect two phase output voltages to a single point on the DC-bus. At least one neutral point connection exists. They are vector pairs, which means that two different switching states of the three-level VSC can achieve the same phase output voltage.
- Zero vectors ($\vec{V}_{000}, \vec{V}_{111}, \vec{V}_{222}$) – these vectors connect all of the phase output voltages to a single point on the DC-bus, thus null current results for the load.

One major drawback in implementing a three-level VSC is the occurrence of DC-link neutral point voltage unbalance [26], [62]–[64]. The VSC output connection to the midpoint of the DC-bus causes neutral current to flow, if left unchecked this could lead to complete discharge in one of the DC-link capacitors. Modulation algorithms for a three-level VSC should take this negative effect into account in order to prevent potential instabilities in the DC voltage controller.

4.4 Three-level NPC space vector pulse width modulation

The Volt/Second balancing principle discussed in section 4.2 can be equally applied for three-level SVPWM. Dwell times for each vector of the NTV's can be calculated based on trigonometric relations between $\vec{V}_{ref}$ and θ_s. In the case for a three-level VSC, NTV's must be selected based on the sector as well as regional positions of $\vec{V}_{ref}$ in Figure 4-4. This will lead to a large number of variations for dwell time calculations where complex trigonometric equations are involved. Thus, the algorithm is computationally taxing and practically difficult to implement for digital hardware such as an FPGA. In order to simplify the implementation of three-level SVPWM, a novel dwell time calculation method in [26] is presented here where its key principles are detailed in the following subsections.

4.4.1 Duty cycle calculation by projection

The Volt/Second balancing principle states that any reference vector can be approximated by three adjacent vectors in the same plane, using the PWM averaged expression shown in (97). In addition, the reference vector must lie in the triangular boundary formed by the adjacent vectors. Such a region is shown in Figure 4-5.

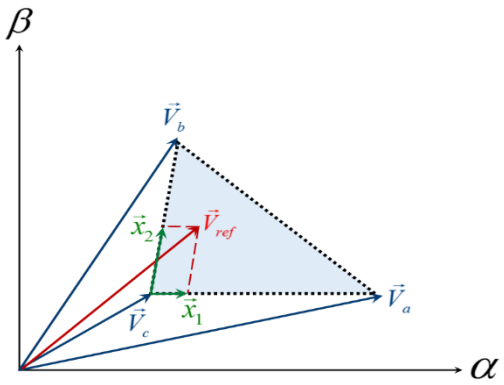

Figure 4-5: Limiting area for $\vec{V}_{ref}$

The reference voltage vector $\vec{V}_{ref}$ can be projected onto the boundary formed by $\vec{V}_a - \vec{V}_c$ and $\vec{V}_b - \vec{V}_c$ resulting in $\vec{x}_1$ and $\vec{x}_2$ respectively. Therefore, $\vec{V}_{ref}$ can be expressed by the following vector summation as:

$$\vec{V}_{ref} = \vec{x}_1 + \vec{x}_2 + \vec{V}_c \tag{101}$$

Equation (101), after some algebraic manipulation, can also be expressed as:

$$\vec{V}_{ref} = x_1 \frac{\vec{V}_a - \vec{V}_c}{l_1} + x_2 \frac{\vec{V}_b - \vec{V}_c}{l_2} + \vec{V}_c \tag{102}$$

The terms $\frac{\vec{V}_a - \vec{V}_c}{l_1}$ and $\frac{\vec{V}_b - \vec{V}_c}{l_2}$ are unit vectors that contain directional information of $\vec{x}_1$ and $\vec{x}_2$ respectively. The variables x_1 and x_2 are scalar magnitudes of the vector projections. Expression (102) can be rearranged resulting in the following:

$$\vec{V}_{ref} = \frac{x_1}{l_1}\vec{V}_a + \frac{x_2}{l_2}\vec{V}_b + \left(1 - \frac{x_1}{l_1} - \frac{x_2}{l_2}\right)\vec{V}_c \tag{103}$$

The coefficients $\frac{x_1}{l_1}$, $\frac{x_2}{l_2}$ and $\left(1 - \frac{x_1}{l_1} - \frac{x_2}{l_2}\right)$ in (103) are per unit quantities which actually represents duty cycles when compared to (97). This leads to the following relation between dwell times and $\vec{V}_{ref}$ projections:

$$d_a = \frac{x_1}{l_1} = \frac{T_a}{T_{samp}}$$

$$d_b = \frac{x_2}{l_2} = \frac{T_b}{T_{samp}} \tag{104}$$

$$d_c = 1 - \frac{x_1}{l_1} - \frac{x_2}{l_2} = \frac{T_c}{T_{samp}}$$

The limiting area in Figure 4-5 can be related to a single sector in the three-level SV diagram. Assuming the DC-bus voltages are balanced and the system is normalised to a two per unit base, then the regions in a sector would be equilateral triangles with unit lengths. Therefore the duty cycles d_a, d_b, d_c expressed in (104) can be simplified to:

$$l_1 = l_2 = 1$$

$$d_a = x_1$$

$$d_b = x_2 \tag{105}$$

$$d_c = 1 - x_1 - x_2$$

To demonstrate the duty cycle calculations process, sector one of the three-level SV diagram is presented in detail as shown in Figure 4-6.

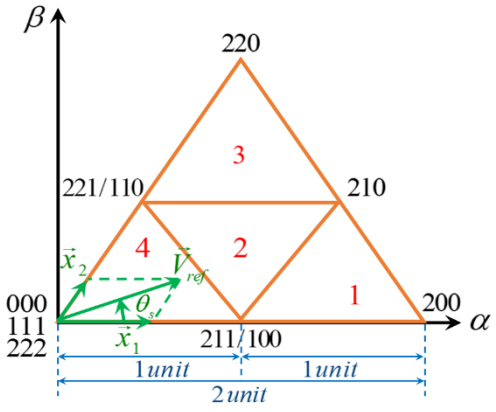

Figure 4-6: Sector one of the SV diagram

The regions are numerically labelled $1-4$. Consider the case where $\vec{V}_{ref}$ lies in region 4, the corresponding NTV's should be selected so that $\vec{V}_a = \vec{V}_{211/100}, \vec{V}_b = \vec{V}_{221/110}$ and $\vec{V}_c = \vec{V}_{111}$. The vector projections of $\vec{V}_{ref}$ coincides with the regional boundary, therefore corresponding duty cycles for the NTV's can then be computed using (105) exactly. Figure 4-7 shows the cases when $\vec{V}_{ref}$ lies in regions 1, 2 and 3.

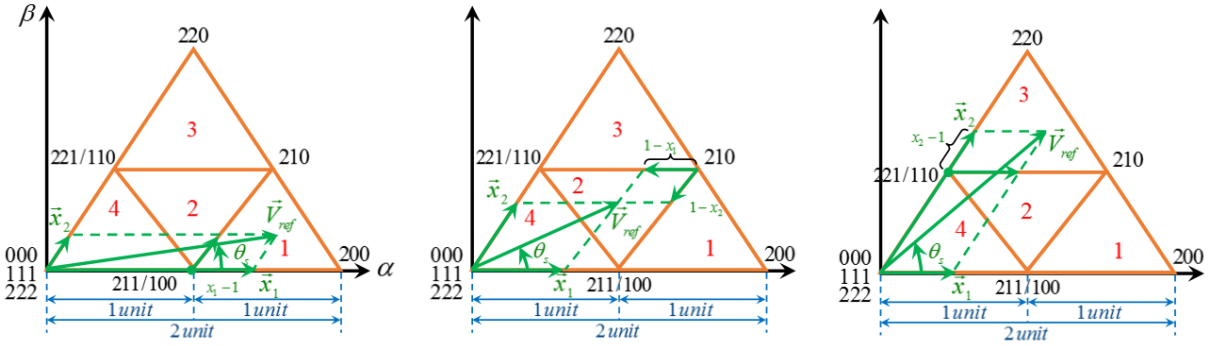

Figure 4-7: Cases where $\vec{V}_{ref}$ lies in regions 1, 2 and 3

It should be noted that the sector length is normalised to two per unit, this is done in order to facilitate the simplification presented in (105). The region where $\vec{V}_{ref}$ lies can be directly determined from x_1 and x_2. Duty cycle calculations and NTV selections for the first sector is summarised in Table 4-1.

Table 4-1: Summary of duty cycle calculations in sector one

Case	Region	NTV's	Duty Cycles
$x_1 > 1$	1	$\vec{V}_a = \vec{V}_{200}$ $\vec{V}_b = \vec{V}_{210}$ $\vec{V}_c = \vec{V}_{100/211}$	$d_a = x_1 - 1$ $d_b = x_2$ $d_c = 1 - d_a - d_b$
$x_1 \le 1$ $x_2 \le 1$ $x_1 + x_2 > 1$	2	$\vec{V}_a = \vec{V}_{100/211}$ $\vec{V}_b = \vec{V}_{110/221}$ $\vec{V}_c = \vec{V}_{210}$	$d_a = 1 - x_2$ $d_b = 1 - x_1$ $d_c = 1 - d_a - d_b$
$x_2 > 1$	3	$\vec{V}_a = \vec{V}_{210}$ $\vec{V}_b = \vec{V}_{220}$ $\vec{V}_c = \vec{V}_{110/221}$	$d_a = x_1$ $d_b = x_2 - 1$ $d_c = 1 - d_a - d_b$
$x_1 \le 1$ $x_2 \le 1$ $x_1 + x_2 \le 1$	4	$\vec{V}_a = \vec{V}_{100/211}$ $\vec{V}_b = \vec{V}_{110/221}$ $\vec{V}_c = \vec{V}_{111}$	$d_a = x_1$ $d_b = x_2$ $d_c = 1 - d_a - d_b$

Since the sum of dwell times cannot exceed the controller sampling period, therefore the sum of x_1 and x_2 cannot be greater than two. This will ensure the modulation of $\vec{V}_{ref}$ to stay within linear range.

4.4.2 Sector one equivalence

If we consider the symmetry that exists in the SV diagram, it can be deduced that a sector one equivalent vector can be found for $\underset{1}{V}_{ref}$ when it lies in any of the other sectors. This concept is demonstrated with the aid of Figure 4-8.

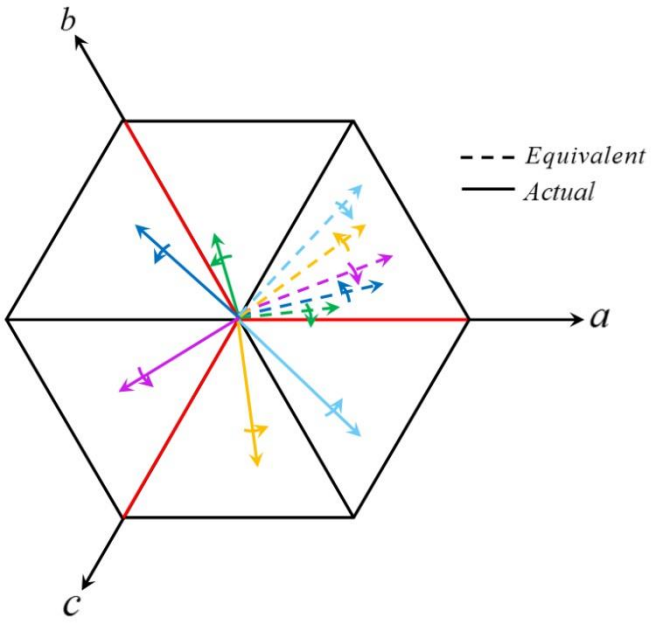

Figure 4-8: Sector one equivalences for $\underset{1}{V}_{ref}$

The equivalent transformation can be implemented by simply interchanging a,b,c variables before applying Clarke's transformation to the reference voltage. A physical interpretation of this is that the base axis of each sector is rotated in such a way, so as to coincide with the a - axis that is the base for sector one. For example if $\underset{1}{V}_{ref}$ is in sector two, then b - axis must first rotate clockwise by $\frac{2\pi}{3}$ radians then reflected about a - axis. The resulting sector one equivalent vector for $\underset{1}{V}_{ref}$ would then have its natural reference frame components V_a and V_b interchanged where V_c remains the same. Table 4-2 summarises all the equivalent variable interchanges for $\underset{1}{V}_{ref}$ in sector 1-6.

Table 4-2: Variable interchanges for sector one equivalent $\dot{V}_{ref}^{1}$

Sector	Variable Interchange
1	$a \rightarrow a$ $b \rightarrow b$ $c \rightarrow c$
2	$a \rightarrow b$ $b \rightarrow a$ $c \rightarrow c$
3	$a \rightarrow c$ $b \rightarrow a$ $c \rightarrow b$
4	$a \rightarrow c$ $b \rightarrow b$ $c \rightarrow a$
5	$a \rightarrow b$ $b \rightarrow c$ $c \rightarrow a$
6	$a \rightarrow a$ $b \rightarrow c$ $c \rightarrow b$

By defining a sector one equivalent vector for $\dot{V}_{ref}^{1}$, all modulation can be carried out in sector one where $\dot{V}_{ref}^{1}$ sector position in the SV diagram do not influence duty cycle calculations. This simplifies the process as Table 4-1 can be exclusively used for all duty cycle related computations.

4.4.3 Determination of reference vector projections x_1 and x_2

So far it is shown that duty cycles for the NTV's can be calculated by vector projections of $\dot{V}_{ref}^{1}$. The projection lengths x_1 and x_2 can be calculated based on the trigonometric relation between $\dot{V}_{ref}^{1}$ and θ_s. However, since trigonometric equations are complex and time varying, this exacerbates the computation requirement issue for the three-level SVPWM. An interesting method presented in [62] eliminates these trig equations for duty cycle calculations. This method expresses $\dot{V}_{ref}^{1}$ on a new set of axis, known as the gh reference frame. These axis are 60^o apart which coincide with the boundaries of sector one in the SV diagram. Figure 4-9 shows a graphical presentation of the gh reference frame.

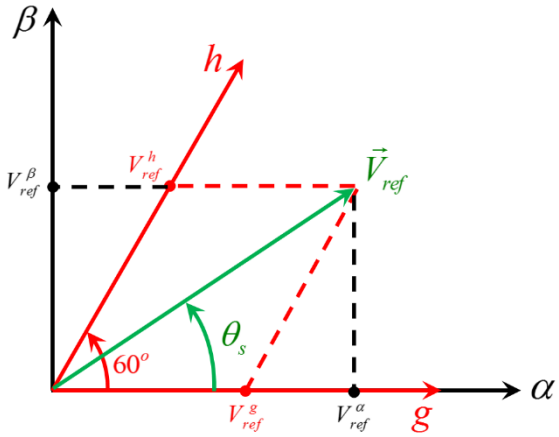

Figure 4-9: Graphical presentation of gh reference frame

A quick comparison between Figure 4-6 and Figure 4-9 shows that x_1 and x_2 can be directly found from the gh coordinates of $\vec{V}_{ref}$, denoted by V_{ref}^{g} and V_{ref}^{h}. The dependence on θ_s can thus be eliminated from duty cycle calculations. Since the vector controller provides $\vec{V}_{ref}$ in the synchronous frame, its dq components must be transformed onto the gh - axis by [26]:

$$\begin{bmatrix} g \\ h \end{bmatrix} = \frac{2}{V_{dc}} \begin{bmatrix} \sin(\theta_e + \frac{2\pi}{3}) & \cos(\theta_e + \frac{2\pi}{3}) \\ \sin(\theta_e) & \cos(\theta_e) \end{bmatrix} \begin{bmatrix} d \\ q \end{bmatrix} \tag{106}$$

The coefficient $\frac{2}{V_{dc}}$ in (106) is derived in such a way so that $\vec{V}_{ref}$ will be normalised to a two per unit SV diagram. Figure 4-10 illustrates this transformation.

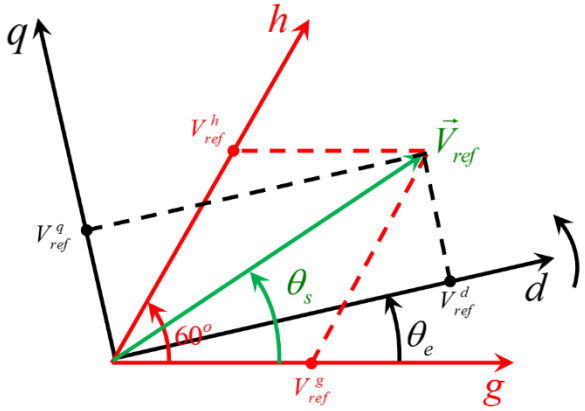

Figure 4-10: Graphical presentation of $dq - gh$ transformation

The transformation angle θ_e in (106) will be equal to θ_s if $\vec{V}_{ref}$ is initially aligned with the synchronous d-axis. This is actually most often the case when grid voltage orientation is adopted. For the purpose of demonstration, these two angles are shown to be different here.

From the values of V_{ref}^{g} and V_{ref}^{h}, the sector where the reference vector lies can be directly found, as can the vector projections x_1 and x_2 of the equivalent reference vector in the first sector. These relationships are illustrated and summarised in Figure 4-11 and Table 4-3 respectively.

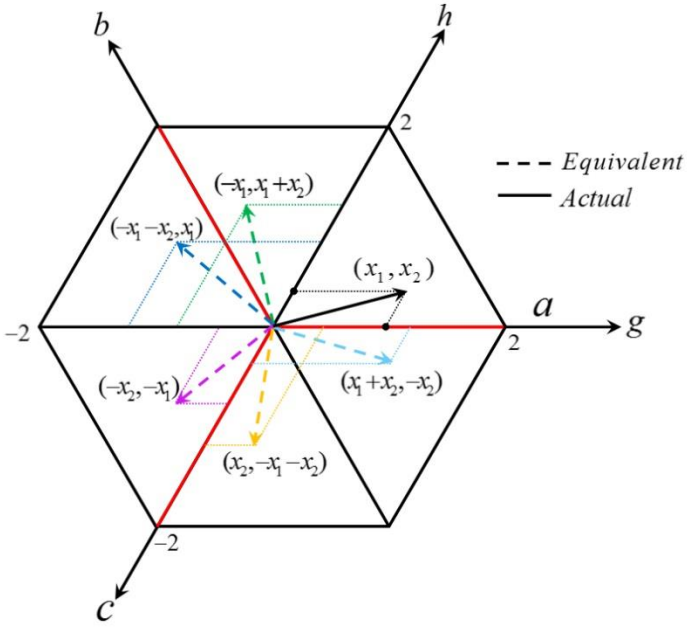

Figure 4-11: $\underset{\iota}{V}_{ref}$ sector one equivalent vector components in gh reference frame

Table 4-3: Sector selection and equivalent vector projections x_1, x_2 in sector one based on V_{ref}^{g}, V_{ref}^{h}

gh **Component Logic**	**Sector**	**Equivalent x_1, x_2 in sector one**
$V_{ref}^{g} \geq 0 \quad V_{ref}^{h} \geq 0$	1	$x_1 = V_{ref}^{g} \quad x_2 = V_{ref}^{h}$
$V_{ref}^{g} < 0 \quad V_{ref}^{h} \geq 0 \quad (V_{ref}^{g} + V_{ref}^{h}) \geq 0$	2	$x_1 = -V_{ref}^{g} \quad x_2 = V_{ref}^{g} + V_{ref}^{h}$
$V_{ref}^{g} < 0 \quad V_{ref}^{h} \geq 0 \quad (V_{ref}^{g} + V_{ref}^{h}) < 0$	3	$x_1 = V_{ref}^{h} \quad x_2 = -V_{ref}^{g} - V_{ref}^{h}$
$V_{ref}^{g} < 0 \quad V_{ref}^{h} < 0$	4	$x_1 = -V_{ref}^{h} \quad x_2 = -V_{ref}^{g}$
$V_{ref}^{g} \geq 0 \quad V_{ref}^{h} < 0 \quad (V_{ref}^{g} + V_{ref}^{h}) < 0$	5	$x_1 = -V_{ref}^{g} - V_{ref}^{h} \quad x_2 = V_{ref}^{g}$
$V_{ref}^{g} \geq 0 \quad V_{ref}^{h} < 0 \quad (V_{ref}^{g} + V_{ref}^{h}) \geq 0$	6	$x_1 = V_{ref}^{g} + V_{ref}^{h} \quad x_2 = -V_{ref}^{h}$

Duty cycle calculations carried out by using Table 4-1 and Table 4-3 only consists of logic, add and subtract functions, which can be implemented on digital electronics with ease. However, the $dq-gh$ transformation detailed in (106) must be applied to $\underset{\iota}{V}_{ref}$ first.

4.4.4 Sequencing and modulation consideration

Once the duty cycles are calculated, the actual sequencing for the NTV's must be defined. This should be performed to ensure minimum state transitions within one sampling period T_{samp}. The additional

issue with respect to neutral point voltage unbalance must be considered too. As discussed previously, short vectors are double vectors that produce the same VSC output voltage. These vectors introduce a second degree of design freedom for NTV sequencing determinations. If this is properly utilised, neutral point balance can be achieved [26], [64]. To demonstrate the effect of short vector selection on neutral point balancing, Figure 4-12 shows the three-level VSC output dynamics when either $\underline{\vec{V}}_{100}$ or $\underline{\vec{V}}_{211}$ from the short vector pair $\underline{\vec{V}}_{100/211}$ is applied.

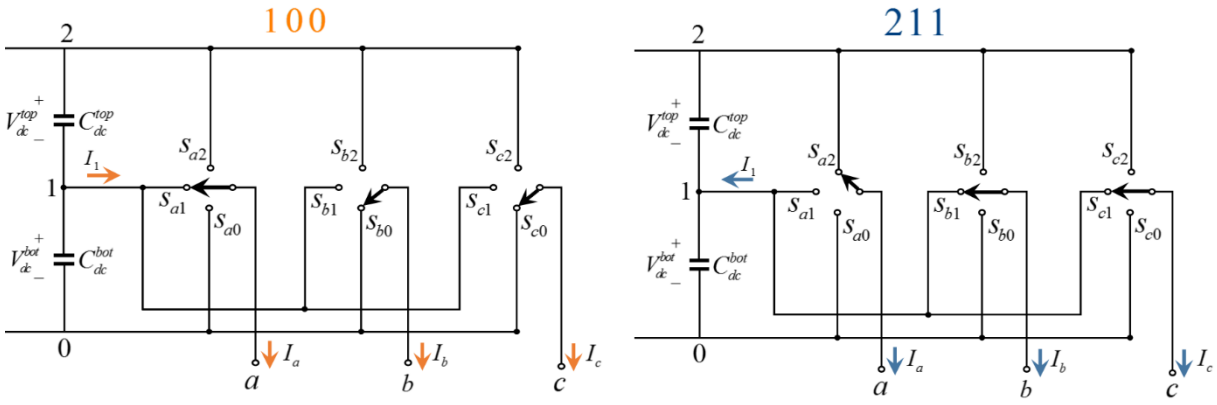

Figure 4-12: Selection of $\underline{\vec{V}}_{100/211}$ and its effect on DC neutral point voltage balance

Since short vectors connect at least one of the output terminals to the neutral point, there will be a neutral current I_1 given that load currents I_a, I_b, I_c are non-zero. When $\underline{\vec{V}}_{100}$ is applied, assuming a positive load current (i.e. away from DC-bus), output a is connected to '1' and thus $I_1 = I_a$. The bottom capacitor C_{dc}^{bot} will discharge due to the positive I_1, therefore V_{dc}^{bot} will decrease. Note the top capacitor C_{dc}^{top} will charge due to its polarity with respect to the neutral point, hence the total V_{dc} remains the same. In the case that $\underline{\vec{V}}_{211}$ is applied, outputs b and c are connected to '1' and thus $I_1 = I_b + I_c = -I_a$. The bottom capacitor C_{dc}^{bot} will charge due to the negative I_1, therefore V_{dc}^{bot} will increase.

The above analysis can be performed for all short vector pairs, and a conclusion can be reached that:

- Each short vector pair consists of two vectors that individually influence the DC-bus neutral point voltage in opposite directions.
- The polarity of the neutral point current caused by applying short vectors depends on the load current direction.

In order to select short vectors for achieving neutral point voltage balance, the imbalance between V_{dc}^{bot} and V_{dc}^{top} as well as the instantaneous direction of I_a and I_c must be known. All of the modulation is carried out in sector one based on the discussion in subsection 4.4.2, therefore only short vector pairs $\underline{\vec{V}}_{100/211}$ and $\underline{\vec{V}}_{110/221}$ need to be considered. However, the load current must be transformed to their first

sector equivalent. This can be done using the relationship demonstrated in Table 4-2. The logic for short vector selection based on $V_{dc}^{bot}, V_{dc}^{top}, I_a^{'}, I_c^{'}$ are presented in Table 4-4.

Table 4-4: Short vector selection in sector one

Selection for $\vec{V}_{100/211}$			**Selection for** $\vec{V}_{110/221}$		
$V_{dc}^{bot} > V_{dc}^{top}$	$I_a^{'} > 0$	**Select**	$V_{dc}^{bot} > V_{dc}^{top}$	$I_c^{'} > 0$	**Select**
0	0	$\vec{V}_{100}$	0	0	$\vec{V}_{221}$
0	1	$\vec{V}_{211}$	0	1	$\vec{V}_{110}$
1	0	$\vec{V}_{211}$	1	0	$\vec{V}_{110}$
1	1	$\vec{V}_{100}$	1	1	$\vec{V}_{221}$

It should be noted that $I_a^{'}$ and $I_c^{'}$ here represents the first sector equivalences for I_a and I_c respectively. Following short vector selections, the next step is to determine the actual sequence for the NTV's which depends on the short vectors selected. Table 4-5 provides a summary of NTV sequencing that can minimize state transitions the most for approximating $\vec{V}_{ref}$ in the first sector.

Table 4-5: NTV sequence look-up table for sector one

Region	**Short Vectors**	**NTV Sequence**	**State Transitions**
1	$\vec{V}_{100}$	$\vec{V}_{100}$ - $\vec{V}_{200}$ - $\vec{V}_{210}$ // $\vec{V}_{210}$ - $\vec{V}_{200}$ - $\vec{V}_{100}$	2//2
	$\vec{V}_{211}$	$\vec{V}_{200}$ - $\vec{V}_{210}$ - $\vec{V}_{211}$ // $\vec{V}_{211}$ - $\vec{V}_{210}$ - $\vec{V}_{200}$	2//2
2	$\vec{V}_{100}$ - $\vec{V}_{110}$	$\vec{V}_{100}$ - $\vec{V}_{110}$ - $\vec{V}_{210}$ // $\vec{V}_{210}$ - $\vec{V}_{110}$ - $\vec{V}_{100}$	2//2
	$\vec{V}_{100}$ - $\vec{V}_{221}$	$\vec{V}_{100}$ - $\vec{V}_{210}$ - $\vec{V}_{221}$ // $\vec{V}_{221}$ - $\vec{V}_{210}$ - $\vec{V}_{100}$	4//4
	$\vec{V}_{211}$ - $\vec{V}_{110}$	$\vec{V}_{110}$ - $\vec{V}_{210}$ - $\vec{V}_{211}$ // $\vec{V}_{211}$ - $\vec{V}_{210}$ - $\vec{V}_{110}$	2//2
	$\vec{V}_{211}$ - $\vec{V}_{221}$	$\vec{V}_{210}$ - $\vec{V}_{211}$ - $\vec{V}_{221}$ // $\vec{V}_{221}$ - $\vec{V}_{211}$ - $\vec{V}_{210}$	2//2
3	$\vec{V}_{110}$	$\vec{V}_{110}$ - $\vec{V}_{210}$ - $\vec{V}_{220}$ // $\vec{V}_{220}$ - $\vec{V}_{210}$ - $\vec{V}_{110}$	2//2
	$\vec{V}_{221}$	$\vec{V}_{210}$ - $\vec{V}_{220}$ - $\vec{V}_{221}$ // $\vec{V}_{221}$ - $\vec{V}_{220}$ - $\vec{V}_{210}$	2//2
4	$\vec{V}_{100}$ - $\vec{V}_{110}$	$\vec{V}_{100}$ - $\vec{V}_{110}$ - $\vec{V}_{111}$ // $\vec{V}_{111}$ - $\vec{V}_{110}$ - $\vec{V}_{100}$	2//2
	$\vec{V}_{100}$ - $\vec{V}_{221}$	$\vec{V}_{100}$ - $\vec{V}_{111}$ - $\vec{V}_{221}$ // $\vec{V}_{221}$ - $\vec{V}_{111}$ - $\vec{V}_{100}$	4//4
	$\vec{V}_{211}$ - $\vec{V}_{110}$	$\vec{V}_{110}$ - $\vec{V}_{111}$ - $\vec{V}_{211}$ // $\vec{V}_{211}$ - $\vec{V}_{111}$ - $\vec{V}_{110}$	2//2
	$\vec{V}_{211}$ - $\vec{V}_{221}$	$\vec{V}_{111}$ - $\vec{V}_{211}$ - $\vec{V}_{221}$ // $\vec{V}_{221}$ - $\vec{V}_{211}$ - $\vec{V}_{111}$	2//2

It can be seen that short vector selections in region 2 ($\vec{V}_{100}$ - $\vec{V}_{221}$) and region 4 ($\vec{V}_{100}$ - $\vec{V}_{221}$) produce NTV sequences that results in more state transitions when compared to the rest. Therefore, the switching frequency for the three-level VSC will only be quasi-constant during steady state conditions.

When the NTV's have been selected and the most suitable sequence defined, the final step is to apply the calculated duty cycles to corresponding NTV's. This task requires the knowledge of the real sector

where $\vec{V}_{ref}$ lies, and it can be performed by inversely interchanging the states of the output phases in accordance with the relationship given in Table 4-2. The entire three-level SVPWM procedure presented in this chapter is summarised and illustrated by the flow chart shown in Figure 4-13.

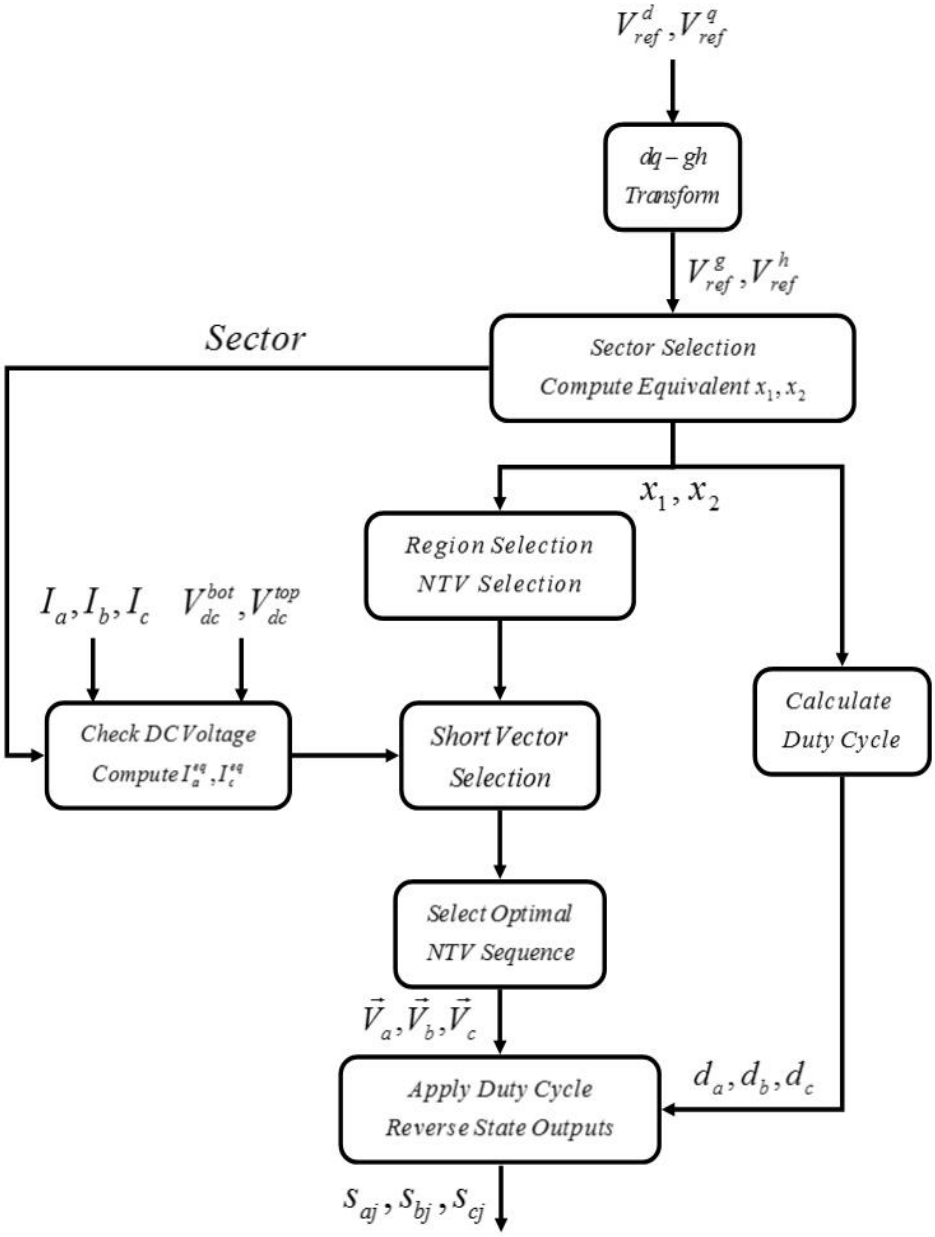

Figure 4-13: Summary for the three-level SVPWM

4.5 Advantages and disadvantages of two-level and three-level PWM converters

The research conducted in this chapter detailed the operating principles and implementation for both two-level and three-level converters. It was decided that both converter types are to be used for the practical implementation of the system in this thesis. However, the advantages and drawbacks for both converter topologies should be considered when deciding their application in the real world. Table 4-6 below shows a summary of advantages and disadvantages for both two-level and three-level converter applications.

Table 4-6: Advantages and Disadvantages of PWM Converters

Converter Type	Advantages	Disadvantages
2-level	• Simple circuitry • Less components • Easy implementation • Cheaper compared to three-level converters	• Higher component rating requirements • Poor output power quality
3-level	• Reduced component rating requirements • Improved output power quality	• More components • Complex implementation • More expensive compared to two-level converters • DC-link neutral voltage unbalance issues

5. DFIG Soft Grid Synchronisation

This chapter presents the process in which the rotor current controller is modified to enable soft synchronisation of the DFIG with the grid. In addition, stator current transients caused by controller feedforward mismatch during synchronization is also investigated.

5.1 DFIG open stator dynamics

Soft synchronisation of the DFIG with the grid requires that the initial voltage at the open stator terminals are exactly the same as the grid voltage. The DFIG model derived in section 2.3 must be adjusted according to its open stator dynamics in order to facilitate a soft synchronisation controller design.

There will be no current flow in the windings when the stator is open circuited, therefore the dynamic model in (21) can be expressed as:

$$\begin{gathered} \underline{I}_s = 0 \\ \therefore \underline{\phi}_s = L_m \underline{I}_r \qquad \underline{\phi}_r = L_r \underline{I}_r \\ \therefore \underline{V}_s = L_m \frac{d\underline{I}_r}{dt} + j\omega_s L_m \underline{I}_r \qquad \underline{V}_r = R_r \underline{I}_r + L_r \frac{d\underline{I}_r}{dt} + j\omega_{slip} L_r \underline{I}_r \end{gathered} \tag{107}$$

Observing (107) we see that when the stator is open, magnetization of the machine is solely dependent on rotor currents. The stator and rotor flux components, $\underline{\phi}_s$ and $\underline{\phi}_r$, are collinear with rotor current $\underline{I}_r$. A quadrature $\underline{V}_s$ is thus induced at the stator terminals when the machine is in steady state, where $\frac{d\underline{I}_r}{dt} = 0$. The space vector diagram that sums up DFIG open stator dynamics in (107), with grid voltage orientation, is shown in Figure 5-1.

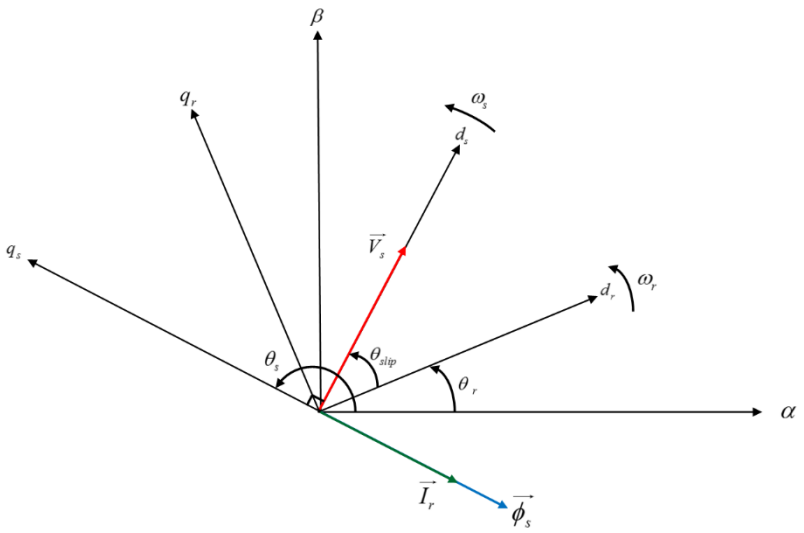

Figure 5-1: Open stator vector diagram

A stator voltage equal to the grid voltage must be induced. This objective is achieved if $\vec{V}_s$ satisfies the following condition:

$$\vec{V}_s = \vec{V}_g \tag{108}$$

It can be assumed that at the instant before DFIG grid connection, the machine is in steady state. By inspecting (65), (107) and (108), the rotor current that is responsible for inducing the stator voltage must then satisfy the following condition:

$$I_{rd} = 0 \qquad I_{rq} = -\frac{\left|\vec{V}_g\right|}{\omega_s L_m} \tag{109}$$

Setting the rotor dq current components to the expressions given in (109) will result in $\vec{V}_s = \vec{V}_g$. The goal of soft synchronization is to reduce excessive energy surges within the stator of the machine during grid connection, therefore the stator active and reactive power dynamics should be investigated. For ease of presentation, the stator power expressions given in (72) is presented here again:

$$P_s = -\frac{3}{2}\left|\vec{V}_g\right|\frac{L_m}{L_s} I_{rd}$$

$$Q_s = \frac{3}{2L_s}\left(\frac{\left|\vec{V}_g\right|^2}{\omega_s} + \left|\vec{V}_g\right| L_m I_{rq}\right)$$

It can be noted that both P_s and Q_s yields 0 if the rotor current condition in (109) is met. This shows that zero power exchange between stator and grid is guaranteed after synchronization.

Using the same procedure described in section 3.7, the rotor dynamic equation in (107) can be resolved into its dq components as:

$$V_{rd} = R_r I_{rd} + L_r \frac{dI_{rd}}{dt} - \omega_{slip} L_r I_{rq}$$
$$V_{rq} = R_r I_{rq} + L_r \frac{dI_{rq}}{dt} + \omega_{slip} L_r I_{rd} \tag{110}$$

The corresponding DFIG rotor process model, for the open stator condition, can be derived as:

$$G(s) = \frac{1}{L_r s + R_r} \tag{111}$$

5.2 Effect of changing rotor dynamics on grid connection

Comparing (110) and (67), it is obvious that rotor electrical dynamics is different during soft synchronization and normal operation of the DFIG. The main difference lies in that the rotor electrical time constant for normal operation $\frac{L_\sigma}{R_r}$ changes to $\frac{L_r}{R_r}$ during synchronization, and the d-axis back-EMF component $\omega_{slip} \frac{L_m \dot{\phi}_s}{L_s}$ do not exist when the stator is open. The back-EMF can be considered as a constant disturbance on the rotor d-axis current given that the grid is stiff.

It is important to note that the aforementioned differences occur if there are non-zero currents in the stator. Ideally there should be no power exchange between the machine and grid at the instant of connection, then there should be no change in dynamics between the two modes of operation. However, in reality that is rarely the case especially during the moment of synchronisation, since a slight imbalance between $\dot{V}_g$ and $\dot{V}_s$ can cause large transients in $\dot{I}_s$. Therefore, the controller should be designed separately for both normal and synchronising operations.

The synchronisation controller should cater for changing electrical dynamics of the rotor, as well as the addition of back-EMF which contributes toward stator current transients at the point of connection due to its higher magnitude. Generally this back-EMF component is compensated by an approximated feedforward term shown in (68), therefore a smooth synchronization is highly dependent on the numerical accuracy of this approximation. Assuming there is a slight offset between the feedforward compensation and the actual EMF, the difference between the two will be seen by the rotor d-axis as a step disturbance at the instant of DFIG synchronisation. Since $\dot{V}_s$ is initially induced by regulating I_{rq}, therefore a d-axis disturbance may introduce a phase shift in $\dot{V}_s$ with respect to $\dot{V}_g$ during

synchronisation which in turn may cause current transients that are proportional to the error in the feedforward approximation.

5.3 Synchronisation rotor current control

The rotor circuit dynamics are different between normal and synchronising operations of the DFIG. The synchronisation rotor current controller must be designed using the process model in (111). After the connection between grid and DFIG is made, then the rotor current controller must be switched from synchronisation control to normal mode. The rotor current controller schemes for both DFIG operation modes are shown in Figure 5-2 and Figure 5-3 below.

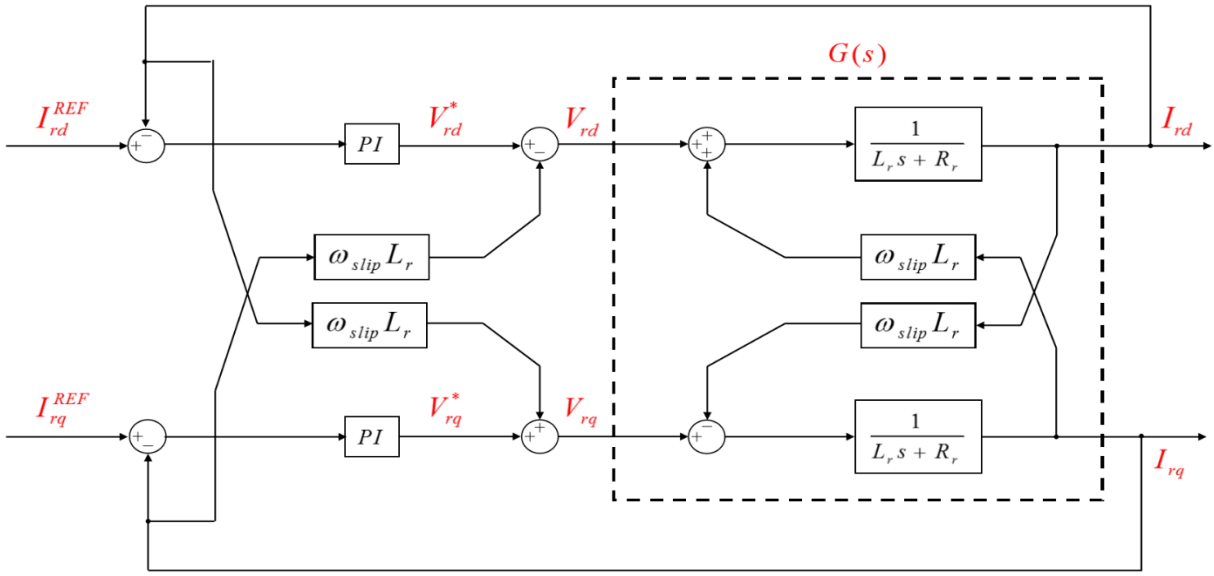

Figure 5-2: DFIG soft synchronisation controller

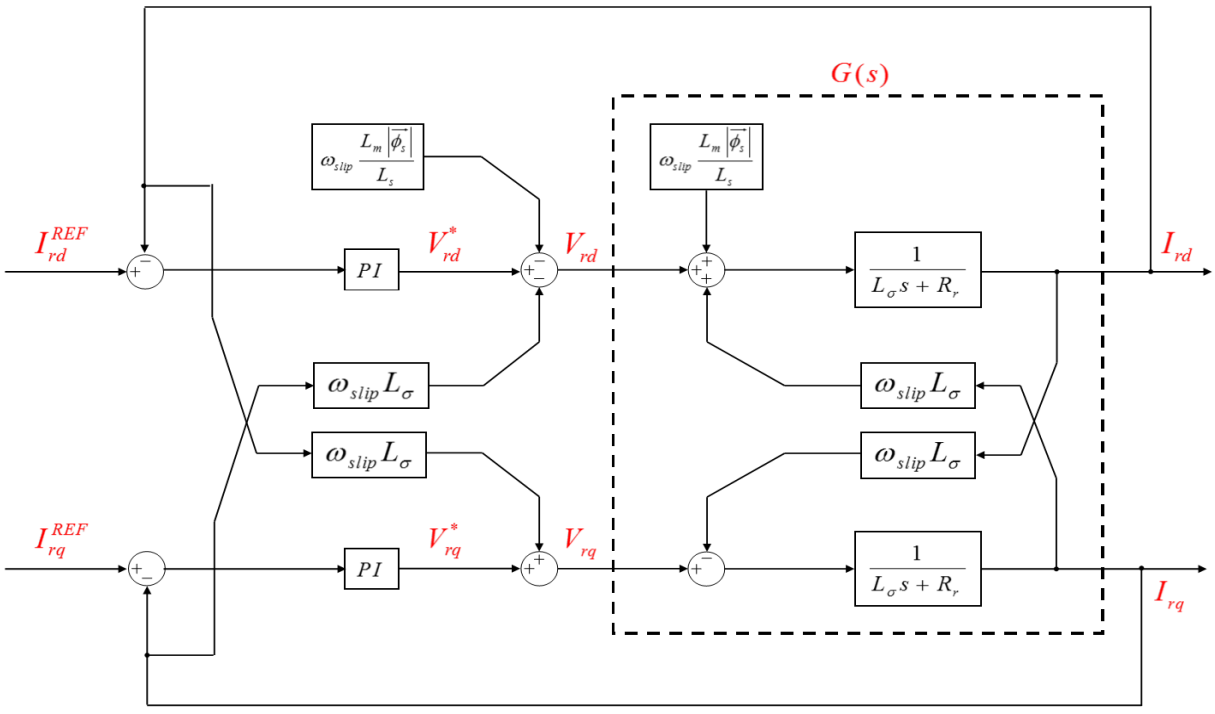

Figure 5-3: DFIG normal operation controller

The most distinct difference between the above two controller structures is that the process plant has different parameters, which would result in different gain values for the PI compensators. Moreover, different feedforward decoupling terms must also be applied. The PI compensator gains for the soft synchronisation controller can be computed using the same IMC tuning technique detailed in section 3.8. These equations are given as:

$$\begin{aligned} k_P &= \alpha_{soft} L_r \\ k_I &= \alpha_{soft}(R_r + R_a) \\ R_{soft} &= \alpha_{soft} L_r - R_r \end{aligned} \tag{112}$$

The closed loop bandwidth α_{soft} for the soft synchronisation controller is limited by:

$$\alpha_{soft\,\min} > \frac{R_r}{L_r} \tag{113}$$

The selection of the actual value for α_{soft} can be done exactly as presented in (79).

5.4 Practical implementation of DFIG soft synchronization

In this section, a step by step procedure is established for DFIG soft synchronization. In addition, some relevant practical implementation issues are also discussed here.

5.4.1 Incremental Encoder angle offset on rotor alignment

Reflecting on **Error! Reference source not found.**, the rotor electrical angle measurement is fundamental in enabling rotor current control for both normal and soft synchronization conditions. The rotor angle can be obtained by using an incremental encoder coupled with the machine shaft. This type of encoder only measures the relative position of the rotor with respect to an initial resting angle $\theta_r^{initial}$. If the rotor is not initially aligned to the stator stationary axis (i.e. $\theta_r^{initial} \neq 0$), then the measured rotor angle θ_r will introduce an offset in θ_{slip} used in the rotor current synchronous transformation. This offset in θ_{slip} results in a phase shift between the induced stator voltage and grid voltage prior to synchronization. In [30], a separate PLL is proposed for computing the stator voltage angle which converges to the grid angle. A simpler method is proposed in [65], where $\theta_r^{initial}$ is first approximated then added to θ_{slip}. This approximation is given by:

$$\theta_r^{initial} = \theta_g - 90^o - \theta_{slip} \tag{114}$$

The grid voltage angle θ_g is computed by the grid-side PLL and θ_{slip} can be calculated from the stationary rotor current components. The relationship in (114) can also be observed in Figure 5-1, where rotor currents in the synchronous frame should be in quadrature with the grid voltage component if $\theta_r^{initial} = 0$.

5.4.2 Controller gain interchange between normal and synchronizing operations

As mentioned previously, the changing rotor dynamics require changing controller gains, as well as feedforward compensation terms. So, it is important to consider that the transition between controller structures depicted in Figure 5-2 and Figure 5-3 should occur in a seamless manner. To be precise, from the point of closing the grid contactors, the control voltages V_{rd} and V_{rq} should be forced to remain the same for a period that is equal to the contactor mechanical closing time. After the contactor has closed, the controller structure will transition to normal operational mode where the procedure will ensure that no large variations occurs in the rotor control voltages due to changes in the rotor controller gains. This operation can be described by the following expression:

$$V_{rdq}(k) = V_{rdq}(k-n) \tag{115}$$

The discrete variable k represents the current sampling instance and n is a integer increment that resets to zero if the following condition is met:

$$nT_{samp} = T_{mech} \tag{116}$$

T_{samp} and T_{mech} in (116) represents the rotor current control sampling period and grid contactor mechanical closing period respectively.

5.4.3 Soft synchronisation task sequence

Based on all aspects discussed in this chapter, a flow chart is provided in Figure 5-4 which details all of the steps that must be taken leading up to the point of DFIG grid synchronization.

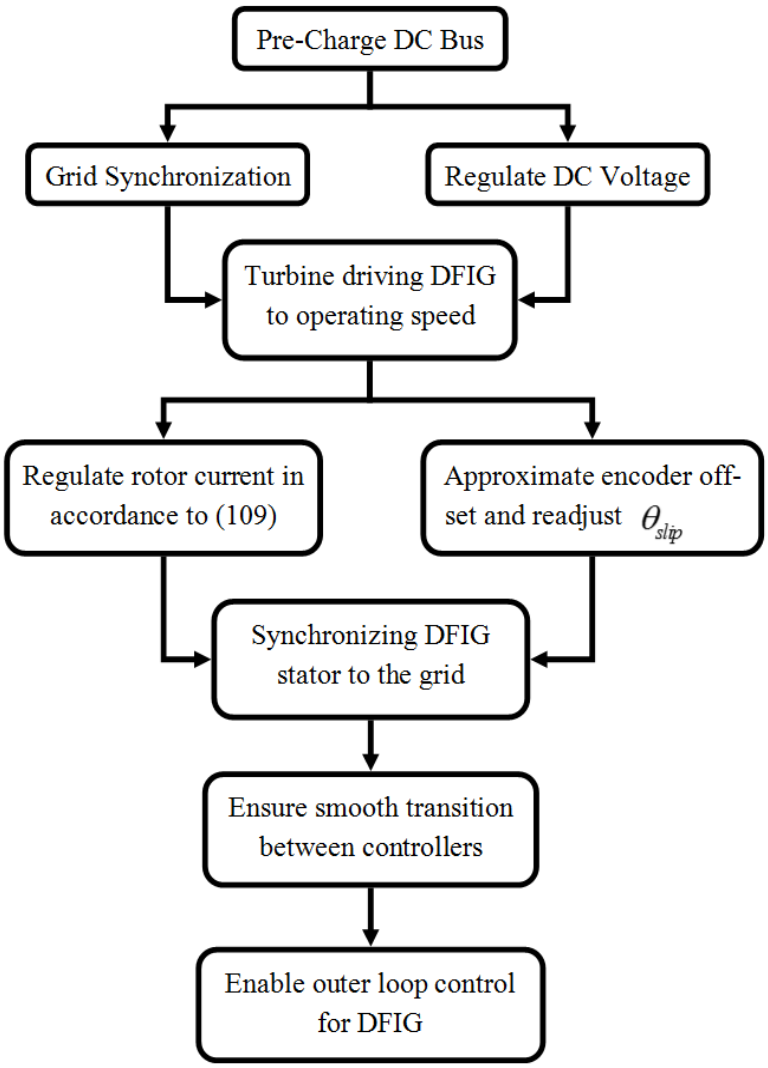

Figure 5-4: DFIG soft synchronisation procedure

It should be noted the procedure presented above includes initial GSC operations which was not discussed in this chapter.

6. DFIG Simulations

The system models and concepts presented previously were simulated prior to the laboratory implementation, where results gathered are shown in this chapter. This is a necessary process for ensuring a good understanding with respect to all underlying principles, and that the laboratory implementation of the DFIG system can be safely implemented. The simulation results also serve as a mean of validating the final experimental results.

All simulations were performed in MATLAB/Simulink. In order to facilitate a simulated environment that closely resembles the physical system, model variables were directly derived from actual hardware parameters. These parameters were either extracted from supplier data sheets or determined experimentally. System parameter identification is detailed in chapter 7. For the purpose of coherent reporting, several key factors for the system under investigation are listed below:

- The DFIG is a 4-pole wound rotor induction machine, rated at $2.2kW$. Its stator voltage is rated at $380V_{rms}^{l-l}$.
- All model parameters can be found in chapter 7. The simulated controller responses are aimed to have close resemblance with final laboratory system performance.
- System dynamics are simulated to achieve correct operation within the generator control level. Refer to chapter 2 for a comprehensive overview on turbine MPPT operations.

Practical controller implementation issues are presented first, then the simulated RSC and GSC controller responses are presented next. Converter SVPWM algorithms for both two- and three-level VSC's are tested in simulation, with specific emphasis on the latter topology. Finally, complete system operations were simulated with DFIG soft synchronisation incorporated in the overall procedure.

6.1 Practical controller implementation issues

This section expands on the concepts presented in sections 3.3 to 3.6, where practical implementation issues for the vector controller are studied in simulation.

6.1.1 Integrator anti-windup

Based on section 3.3, the PI controller structures with and without anti-windup is shown in Figure 6-1.

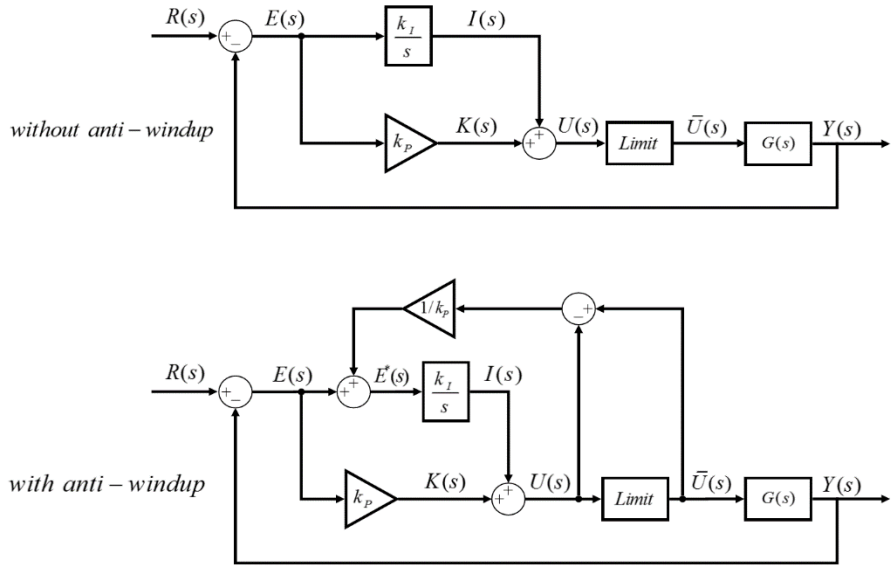

Figure 6-1: PI controllers with and without anti-windup

The implementation of anti-windup is based on the back-calculation principle. The output response for both controller structures were simulated. Results for $Y(s)$ and $U(s)$ dynamics are shown in Figure 6-2.

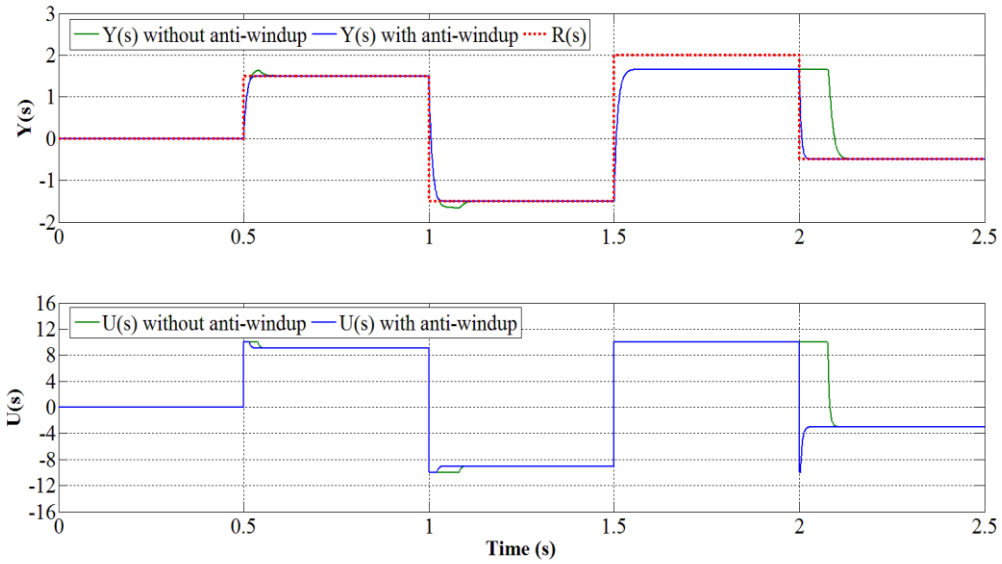

Figure 6-2: Effect of anti-windup on controller output

The controller transient specifications are of minor importance here. The demonstration here shows the impact caused by anti-windup. The controller saturation limit was set to $\bar{U}(s) = \pm 10$ in this case. It is clear from Figure 6-2 that when $U(s)$ was saturated, overshoots could be observed in $Y(s)$ from the controller without anti-windup. The worst case scenario was simulated at $t = 1.5s$, where $U(s)$ was saturated for an extended amount of time. It could be observed that $Y(s)$ without anti-windup did not follow the reference immediately at $t = 2s$, where the system attempted returning to normal operating conditions. This is caused by the integrator accumulating all the error during $U(s)$ saturated period. Therefore, integrator anti-windup must be employed to prevent poor controller transients and potential system instability.

6.1.2 Integrator discretization

The controller discretization discussed in section 3.4 is presented here. In particular, the integrator term $\frac{k_I}{s}$ in Figure 6-2 can be implemented digitally as shown in Figure 6-3.

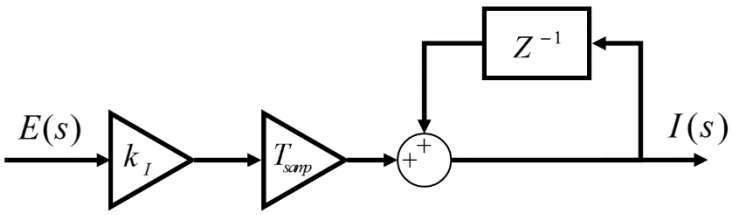

Figure 6-3: Digital implementation for the integrator

The term Z^{-1} represents a unit shift operation in memory. The integrator input must be multiplied by the corresponding controller sampling period T_{samp}. A generic PI controller was discretised and

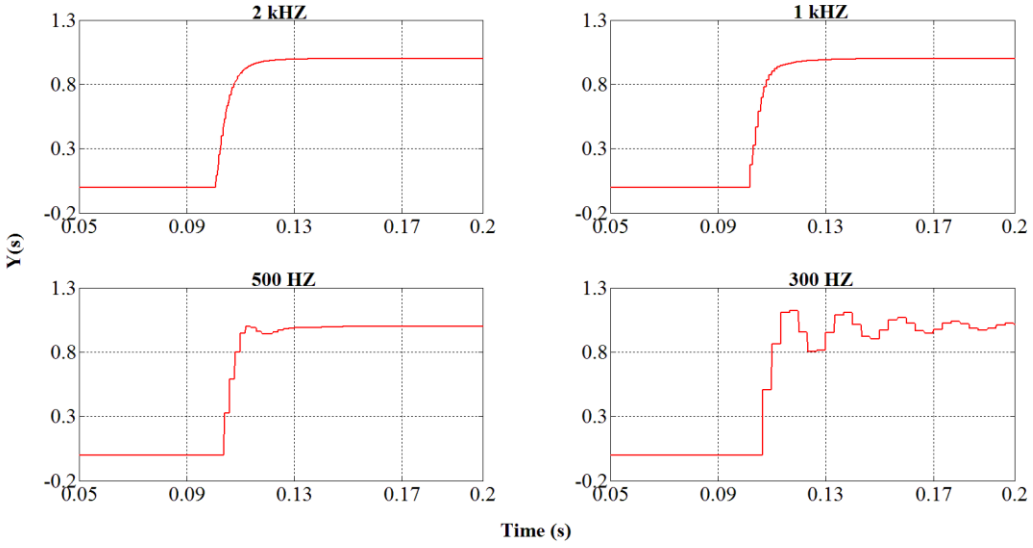

Figure 6-4: Output response from discretised controller with different sampling frequencies

simulated using the above method. The closed loop system was a first order system with a bandwidth of $200Hz$. Simulations were performed to generate a closed loop step response, based on the continuous domain controller design, for various sampling frequencies. Results shown in Figure 6-4 illustrates that as the sampling frequency was decreased to $300Hz$, close to the closed loop bandwidth, the transient response deteriorated. This is expected since the controller sampling delay became large enough to affect system dynamics. Therefore, sampling frequency for the controller should be chosen at least ten times larger than the designed bandwidth which allows continuous domain control design to hold even for digital systems.

6.1.3 Command voltage limiting

As mentioned previously in section 3.5, saturation limits for the inner current control loop cannot be performed on the numerical values of the individual dq components, where the modulus should be limited instead.

To simulate command voltage limiting, equations (61) and (62) were used. Corresponding dq and $\alpha\beta$ components for the limited and actual reference voltage $\overset{1}{V}_{ref}$ are shown in Figure 6-5.

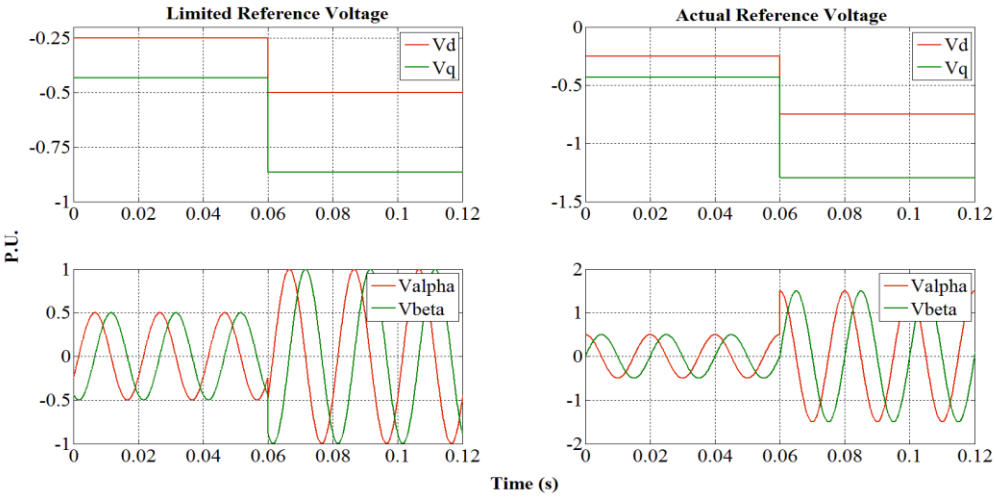

Figure 6-5: Reference voltage saturation

The purpose of limiting the reference voltage is to keep converter modulation within the linear range, therefore results shown here are in per unit for a more intuitive analysis. At $t = 0.06s$ the reference voltage was commanded to exceed the saturation limit. Both d and q components of the limited $\overset{1}{V}_{ref}$ deviated from the actual reference values. In fact, the limited $\overset{1}{V}_{ref}$ in the stationary reference frame has amplitudes of one for its $\alpha\beta$ components. This can be visualised by plotting the $\alpha\beta$ values in Figure 6-5 with respect to their own axis as shown in Figure 6-6.

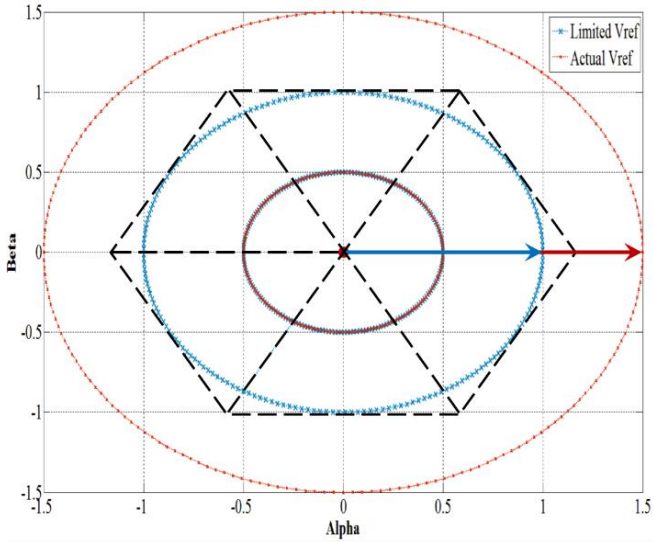

Figure 6-6: XY plot for command voltage limiting operation

With the SV diagram of a two-level VSC superimposed on top, it is easy to see that the limited $\vec{V}_{ref}$ always remain in the hexagon, which corresponds to a unity modulation index.

6.2 PLL operation

The main purpose for the PLL discussed in section 3.6 is to obtain the grid angle. The parameters for the PLL PI compensator were obtained using (35) and (64). Since the grid voltage operates at $50\,Hz$, the closed loop settling time was set to be $t_s = 0.02s$. The damping ratio was set to $\zeta = \frac{1}{\sqrt{2}}$ for a critically damped system. The values for PLL PI gains were then computed as $k_P = 212.93$ and $k_I = 2267$. The simulated results for the PLL operation are shown in Figure 6-7.

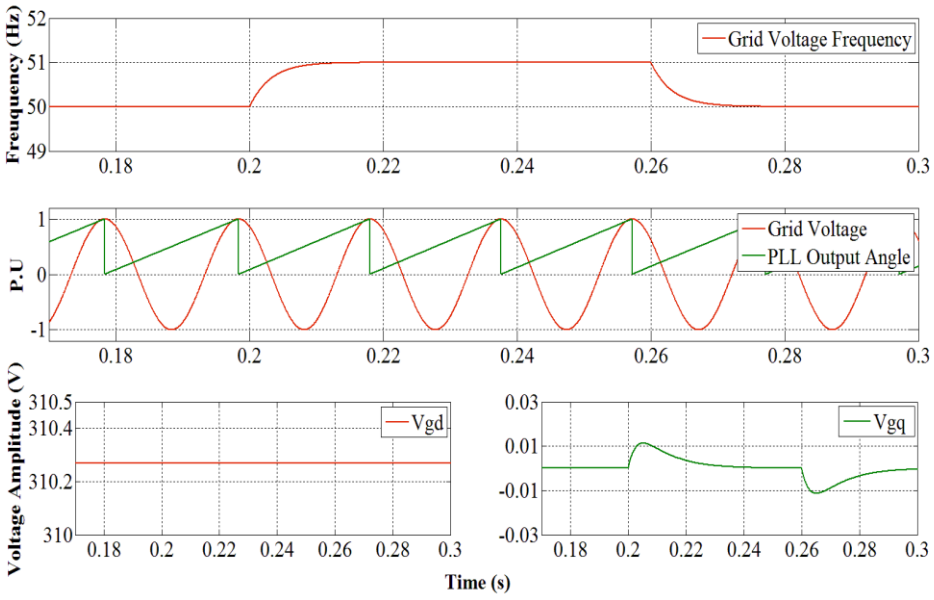

Figure 6-7: Simulated PLL operations

The grid voltage was set to $380V_{rms}^{l-l}$ with a fundamental frequency of $50Hz$. To prove the reliability of the PLL, a grid voltage frequency jump of $1Hz$ was simulated between $t = 0.2s$ and $t = 0.26s$. The designed PLL produced output angles that were synchronised to the grid voltage, even during frequency jumps. The PLL output angle were then used to transform the grid voltage to the synchronous frame, which resulted in the constant waveform of V_{gd}.

It should be noted that it is easy to simulate frequency changes in the grid voltage. In reality, a rigid grid voltage would have little variations in amplitude, frequency and phase. Therefore, the simulated PLL shows promising results for the experimental implementation.

6.3 RSC controller responses

The RSC controller responses were simulated based on the IMC design presented in section 3.8. In particular, attention was paid to the RSC closed loop transient response and system stability. The PI compensator gains were calculated using physical system parameters detailed in chapter 7. In addition, the effect of active damping is presented here with respect to RSC current control.

6.3.1 Normal rotor current control

It was found that the wound rotor induction machine in the laboratory has parameters that results in a process bandwidth of $\frac{R_r}{L_\sigma} = 109.56$. According to (78) the closed loop bandwidth for normal rotor current control must be greater than the process bandwidth, therefore α_r was chosen to be twice as fast resulting in $\alpha_r = 220$. The corresponding settling time, according to (79), for the normal rotor current step response is $t_s = 0.019s$. The control sampling frequency was chosen to be ten times faster than the closed loop bandwidth, which resulted in a sampling period of $T_{samp} = 0.5ms$.

It should be noted that theoretically α_r can be set as fast as one would desire. However, a large closed loop bandwidth may impose unrealistic requirements for the controller sampling frequency. In addition, the system can become more prone to noise. Therefore, closed loop bandwidth should be set considering physical limitations of the controller hardware.

The discretised PI gains and active damping term for the normal rotor current controller were calculated using (77), which resulted in the following values:

$$\begin{aligned} R_a &= 5.55 \\ k_P &= 11.58 \\ k_I T_{samp} &= 1.2185 \end{aligned} \tag{117}$$

The normal rotor current controller step response and its corresponding open loop frequency response are shown in Figure 6-8.

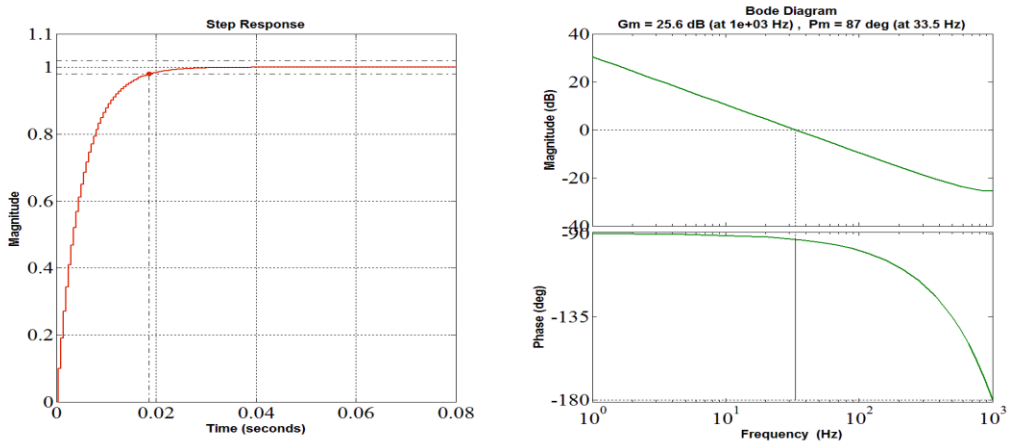

Figure 6-8: DFIG normal rotor current controller responses

The step response shows expected behaviour with respect to the designed settling time of $t_s = 0.019s$. The frequency response has a gain margin of $25.6\,dB$ and phase margin of 87^o which indicates that the closed loop system will be stable. In addition, its margin of stability is within acceptable range to cater for model errors or parameter variations.

To demonstrate the effect of active damping, controller responses for both standard IMC, and IMC with active damping are compared. In particular, step disturbance rejection of the closed loop system was simulated for varying settling times. The results are shown in Figure 6-9 below.

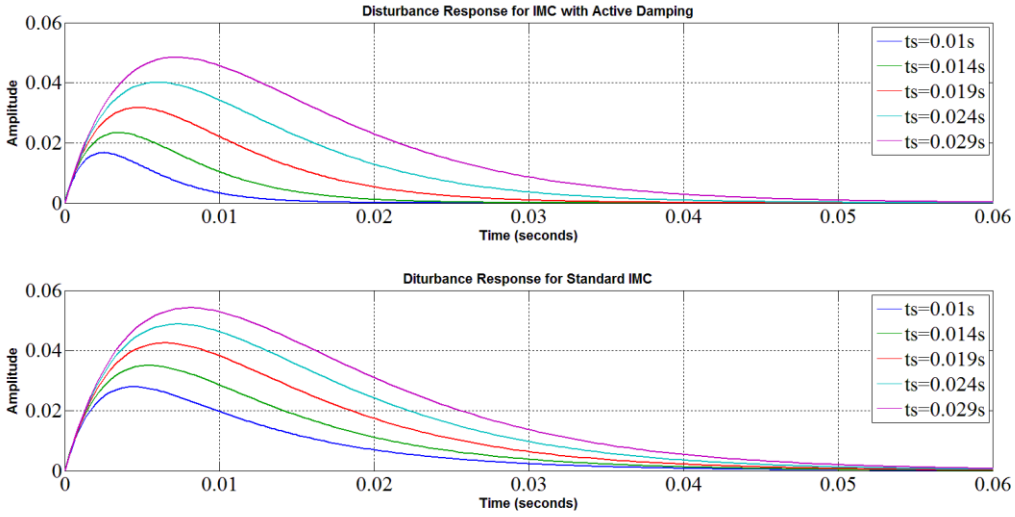

Figure 6-9: Disturbance rejection for standard IMC and IMC with active damping

The results shows that in the case where active damping was employed, disturbances had lower magnitudes and were damped out faster.

The analysis on active damping was presented to demonstrate its impact on closed loop system performance. Since all controller designs in this dissertation will adopt the use of active damping, no further simulations related to this aspect will be performed henceforth.

6.3.2 Synchronisation rotor current control

When the DFIG stator is open, the machine process bandwidth is $\frac{R_r}{L_r} = 12.53$. Since the bandwidth of the DFIG rotor circuit is much smaller prior to grid connection, therefore a more conservative transient response requirement must be imposed for the synchronisation controller. The closed loop bandwidth was chosen to be $\alpha_{soft} = 22.22$ with a corresponding settling time of $t_s = 0.18s$ for the synchronisation current step response. The same sampling frequency for the normal rotor current control can be equally applied to the synchronisation controller.

The discretised PI gains and active damping term for the synchronisation rotor current controller were calculated using (112), which resulted in the following values:

$$\begin{aligned} R_{soft} &= 4.66 \\ k_P &= 10.69 \\ k_I T_{samp} &= 0.1187 \end{aligned} \tag{118}$$

The simulated synchronisation rotor current controller step response and its corresponding open loop frequency response are shown in Figure 6-10.

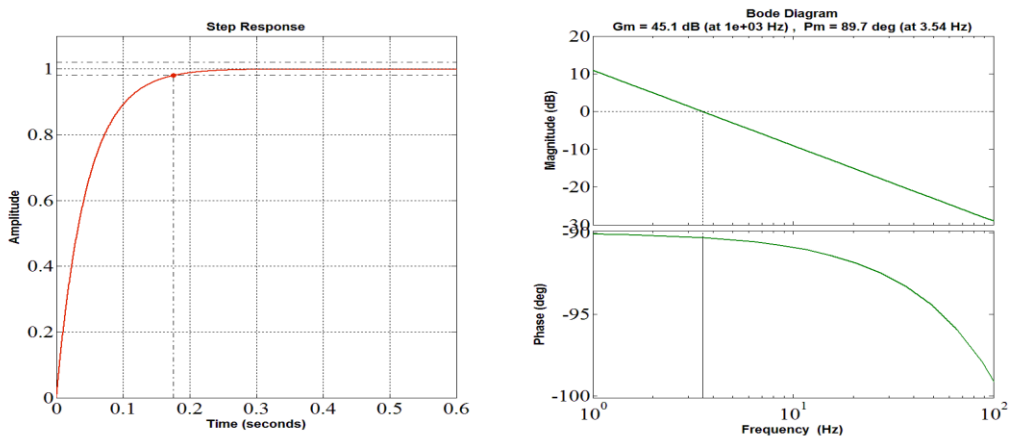

Figure 6-10: DFIG synchronisation rotor current controller responses

The step response shows expected behaviour with respect to the designed settling time of $t_s = 0.18s$. The frequency response has a gain margin of $45.1dB$ and phase margin of 89.7^o. The synchronisation rotor current controller can be seen to have better stability margins when compared to the normal rotor current controller, this is due to rotor circuit dynamics being slower when the stator is open.

6.3.3 Speed control

The speed control closed loop bandwidth was set to $\alpha_\omega = 3.51$ with a corresponding settling time for the speed step response of $t_s = 1.14s$. This bandwidth is sixty times slower than that of the normal rotor current control, therefore ensuring slower dynamics in the outer control loop. In addition, a slower speed control response may reduce excessive mechanical stress on the DFIG shaft during wind turbulent periods.

The control sampling frequency was chosen to be $T_{samp} = 5ms$ which is much faster than the closed loop bandwidth. The discretised PI gains and active damping term for the speed controller were calculated using (82), which resulted in the following values:

$$\begin{aligned} B_a &= 0.3687 \\ k_P &= 0.3687 \\ k_I T_{samp} &= 0.0065 \end{aligned} \tag{119}$$

The simulated speed controller step response and its corresponding open loop frequency response are shown in Figure 6-11.

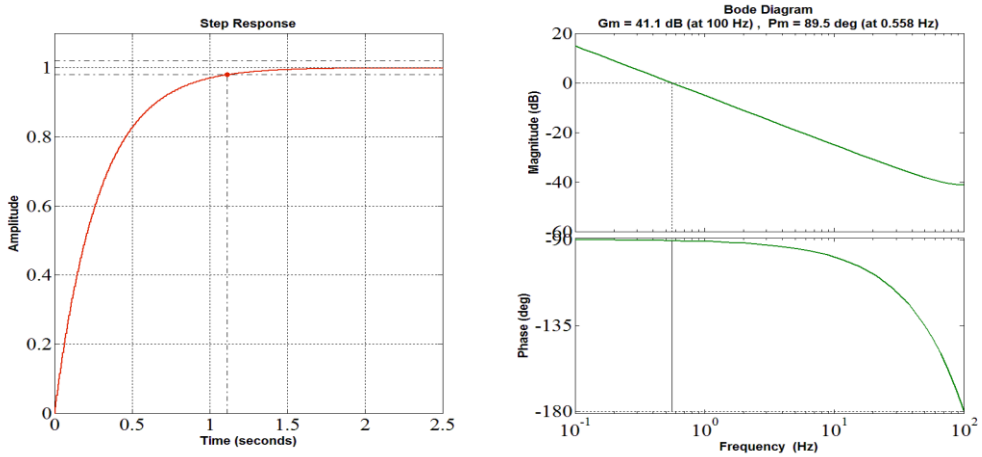

Figure 6-11: DFIG speed controller responses

The step response shows expected behaviour with respect to the designed settling time of $t_s = 1.14s$. The frequency response has a gain margin of $41.1dB$ and phase margin of 89.5^o which indicates that the closed loop system will be stable. In addition, its margin of stability is within acceptable range to cater for model errors or parameter variations.

6.4 GSC controller responses

The GSC controller responses were simulated based on the IMC design presented in section 3.9. In particular, attention was paid to the GSC closed loop transient response and system stability. The PI compensator gains were calculated using physical parameters detailed in chapter 7.

6.4.1 Grid current control

The grid filter has a process bandwidth of $\frac{R_g}{L_g} = 15.96$. According to (89) the closed loop bandwidth for grid current control must be greater than the process bandwidth, therefore α_g was chosen to be twelve times as fast resulting in $\alpha_g = 200$. The corresponding settling time for grid current step response is $t_s = 0.02s$. The control sampling frequency was chosen to be ten times faster than the closed loop bandwidth, which resulted in a sampling period of $T_{samp} = 0.5ms$.

The discretised PI gains and active damping term for the grid current controller were calculated using (88), which resulted in the following values:

$$R_c = 8.65$$
$$k_P = 9.4 \qquad (120)$$
$$k_I T_{samp} = 0.94$$

The grid current controller step response and its corresponding open loop frequency response are shown in Figure 6-12.

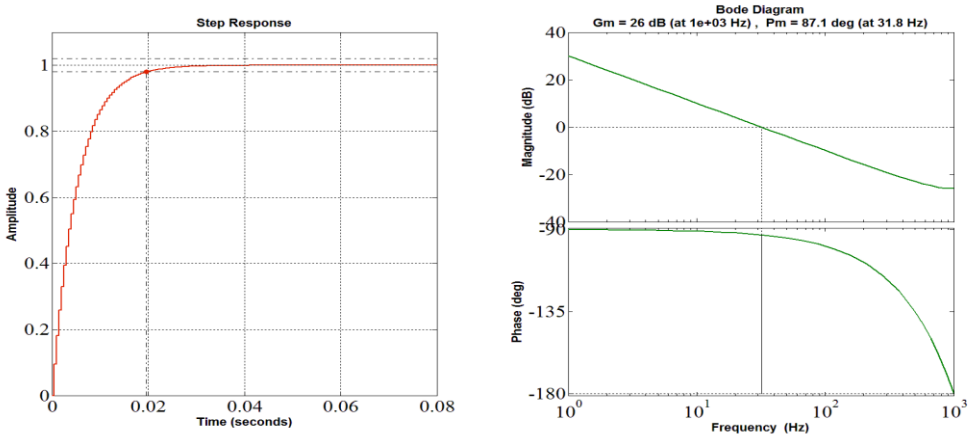

Figure 6-12: Grid current controller responses

The filter inductance is actually too big for the converter switching frequency, which in turn led to slow grid-side electrical dynamics. This is a limitation in this dissertation where existing lab equipment were used instead of procuring optimised components, however, the control design process would be exactly the same. The GSC control responses must be faster than that of the RSC control, therefore power

variation from the DFIG side can be promptly regulated by the GSC. This is why the closed loop bandwidth in this case was set to be much faster than the process bandwidth.

From the results shown in Figure 6-12, the step response shows expected behaviour with respect to the designed settling time of $t_s = 0.02s$. The frequency response has a gain margin of $26\,dB$ and phase margin of 87.1^o which indicates that the closed loop system will be stable. In addition, its margin of stability is within acceptable range to cater for model errors or parameter variations.

6.4.2 DC-link voltage control

The DC-link voltage control closed loop bandwidth was set to $\alpha_{dc} = 6.67$ with a corresponding settling time of $t_s = 0.6s$. This bandwidth is thirty times slower than that of the grid current controller, therefore ensuring slower dynamics in the outer control loop.

The control sampling frequency was chosen to be $T_{samp} = 5\,ms$ which is thirty times faster than the closed loop bandwidth. The discretised PI gains and active damping term were calculated using (94), which resulted in the following values:

$$G_a = 4.18\times10^{-4}$$

$$k_P = 4.18\times10^{-4} \qquad (121)$$

$$k_I T_{samp} = 1.39\times10^{-5}$$

The simulated DC-link voltage controller step response and its corresponding open loop frequency response are shown in

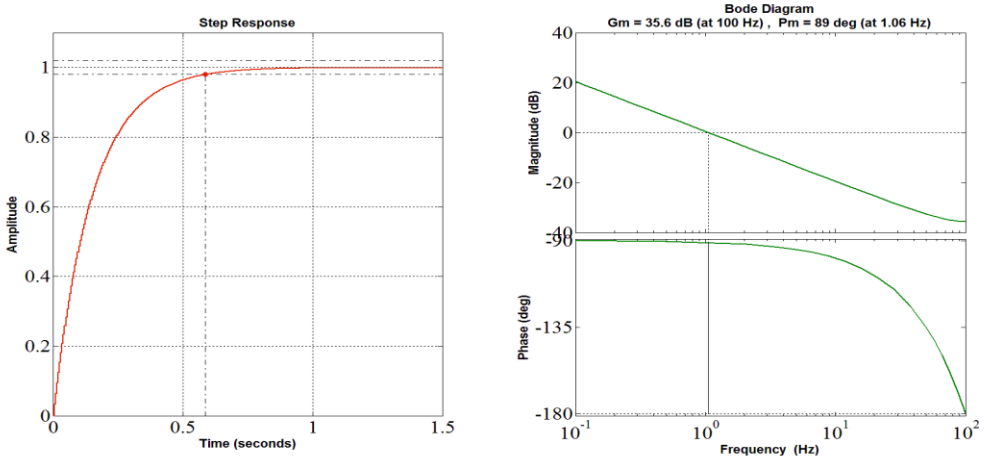

Figure 6-13: DC-link voltage controller responses

The step response shows expected behaviour with respect to the designed settling time of $t_s = 0.6s$. The frequency response has a gain margin of $35.6\,dB$ and phase margin of 89^o which indicates that the

closed loop system will be stable. In addition, its margin of stability is within acceptable range to cater for modelling errors or parameter variations.

6.5 Converter operations

Both two-level and three-level VSC operations were simulated using the SVPWM algorithms discussed in chapter 4. The focus is on the three-level VSC, where detailed simulations were performed with respect to the concepts presented in section 4.4.

6.5.1 Two-level VSC operations

The two-level SVPWM algorithm was developed in MATLAB where its implementation was tested using the two-level VSC model in Simulink. Simulation results of the two-level VSC output are shown in Figure 6-14.

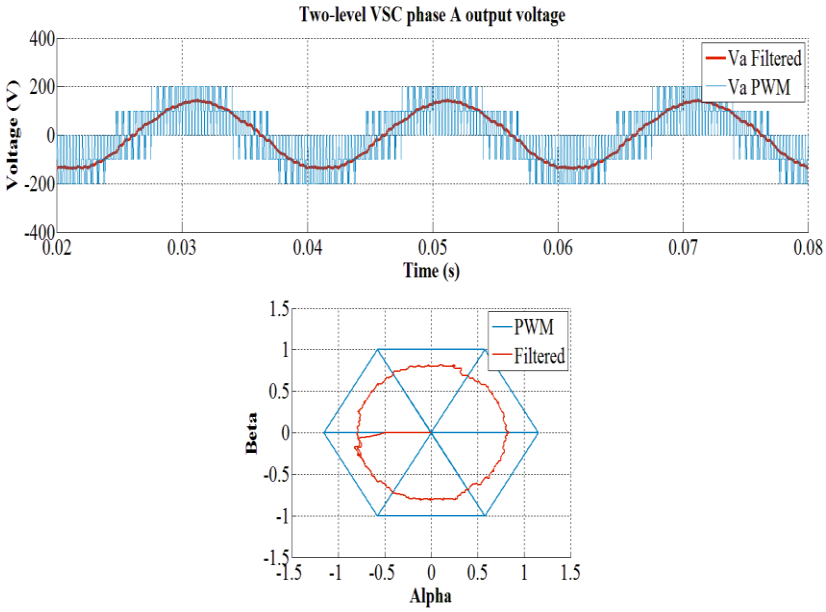

Figure 6-14: Two-level VSC phase output

For ease of presentation, only the phase-A output voltage of the two-level VSC is shown where both the PWM and the fundamental waveforms are included. The DC-bus voltage was set to $300V$ where the open loop output modulation index was set to 0.8. Modulation frequency for the VSC was set to $2kHz$. The time domain voltages were normalised and transformed to the $\alpha\beta$ reference frame, where the PWM voltage formed a hexagon that encloses the fundamental circle. Results shown in Figure 6-14 also validates the commanded modulation index as the fundamental voltage circle has a diameter of 0.8. Furthermore, an FFT analysis was performed on the VSC output voltage where results are shown in Figure 6-15.

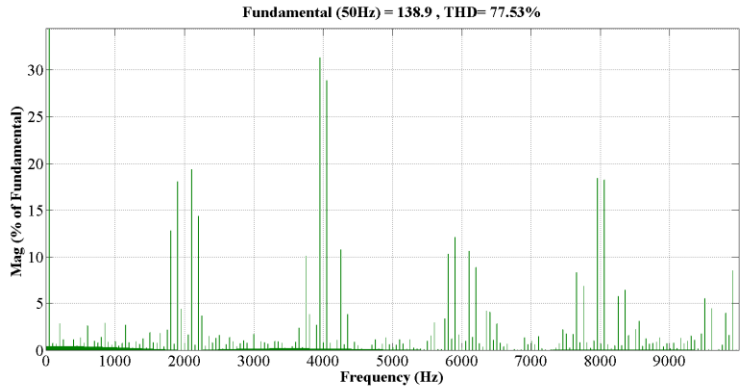

Figure 6-15: FFT analysis on two-level VSC output voltage

The FFT spectrum of the two-level output voltage validates the commanded switching frequency (i.e. 2 kHz) because all of the harmonics are centred on integer multiples of the switching frequency.

The results shown in this subsection indicates that the two-level SVPWM algorithm developed is appropriate.

6.5.2 Three-level VSC operations

The three-level SVPWM algorithm was simulated according to its procedural structure shown in Figure 4-13, where vital computation steps were investigated in detail to ensure the correctness of the algorithm.

Firstly the $dq - gh$ transformation presented in (106) was simulated and the results are shown in Figure 6-16.

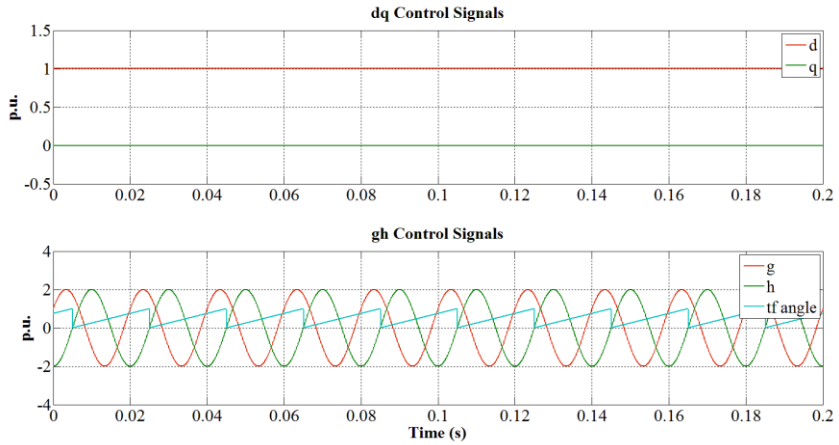

Figure 6-16: $dq - gh$ **transformation**

The dq control signals are given in per unit where the q-axis value was kept at 0, therefore the d-axis signal in this case represents the modulation index. Since the entire three-level SVPWM algorithm operates in a 2 per unit system, therefore the corresponding gh components have amplitudes of 2. The

transformation angle has the same zero crossings as the h-axis component, because $\vec{V}_{ref}$ is aligned with the g-axis whenever the transformation angle completes a period.

The selection of sectors and regions were simulated using logic expressions shown in Table 4-1 and Table 4-3. The results, based on a modulation index of 0.8, are shown in Figure 6-17.

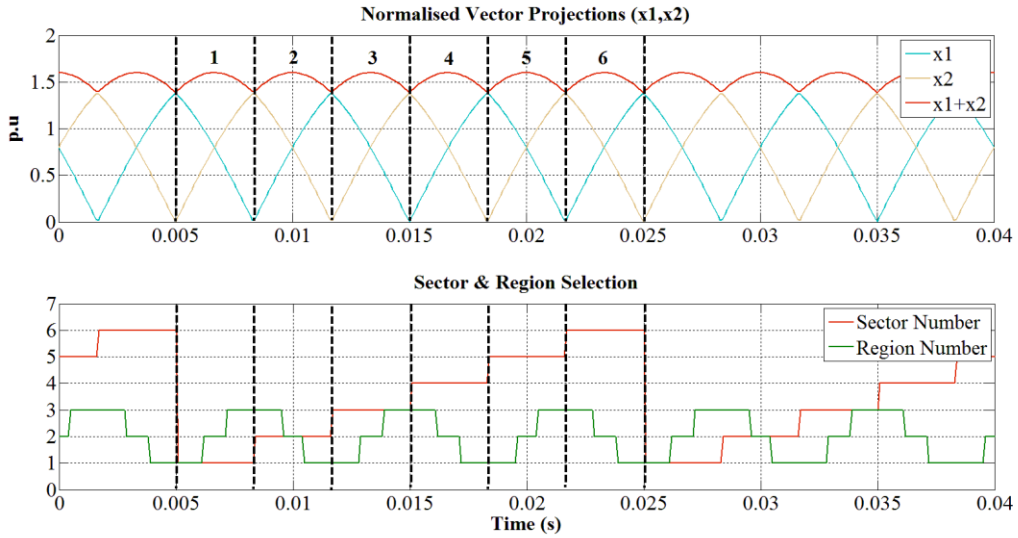

Figure 6-17: Sector and region selection based on equivalent x_1 & x_2

All of the modulation were performed in the first sector, therefore vector projection values x_1 and x_2 are shown to be inverted every time $\vec{V}_{ref}$ changes sector position. This property can be observed in the region selection as well. The peak values of x_1 and x_2 are shown to be 1.4, which reflects a modulation index of 0.8 in a 2 per unit system. Furthermore, the sum of x_1 and x_2 is always below 2, therefore the converter modulation is always linear. Finally, the duty cycles for the three-level NTV's can be directly calculated from x_1 and x_2 using the expressions shown in Table 4-1.

The implementation for the three-level SVPWM algorithm was simulated using the three-level VSC model in Simulink, and results with respect to the three-level VSC output are shown in Figure 6-18.

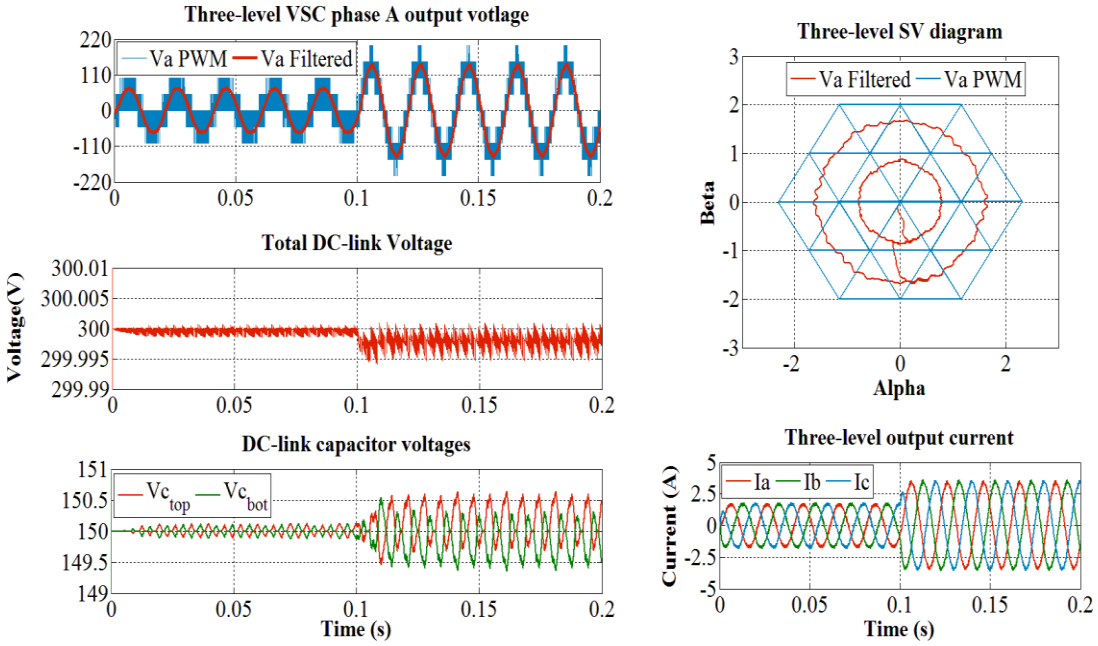

Figure 6-18: Three-level VSC operations

The phase-A output voltage is shown with its fundamental waveform superimposed. The DC-link voltage and modulation frequency were set to $300V$ and $2kHz$ respectively. The modulation index was first set to 0.4, and then stepped up to 0.8 at $t = 0.1s$. It is interesting to see that for smaller modulation indices, the output voltage exhibits the same form as in the case of a two-level VSC which can be explained using the 2 per unit SV diagram. For a reference voltage operating below 0.5 modulation index its $\alpha\beta$ components form a circle that is enclosed in the inner hexagon, therefore the NTV's used to approximate $\vec{V}_{ref}$ consists of short vectors only. This means not all possible output states of the three-level VSC are utilized.

The DC-link neutral voltage balancing is only relevant when the VSC is connected to a load, therefore the output current waveform is shown in Figure 6-18. It can be observed that the DC-link neutral voltage is periodically balanced, which is achieved by the charging and discharging of DC-link capacitors using the short vector selection method discussed in subsection 4.4.4. In the case where the modulation index is large between $t = 0.1s$ and $t = 0.2s$, the capacitor voltages are shown to oscillate with higher amplitudes. This is caused by the load current increase, which in turn produces a larger DC-bus neutral current flow. It should be noted that the total DC-bus voltage is relatively unaffected by any imbalance between the top and bottom capacitors.

FFT analysis were performed on the three-level VSC output for both operating modulation indices of 0.4 and 0.8, where Results are shown Figure 6-19.

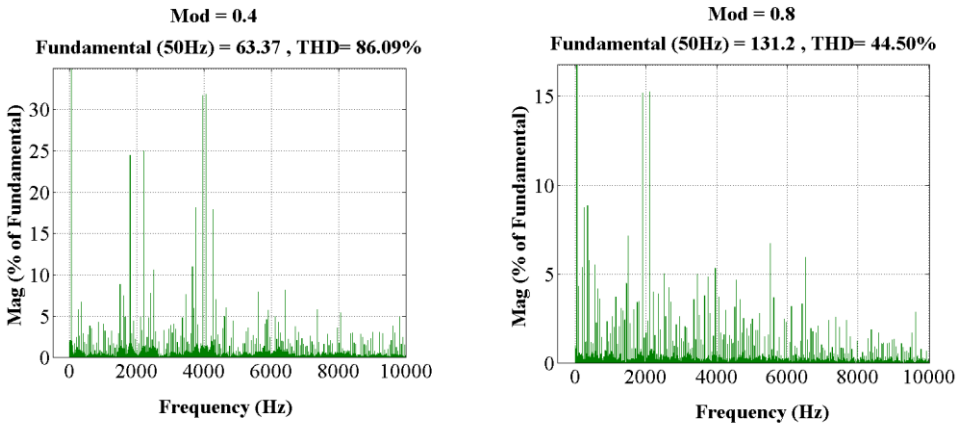

Figure 6-19: FFT analysis on three-level VSC output voltage

As discussed in chapter 4, the resulting switching frequency from the three-level SVPWM algorithm varies over time. This is evident in the above FFT spectrums where switching harmonics are scattered, especially for higher modulation indices. However, the dominant harmonics are still predominantly centered on multiples of the switching frequency. In the case of lower modulation indices, total harmonic distortion in the output voltage is higher. This is expected since less VSC output states are used, which means $\overset{1}{V}_{ref}$ approximation is comparatively less accurate.

The results shown in this subsection indicates that the three-level SVPWM algorithm developed is appropriate. However, operating modulation indices for the three-level VSC should be carefully considered for optimised performance.

6.6 DFIG soft synchronisation dynamics

Prior to DFIG power generation, the machine stator must be soft synchronised to the grid. The complete procedure was simulated based on principles presented in chapter 5, and results are shown in this section.

6.6.1 Complete synchronisation procedure

The DFIG soft synchronisation was simulated using the task sequence shown in Figure 5-4. The GSC was assumed to be synchronised to the grid and that the DC-link voltage was regulated. The rotor current controllers simulated in subsection 6.3.2 were implemented with the DFIG soft synchronisation model developed in Simulink. Results are shown in Figure 6-20.

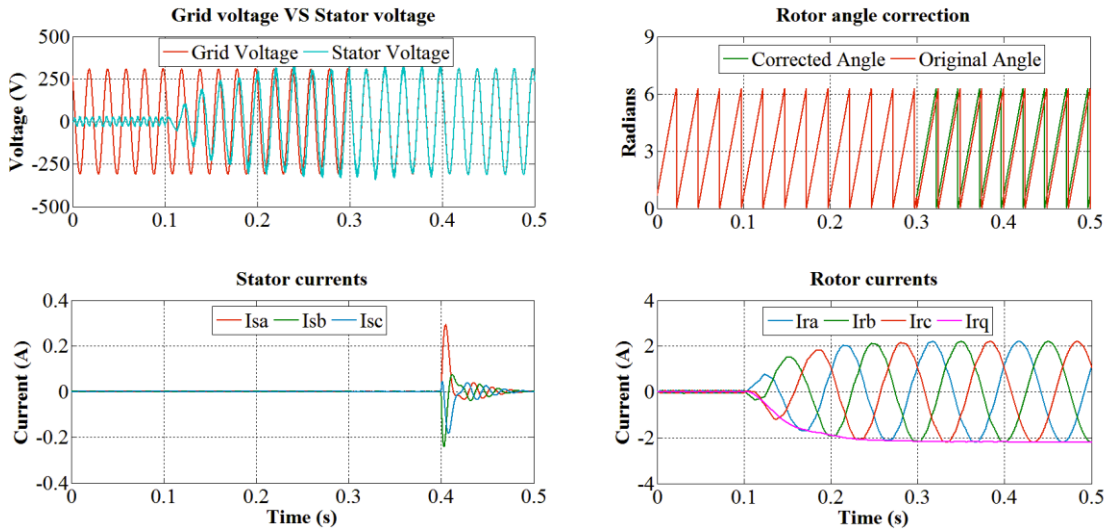

Figure 6-20: Simulated DFIG soft synchronisation

The rotor q-axis current was stepped at $t = 0.1s$ according to (109). The corresponding transient response shows a settling time of $t_s = 0.18s$, which resembles the synchronisation rotor current controller step response shown in Figure 6-10. The induced stator voltage, after the transient period, is equal to the grid voltage in amplitude and frequency. However, due to initial rotor angle offset, the two voltage's phases are slightly mismatched. The rotor angle correction method presented in (114) was implemented at $t = 0.3s$, and the stator voltage is shown to completely synchronise with the grid voltage. The DFIG was connected to the grid at $t = 0.4s$ where the stator contactor was closed.

The rated current amplitude for the investigated machine is $5.65A$, where the peak amplitude of the stator current transient during synchronisation is $0.26A$ which is only 4.95% of the machine rating. It must be emphasised that the machine was initially forced to operate at a 20% slip in simulation. However, in practice the DFIG rotor should be first accelerated to its operating speed range by the wind turbine.

Once the DFIG is connected to the grid, the rotor current controller can be switched over to normal operation mode. The stator currents shown returns to zero after synchronisation, which implies that no active or reactive power exchange occurs between the DFIG and the grid.

6.6.2 Effect of feedforward error during DFIG soft synchronisation

To demonstrate the effect of feedforward error on DFIG soft synchronisation discussed in section 5.2, the simulation model was implemented again with an artificial feedforward error set for the rotor current controller. Results obtained are shown in Figure 6-21.

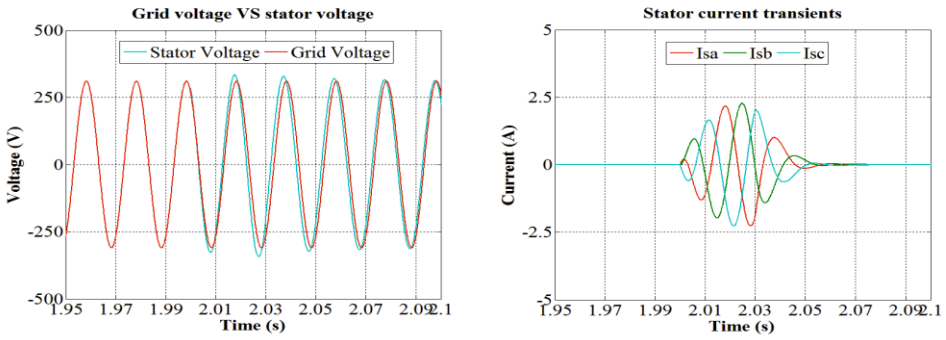

Figure 6-21: Effect of feedforward error during DFIG soft synchronisation

For the results shown above, the feedforward error was set to 30%. It can be seen that a feedforward error causes a phase shift between the induced stator voltage and the grid voltage, which in turn leads to stator current spikes during DFIG grid synchronisation. It should be noted that this phase shift can be simulated easily, however, due to grid voltage dominance it cannot be experimentally shown.

The stator contactor was closed at $t = 2s$ and the stator current transient, caused by feedforward error, can be observed to reach a peak amplitude of $2.28A$. The stator current is then quickly damped out by the controller effort, therefore feedforward error do not pose as a serious issue when the rotor current controller is in normal operation mode.

The same simulation was performed multiple times for varying feedforward error expressed as percentage deviation from the actual DFIG back-EMF. The resulting peak amplitudes of stator current transients are recoded in Table 6-1.

Table 6-1: Stator current peak amplitudes caused by varying feedforward error.

Feedforward Error (%)	Stator Current Amplitude (A)
5	0.81
10	0.96
15	1.14
20	1.51
25	1.89
30	2.28
35	2.65
40	3.05
45	3.5
50	3.79

The data above shows that increasing error in the feedforward compensation produces larger stator current transients during synchronisation, which could cause excessive stress on the DFIG circuits. These disturbances caused by feedforward error can be damped out faster by using active damping with the rotor current controller.

6.7 System dynamic simulations

Decoupled simulations for both GSC and RSC control were performed first to demonstrate their respective operating dynamics. Full system simulations were then performed for the complete DFIG wind turbine.

6.7.1 Independent GSC control dynamics

Inner current control for the GSC-side system was simulated first, and results for its various operating dynamics are shown in Figure 6-22.

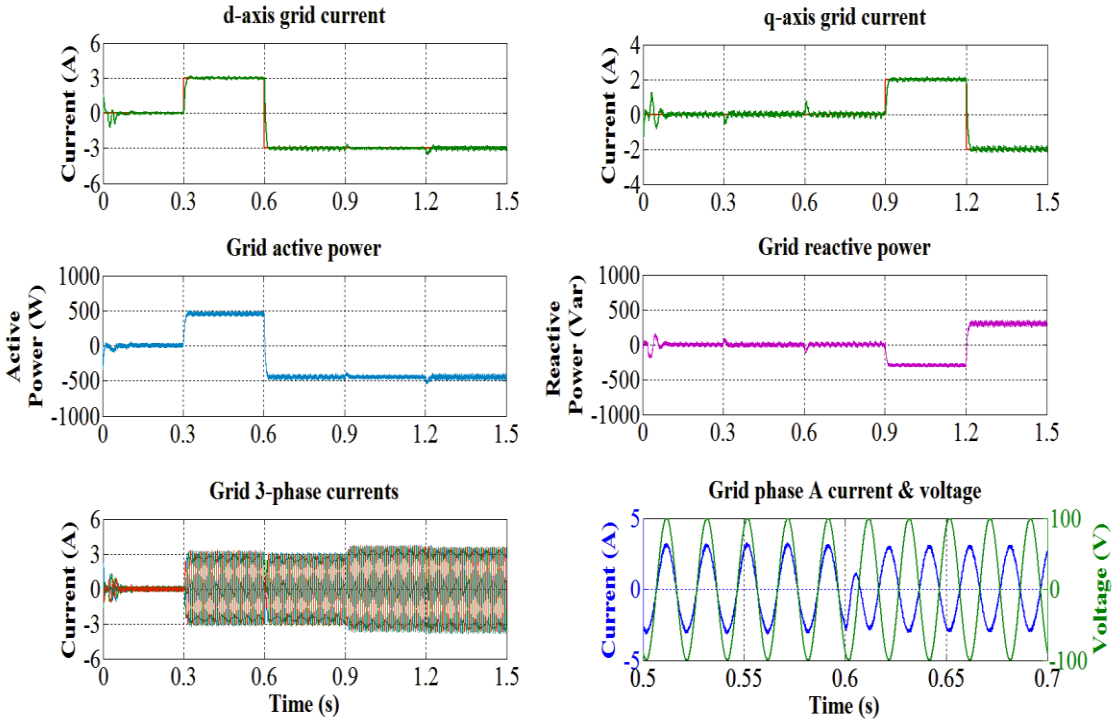

Figure 6-22: Grid current control dynamics

A constant DC-link voltage source was enforced for the independent GSC current control simulations. The d-axis current reference was stepped to $3A$ at $t = 0.3s$ and then $-3A$ at $t = 0.6s$. It can be seen that the actual d-axis current closely follows the reference and has response characteristics that resembles the grid current controller response presented in subsection 6.4.1. It should be noted that positive quantities shown in the above results represents a directional flow from converter to grid. The direction of the grid active power changes at $t = 0.6s$ due to the polarity change in the d-axis current, which can be further observed in the grid phase-A voltage and current waveforms. The 0^o and 180^o phase differences between the grid current and voltage indicates that unity power factor operation is enforced at all times. Finally the q-axis current was stepped to $2A$ at $t = 0.9s$ and $-2A$ at $t = 1.2s$, where the corresponding reactive power variations shows inverted characteristics to the q-axis current variations. The above results also shows that the grid active power is controlled by the d-axis current whereas reactive power is controlled by the q-axis current.

The DC-link voltage control was simulated with grid current control as the inner control loop, and corresponding dynamic results are shown in Figure 6-23.

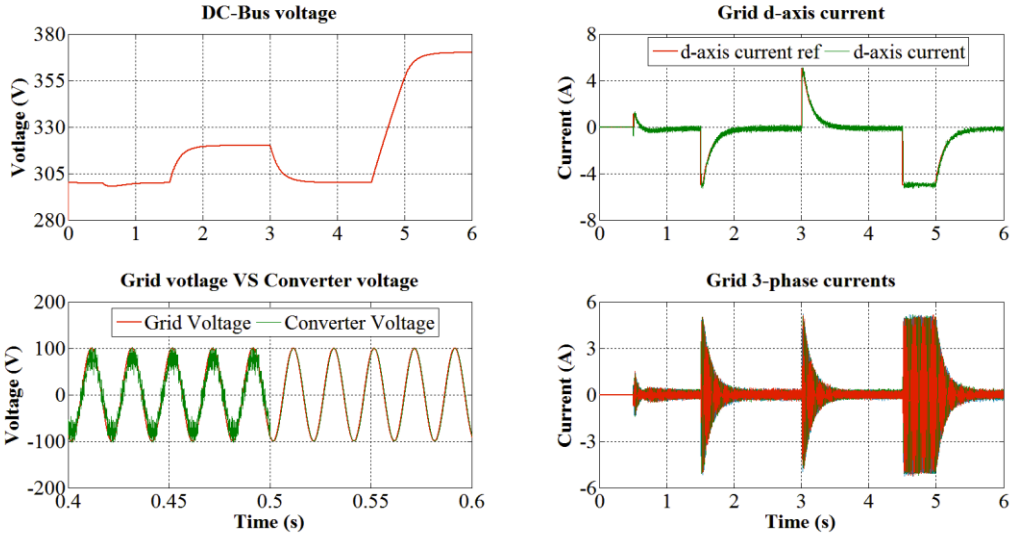

Figure 6-23: DC-link voltage control dynamics

The GSC grid synchronisation process is demonstrated in the above results for the period between $t = 0s$ and $t = 0.5s$. Reflecting on Figure 5-4, this procedure must be done prior to the DFIG soft synchronisation. The steps involved are listed below:

- DC-bus pre charge through single phase grid voltage via a series connected resistor.
- Enable GSC with grid contactor open.
- Ensure voltages at the converter output terminals are synchronised to the grid voltage.
- Close grid contactor.

The GSC synchronisation task is actually analogous to the DFIG soft synchronisation. However, due to its industry standard implementation therefore it was not extensively presented in this dissertation.

DC-link voltage control was simulated after GSC synchronisation, where the DC-link voltage was first stepped from $300V$ to $320V$ at $t = 1.5s$. The corresponding d-axis current reference produced by the outer control loop is shown on the right in Figure 6-23, where it can be seen that the grid d-axis current follows the reference almost instantaneously. The charging and discharging of the DC-bus require current to be drawn from or dissipated into the grid, which are illustrated by the grid d-axis current polarity changes.

Lastly a DC voltage step of $70V$ was simulated at $t = 4.5s$, where the corresponding DC-link voltage response is linear and did not reach steady state within the designed settling time of 0.6s. This is caused by a saturation limit of $5A$ being enforced on the d-axis reference current, which prevents the system from reaching overrated conditions.

For the independent DC-bus voltage control simulations it was assumed that no input power from the DFIG was present, therefore currents shown in Figure 6-23 always return to zero after the DC-bus voltage have reached steady state.

6.7.2 Independent DFIG control dynamics

Inner rotor current control for the RSC side system was simulated first, and d-axis current step responses are shown first in Figure 6-24 to justify some controller modifications.

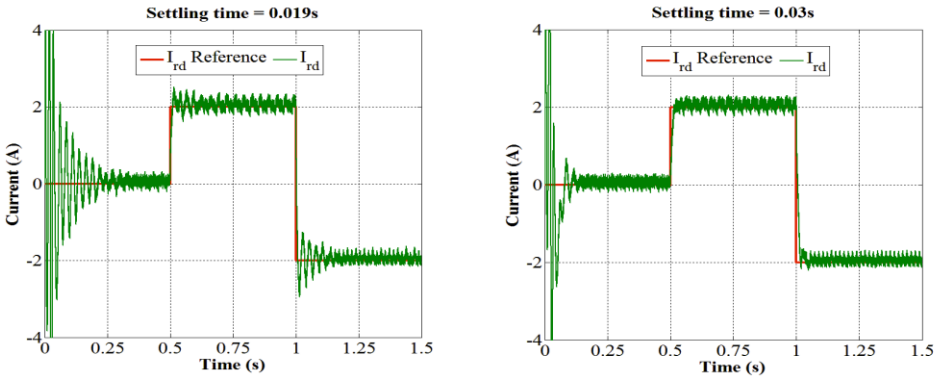

Figure 6-24: Rotor d-axis current step responses for different settling time

Rotor current step tests were performed on the asynchronous machine model in Simulink, where the controller presented in subsection 6.3.1 was used. Looking at the left hand side current step response where the original controller design with a settling time of $t_s = 0.019s$ was used, it can be observed that significant transient oscillations are present in the current response. These oscillations are caused by the derivative flux component $\frac{L_m}{L_s}\frac{d\left|\vec{\phi}_s\right|}{dt}$ in (66) which was neglected in the controller design. Although the assumption of constant stator flux holds true for machine steady state, however, during transient conditions the stator flux would vary. Therefore, the magnitude of the derivative flux term during transient operations becomes significantly higher for faster controller response times. In order to mitigate the current oscillations caused by stator flux dynamics, the control settling time was slowed down from the original design to $t_s = 0.03s$. The resulting closed loop bandwidth is still faster than the process bandwidth, and the discretized PI gains for the adjusted rotor current controller are given as:

$$\begin{aligned} R_a &= 1.3067 \\ k_P &= 7.3312 \\ k_I T_{samp} &= 0.4887 \end{aligned} \tag{122}$$

The d-axis current step response based on the adjusted controller design is shown on the right in Figure 6-24 where it can be observed that almost no transient oscillations are present.

Independent rotor current control was then simulated using the adjusted controller. These results are shown in Figure 6-25.

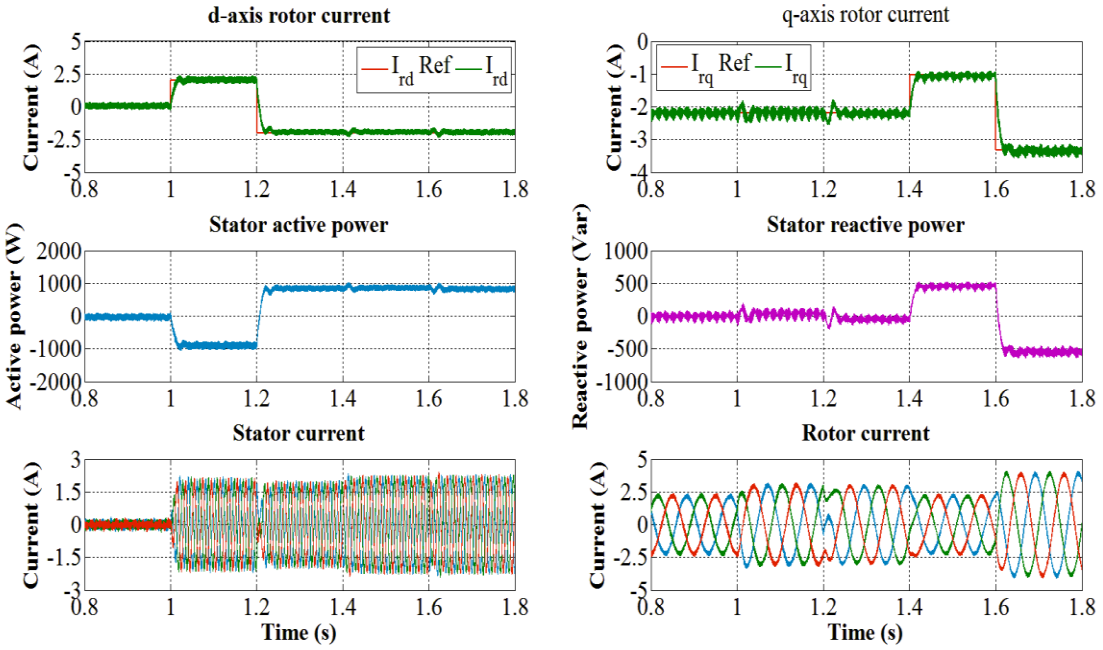

Figure 6-25: Rotor current control dynamics

It was assumed that the DFIG had been soft synchronised to the grid, and the machine initially operated at a constant 0.2 slip. The rotor d-axis current was stepped to $2A$ at $t=1s$ and $-2A$ at $t=1.2s$, where the stator active power is shown to have inversed variations when compared to the d-axis current. For the RSC control, negative power represents current flow from machine to grid. The rotor q-axis current was initially operating at $-2A$ due to the soft synchronisation requirement expressed in (109). In addition, the initial q-axis current value ensures that zero reactive power is exchanged between the stator and the grid. The rotor q-axis current was stepped to $-1A$ at $t=1.4s$ and $-3A$ at $t=1.6s$, where the stator reactive power is shown to vary accordingly. Therefore, it is evident from the above results that stator active and reactive power are independently controlled by rotor d-axis and q-axis currents respectively.

Lastly by comparing the stator and rotor three-phase currents shown at the bottom of Figure 6-25, it can be seen that the stator currents operate at a much higher frequency than the rotor currents. This is expected as the rotor electrical frequency depends on the machine slip, which is generally much slower than the stator electrical frequency.

The RSC speed control loop was simulated with rotor current control as the inner control loop, and corresponding dynamic results are shown in Figure 6-26.

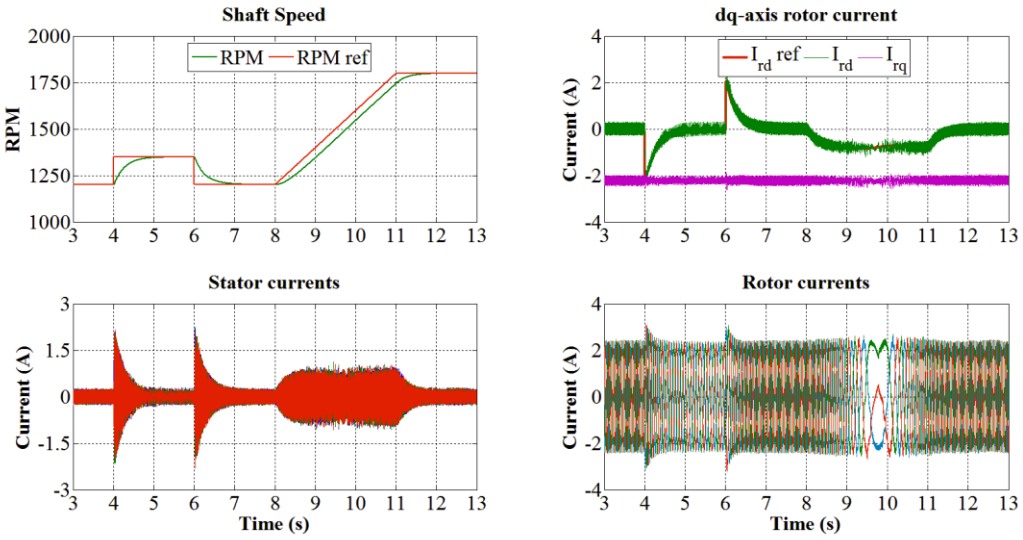

Figure 6-26: DFIG speed control dynamics

The machine was initially assumed to be in steady state, then the speed reference was stepped up by $150\,rpm$ at $t = 4s$ and returned to the original speed at $t = 6s$. The actual machine speed response time resembles the speed controller response simulated in subsection 6.3.3. The rotor d-axis current follows the references from the speed controller almost instantaneously, and corresponding stator current transients caused by rotor d-axis current variations can be observed.

It should be noted that input power to the machine was set to zero for the DFIG speed control simulations, therefore stator currents always return to zero after the speed have reached steady state.

Lastly a ramp speed reference was provided for the period between $t = 8s$ and $t = 11s$, which accelerated the machine from sub-synchronous speed to super-synchronous speed. Since rotor currents operate at the slip frequency of the machine, therefore at synchronous speed (i.e. slip $s = 0$) the rotor electrical frequency becomes zero. The zero frequency can be observed in that the three-phase rotor currents waveform momentarily reaching a DC state between $t = 9s$ and $t = 10s$.

6.7.3 A discussion on system operating conditions

Simulations have been performed thus far to validate individual controller performances, where dynamic responses are observed to ensure correctness of theoretical principles presented in previous chapters. In order to create a realistic virtual environment, physical system specifications as well as its operating conditions must be considered first. Several important aspects for the developed system operations are listed below:

- Only generator level control is implemented where power generation of the machine will be considered for fixed wind speed variations. Therefore constant input power is provided for the DFIG.

- The back-to-back converters connects the rotor to the grid through a step-up transformer. This is done to keep the DC-link voltage low, which then enables higher modulation index operations for the RSC.
- The DC-link and transformer secondary voltages are set at $300V$ and $100V$ respectively. This results in an initial modulation index of 0.6 for the three-level GSC, which provides sufficient latitude for DFIG variable speed operations.
- It has been demonstrated in subsection 6.5.2 that the three-level VSC exhibit similar output characteristics as the two-level VSC for small modulation indices. Due to RSC slip operations, the control voltages required for DFIG rotor excitation generally results in small modulation indices. Therefore in order to fully utilize all of the three-level VSC output states, it will be used for GSC operations.
- Typical DFIG operating speeds range between $\pm 25-30\%$ slip. Due to mechanical restraints on the laboratory machine set, a maximum slip of 20% is adopted in this dissertation.

6.7.4 Overall DFIG system simulations

In order to investigate DFIG system dynamics, operational power flow is illustrated in Figure 6-27 to compliment system simulations. As mentioned previously, motoring convention was adopted, therefore positive power flow is towards the generator.

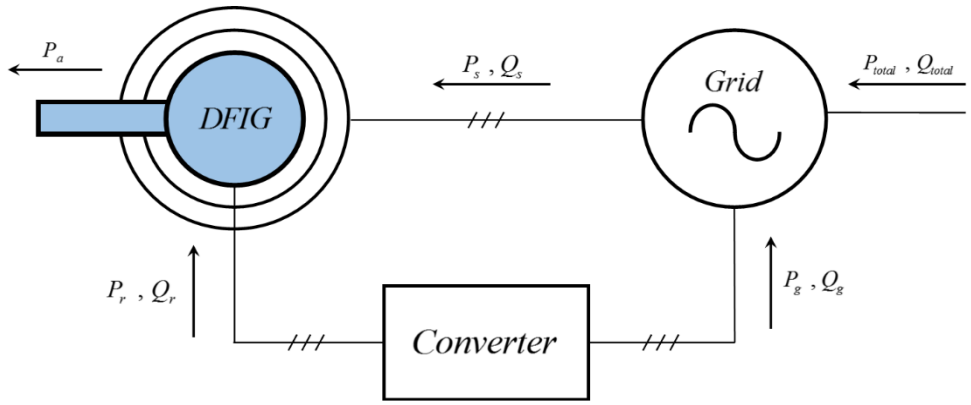

Figure 6-27: DFIG system operational power flow

Directional convention for all power flow is displayed here. If a 'lossless' system is assumed, then the following power equalities are approximately true:

$$\begin{aligned} P_r &\approx -P_g \quad Q_r \approx -Q_g \\ P_a &\approx P_s + P_r \approx P_{total} \\ \therefore P_{total} &\approx P_s + (-P_g) \\ \therefore Q_{total} &= Q_s + (-Q_g) \end{aligned} \tag{123}$$

The input mechanical power from the turbine P_a can be simulated by the following expression:

$$P_a = \omega_m T_a \tag{124}$$

The complete DFIG system operations are thus simulated based on Figure 6-27. Resulting waveforms for all relevant system dynamics are shown in Figure 6-28.

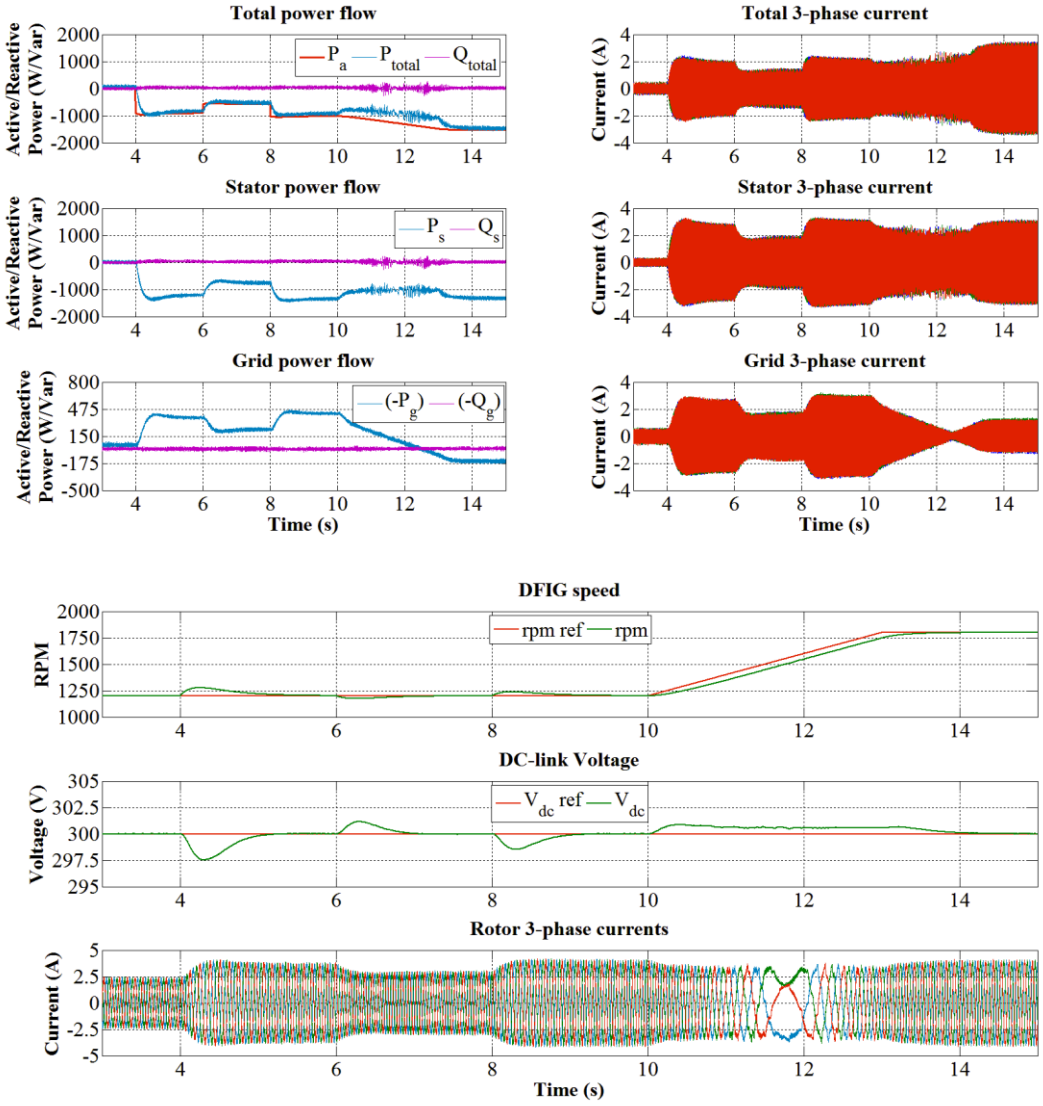

Figure 6-28: Simulated DFIG System dynamics

DFIG and GSC grid synchronisation are performed prior to $t = 3s$, thus results shown here depicts normal system operations. The input power P_a to the generator is initially varied by step changes in T_a at $t = 4s$, $t = 6s$ and $t = 8s$, where the shaft speed is fixed at 20% slip. The total active power output P_{total} is shown to equalise with P_a after shaft speed transients. It should be noted that P_{total} is the summation of P_s and P_g, since initially the generator is in sub-synchronous operation, therefore the relationship between P_s and P_g is subtractive where $P_{total} = P_s - P_g$. Between $t = 10s$ and $t = 13s$ P_a is

varied by accelerating the machine to a super synchronous slip of -20%, where T_a is kept constant. The resulting P_g during DFIG super synchronous operation has an additive relationship to P_s, thus $P_{total} = P_s + P_g$. It is observed that when the generator is operating close to its synchronous speed, significant amount of oscillation is present in P_s and hence P_{total}. Therefore prolonged DFIG operation in the vicinity of synchronous speed should be avoided. The DC-link voltage dynamics exhibit small variations for all simulated power transients hence further validating the controller design. Note the system reactive power has been regulated at zero throughout to enforce unity power factor operations.

The emulation of constant generator input power variations can be achieved by either varying DFIG speed or turbine aerodynamic torque T_a. In reality, the latter component cannot be controlled since its variation is dependent on the constantly fluctuation wind velocity. Therefore the generator speed should be controlled in accordance to the MPPT algorithm discussed in section 2.6, which should then optimise energy capture for the DFIG system. However, turbine control is outside of the scope of this dissertation, hence only correct operations for the DFIG controllers are ensured.

It can be concluded here that results shown in Figure 6-28 has fully verified expected system behaviours based on discussions in the preceding chapters. Full laboratory implementation for the developed DFIG system and corresponding experimental results are thus presented in chapters 7 and 8 respectively.

7. Laboratory Setup and Implementation

This chapter introduces the experimental implementation of the DFIG system in the laboratory. Integral components, both hardware and software, are discussed with respect to their functionalities. All relevant system parameters are either extracted from supplier datasheets or experimentally derived. In the latter case, a procedural description for experimental parameter identification is presented. Practical implementation issues are also discussed to justify, for the physical system, any design deviation from what was presented in the preceding chapters. All hardware related datasheets, drawings and documents are included in Appendix A at the end of this dissertation.

7.1 DFIG experimental test bench overview

In **Error! Reference source not found.** the basic configuration for a wind turbine driven DFIG is illustrated. Here the physical implementation of such a system is shown in Figure 7-1.

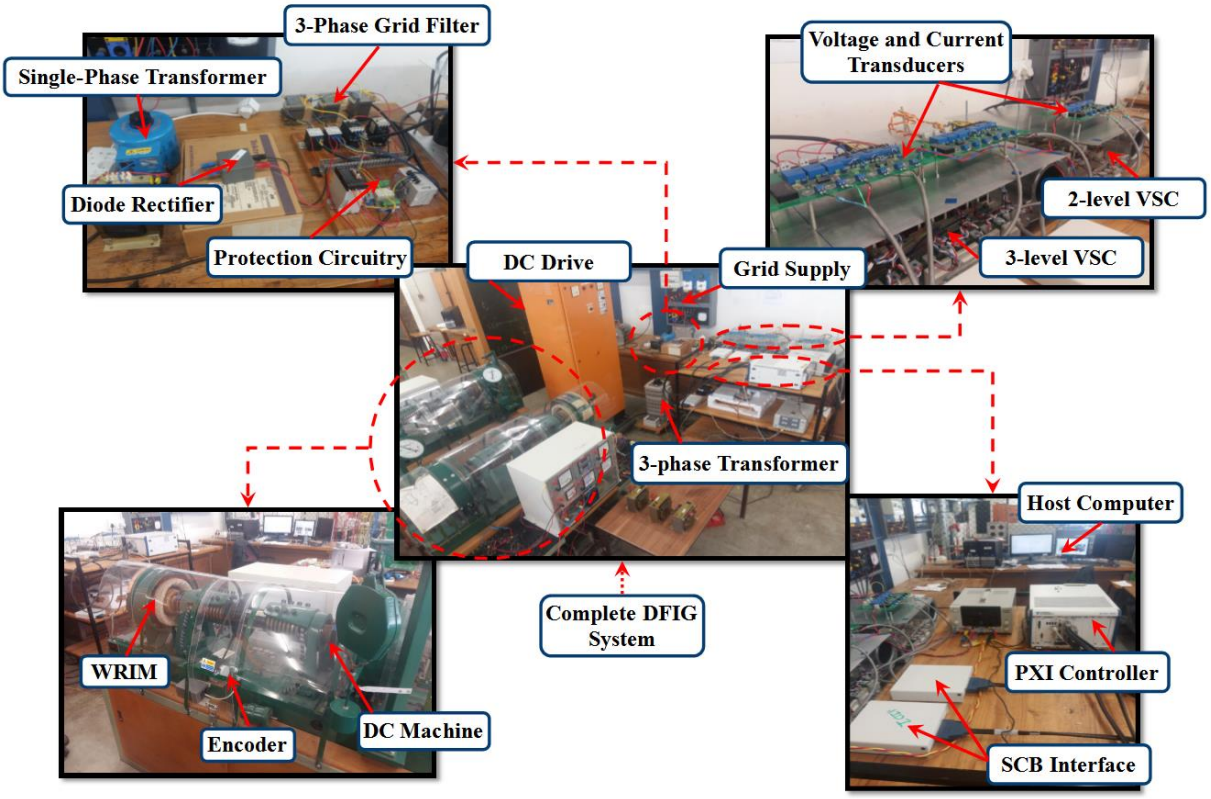

Figure 7-1: Hardware for the DFIG system

Based on hardware components shown in the above image, a brief description for the overall system operation is listed below:

- A wound rotor induction machine (WRIM) and a DC machine, directly coupled via their rotors, are used to emulate the wind-turbine-driven DFIG. The DC machine is driven by a thyristor stack to emulate basic turbine torque and speed variations. An incremental encoder is connected to the machine shaft for the purpose of obtaining instantaneous rotor angular position. The

WRIM rotor and stator windings are directly connected to a two-level VSC and a 380V grid supply respectively.

- A three-phase transformer is connected between the three-level GSC and grid supply in order to reduce operating DC-link voltage requirements as previously discussed. The single phase variable transformer, connected to a diode rectifier, is used to pre-charge the DC-bus.
- There are sixteen transducers in total for system voltage and current measurements.
- All system operations are processed by the PXI integrated controller. Run time commands can be sent to the controller from the host PC via an Ethernet connection.
- All electrical connections between the DFIG system and grid supply are protected by over current detection using digitally controlled contactors. Furthermore, low power devices within the system are fully isolated from high power components through the use of relays and operational amplifiers.

The above mentioned components are explained in detail, with respect to their operating characteristics and limitations, in the following section.

7.2 Hardware considerations for the DFIG system

Before assembling the complete DFIG system, its hardware components shown in Figure 7-1 are individually investigated to enable their safe and reliable implementation. Findings obtained are presented in this section to provide insight for the operations of these components.

7.2.1 PXI multipurpose real-time controller

The PXI controller is a National Instruments product designed for multipurpose real-time control applications. It consists of an enclosed chassis with multi-card slot features, where compatible expansion modules can be installed and synchronised to the same system clock.

Most of embedded PXI hardware can be programmed using the LabVIEW platform, either directly on the controller or through a remote host PC connected via Ethernet.

For this dissertation, an NI PXIe-1062Q chassis with three embedded components, shown in Figure 7-2, has been deployed to carry out all system control related tasks.

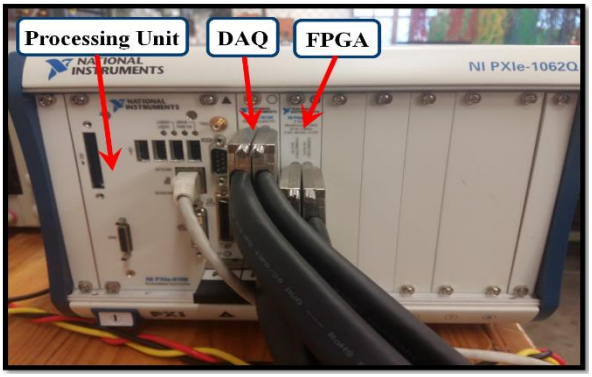

Figure 7-2: PXI integrated controller

Signals from PXI expansion cards are interfaced to other system devices via shielded connector boards (SCB) with shielded data cables. These accessories, shown in Figure 7-3, can be setup for analog or digital signal transmissions.

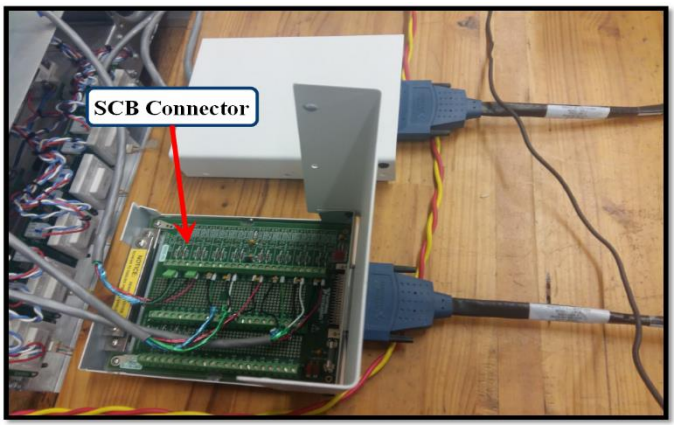

Figure 7-3: SCB connectors

Brief descriptions for each embedded PXI component functionalities are described in the following subsections.

7.2.1.1 Data acquisition device (PXIe-6363)

The PXIe-6363 is a data acquisition (DAQ) card. It has 16 differential analog input channels with a maximum sample rate of 1MS/s multiplexed between each channel used. In addition, it has 4 analog and 48 digital output channels that are respectively capped at maximum data rates of 2.88 Ms/s and 10 Ms/s.

All 16 input channels on the DAQ card are used for system measurements listed below:

- Three-phase grid voltage
- Three-phase stator voltage
- Three-phase grid current
- Three-phase stator current
- Three-phase rotor current
- DC-link voltage across top capacitor and bottom capacitor

Measurement signals from voltage and current transducers are interfaced to the DAQ via SCB connectors. An URL link for the PXIe-6363 datasheet is provided in Appendix A.

7.2.1.2 Processing unit (PXIe-8108)

The PXIe-8108 is an Intel Core 2 Duo embedded controller. Although it can be used for control applications, its ability to execute deterministic processing tasks decrease with higher CPU loads. This could cause deterioration in controller reliability. Therefore it is only used for synchronising system

communication and providing a reliable user interface. Actual system control tasks are performed using the FPGA card detailed next.

7.2.1.3 Field Programmable Gate Array (FPGA PXI-7813R)

The PXI-7813R is an FPGA card that has a maximum logic rate of 40MHz with 160 configurable digital lines. It is capable of executing logical statements at extremely high speeds up to a maximum of 25ns resolution. Furthermore, it is capable of true parallel computing where different tasks can be performed simultaneously. Thus FPGA is an ideal choice for implementing control and PWM switching operations. However, its device resources are limited, therefore computational efficiency and memory utilization must be carefully considered when programming the FPGA card. The digital lines can be configured as inputs and outputs which are interfaced with external devices via SCB connectors. An URL link for the PXI-7813R datasheet is provided in Appendix A.

7.2.2 Converters

Figure 7-4 shows the two-level and three-level VSC's independently, and when they are connected in a back-to-back configuration. The three-level VSC forms part of the grid-side control whereas the two-level VSC forms part of the rotor-side control. Note these images are taken during early stages of laboratory prototyping, therefore they do not resemble final physical locations of these components in the system.

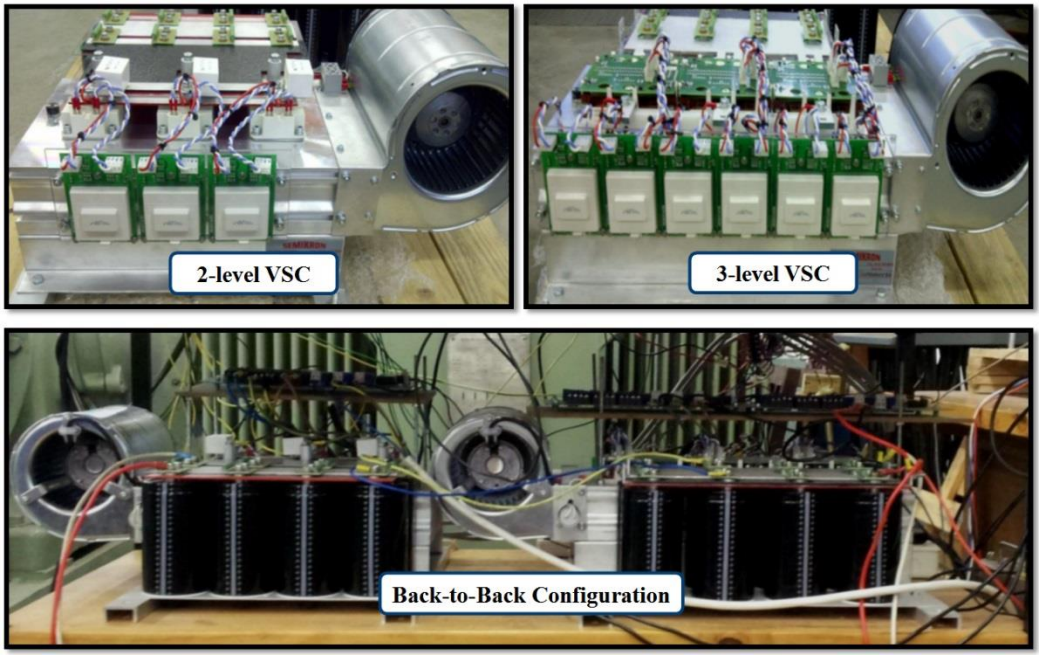

Figure 7-4: Individual VSC's and their back-to-back configuration

Both VSC's are manufactured by Semikron, with built-in DC capacitors. When both converters are connected back-to-back, total DC-link capacitance is rated at $18800\mu F$. In addition, each converter also consists of IGBT modules and corresponding gate driver PCB's.

7.2.2.1 Insulated Gate Bipolar Transistors (IGBT's)

For the three-level converter, Semikron SkimMLI200 IGBT modules are used for modulation. Each module consists of four IGBT's that has individual voltage and current ratings of 1200V and 200A respectively. For the two-level converter, Semikron SKM144GB123D IGBT modules are used. Each module consists of two IGBT's that has individual voltage and current ratings of 1200V and 145A respectively. These IGBT modules are separately shown in Figure 7-5, their respective datasheets are provided in appendix A.

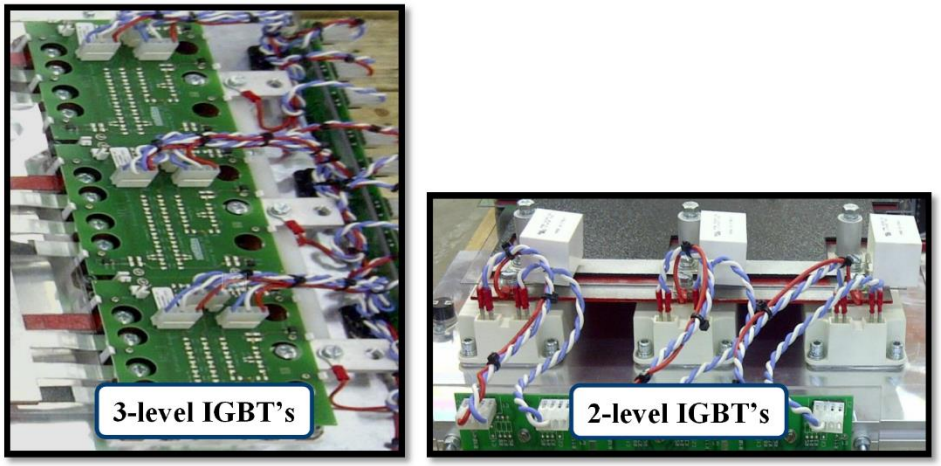

Figure 7-5: Semikron 3-level (SkimMLI200) & 2-level (SKM144GB123D) IGBT modules

The rating of these power electronic devices actually far exceeds the ratings of the DFIG. This is a limitation within this dissertation where existing lab equipment are used to develop the system. That being said, given a pair of converters that are over rated, the finalised drive system can be easily implemented on different machines with higher power requirements.

7.2.2.2 Gate drivers

To provide gating signals for the IGBT's, Semikron SKHI22BR driver boards are used for both converters. In addition, these drivers have various built-in protection measures for both IGBT's and external controlling circuits. The two most important features are IGBT collector-emitter voltage monitoring and signal transmission via opto-couplers. The former provide short circuit protection and the latter facilitates isolation between external control circuits and the IGBT's. A component image for the SKHI22BR, and its corresponding inputs are shown in Figure 7-6.

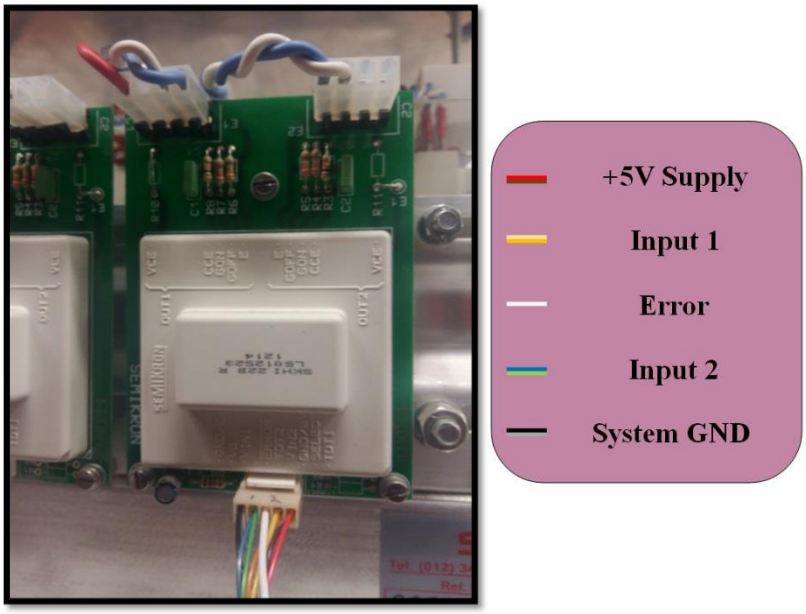

Figure 7-6: Semikron SKHI22BR

The driver inputs accept control voltages of 0V=off and +5V=on, then outputs gate-emitter signals of -7V=off and +15V=on for the IGBT's via the opto-coupler. External components can be placed on the PCB to set SKHI22BR output characteristics. The most important settings are listed below:

- **Gate turn-on and turn-off times** - this is set by gating resistors R_{ON} and R_{OFF} which must have values above 3Ω specified by Semikron.
- **Switch interlocking time** - this feature provides a built-in dead-time to ensure both IGBT's are off before the alternate IGBT is switched on. The factory setting of $4\mu s$ is used as it provides a good safety margin, however, it may be altered by varying the connections to the configuration pins.
- **Collector-emitter voltage monitoring –** the threshold voltage V_{CEstat} for short circuit detection may be altered by choosing a suitable resistor R_{CE} . In addition, a parallel capacitor C_{CE} can be connected to alter the blanking time before V_{CE} monitoring is activated.

Component value calculations for the above mentioned settings are extracted from the manufacturer datasheet and summarised in Table 7-1.

Table 7-1: SKHI22BR component setting calculations

Component	Function	Value determination
R_{CE}	Collector-emitter threshold voltage	$V_{CEstat} = \frac{10R_{CE}(k\Omega)}{10+R_{CE}(k\Omega)} - 1.4$
C_{CE}	Blanking time of V_{CE} monitoring	$t_{\min} = \tau_{CE} \ln\left(\frac{15-V_{CEstat}}{10-V_{CEstat}}\right)$ $\tau_{CE}(\mu s) = C_{CE}(nF)\frac{10R_{CE}(k\Omega)}{10+R_{CE}(k\Omega)}$
R_{ON}	Gate turn-on time	$R_{ON} > 3\Omega$
R_{OFF}	Gate turn-off time	$R_{OFF} > 3\Omega$

If an error is detected by either the interlocking mechanism or V_{CE} monitoring, a corresponding signal V_{Error} is generated by the driver. The logic values for V_{Error} is +15V during healthy conditions and 0V if an error has been detected. These signals can thus be registered by the controller for appropriate system shut down operations.

Detailed circuit schematics, setup instructions and operating characteristics for the Semikron SKHI22BR driver boards can be found in its datasheet, where its URL link is provided in Appendix A.

7.2.2.3 Signal level shifter

Control inputs for the gate drivers are generated by the FPGA (PXI-7813R) digital lines. The logic output voltage from the FPGA is +3.3V=on and 0V=off. In order to meet the +5V requirement for the driver input voltages, an interface circuit is separately designed to shift all signals from the FPGA to +5V. This operation is accomplished by using quad two-input AND gates (MN74HC08). The actual

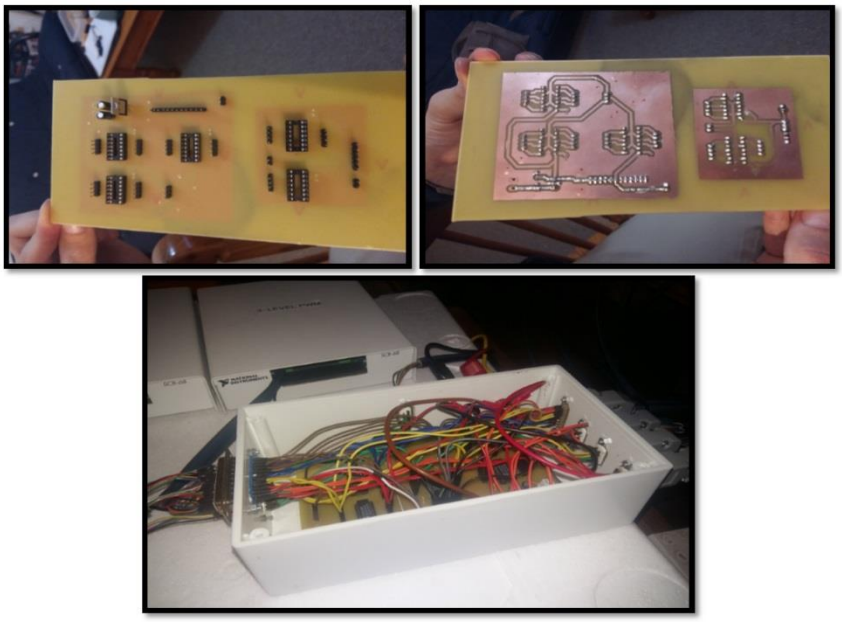

Figure 7-7: Customised signal level shifter

circuit for the level shifter is shown in Figure 7-7, where the corresponding schematic and component datasheets are provided in Appendix A.

7.2.3 Current and voltage transducers

Voltage and current measurements are performed using specialised transducers. The output low voltage signals are then sent to the DAQ card for processing. The LEM modules are used to accomplish all

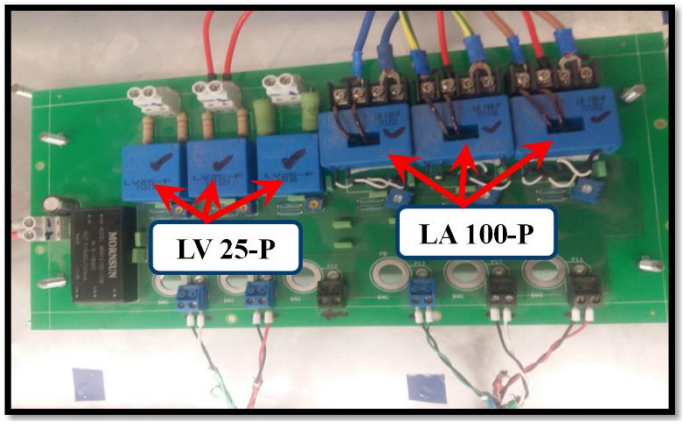

Figure 7-8: LEM integrated PCB

measurement related tasks. Seven voltage LEM modules (LV 25-P) and nine current LEM modules (LA-100-P) are used to obtain system measurements described in subsection 7.2.1.1. These modules are all mounted on custom PCB's which are further mounted on top of the converters. Figure 7-8 shows the LEM integrated PCB, where relevant datasheets and schematics are provided in Appendix A.

The external circuit components connected to the LEM modules must be properly chosen so as to ensure voltages and currents stay within the maximum range and that saturation does not occur. These component settings are discussed in the following subsections.

7.2.3.1 LEM's LA 100-P

The current transducers have nominal rms current ratings of 100A and 50mA for its primary and secondary sides respectively. Figure 7-9 displays the internal circuitry for the LA 100-P modules.

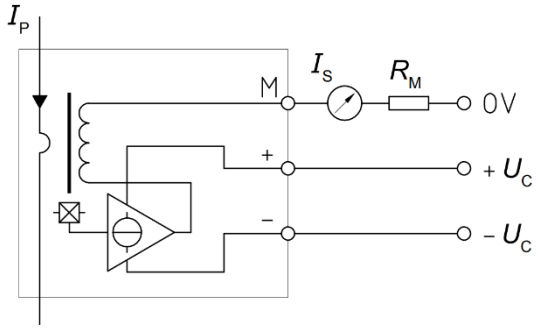

Figure 7-9: LA 100-P internal circuitry

The attenuation ratio for the device, considering its nominal ratings, is 2000:1 between the primary and secondary side currents (I_P, I_s). Apart from the required external supply voltage $\pm U_c$, a resistor R_M must be connected on the secondary side to limit output current as well as setting the scaling ratio.

The output resistance R_M is provided by a potentiometer on the custom PCB, where its value can be tuned to give desired scaling factor. Manufacturer recommended input voltage range for the DAQ is $\pm 10V$, whereas the system rated current from the generator is $5A$. Therefore the maximum primary measuring range has been set to $25A$ catering for any possible over current conditions, where the corresponding maximum secondary output voltage is set to $10V$. This is achieved by tuning the potentiometer so that $R_M = 800\Omega$, and the consequent scaling factor between primary current and secondary voltage is 2.5.

7.2.3.2 LEM's LV 25-P

The voltage transducers have nominal $_{rms}$ current ratings of 10mA and 25mA for its primary and secondary sides respectively. Figure 7-10 displays the internal circuitry for the LV 25-P modules.

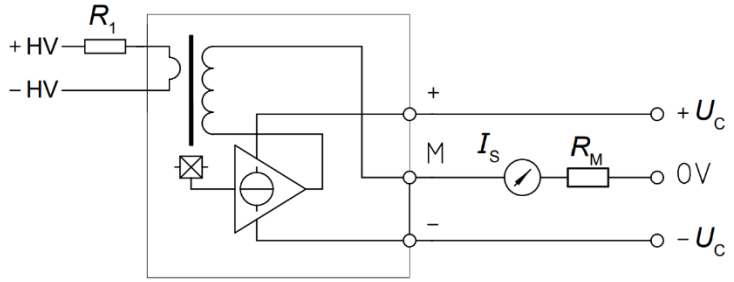

Figure 7-10: LV 25-P internal circuitry

The attenuation ratio for the device, considering its nominal ratings, is 1:2.5 between the primary and secondary side currents (I_P, I_s). An output resistor must be connected on the secondary side for the same reasons as in the case of the current transducer. In addition a resistor R_1 must be connected on the primary side to limit current flow.

The scaling factor for all voltage measurements is set to 90 between primary and secondary sides. This is accomplished by choosing resistance values so that $R_1 = 50k\Omega$ and $R_M = 220\Omega$. Resulting maximum measuring range on the primary side is thus $500V$ with a corresponding maximum secondary voltage of $5.5V$.

7.2.4 Incremental Encoder

The incremental encoder is used to obtain angular position of the rotor. The RS58-0/1000 shaft encoder, from Texas Instruments, has been implemented due to its availability in the lab. It has a resolution of 1000 pulses per revolution, and a maximum speed measuring range up to 10000 rpm. The encoder, shown in Figure 7-11, is coupled to the machine rotor through a unity gearing system.

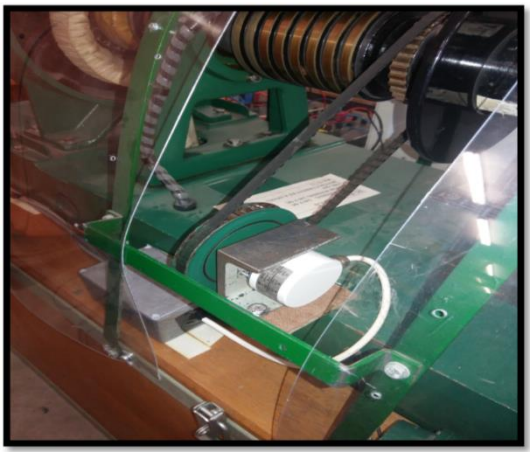

Figure 7-11: Mounting for the incremental encoder

The encoder has two output channels, A and B, which individually generates 1000 pulses per revolution. The digital signals from B are 90^{o} phase shifted from that of A. Thus 4000 counts per revolution can be obtained from both A and B to represent the rotor angular position. The encoder also generates an index pulse, which can be used to reset the counting of pulses after each revolution. The electrical circuit inside the encoder requires a +5V supply, this is provided by the PXI controller.

The rotor angular position θ_m in radians with respect to encoder output pulse counts can be determined by:

$$\theta_m = \frac{2\pi}{4000} count \tag{125}$$

It must be emphasised θ_m in (125) represents rotor mechanical angular position, which must be converted to electrical radians for synchronous transformation of rotor electrical quantities. The rotor mechanical angular speed can thus be calculated by:

$$\omega_m = \frac{\theta_m(k-1) - \theta_m(k)}{T_{samp}} \tag{126}$$

Expression (126) is a simple shift register operation where k and T_{samp} represents controller sampling instance and period respectively. For reliable speed determination from angular position samples, it is vital to ensure a constant T_{samp}. This can be easily achieved by the FPGA, therefore it is used to decode the quadrature encoder pulse counts.

It was discovered during laboratory implementation that the digital encoder output signals are easily compromised by environmental noises, which originates from machine rotor PWM excitations. In order to preserve data transmitted by the encoder, a common radio frequency signal conditioning technique has been adopted. The signals are passed through a quad differential line driver (AM26LS31CN), which converts TTL signals from the encoder to differential signals that are known to have better resistance to electrical noises. The transmitted signals are then converted back to TTL format at the controller end by

using a quad differential receiver (AM26LS31ACN). This is a required operation as FPGA inputs are not differential compatible. In addition, twisted pair cables with properly earthed shields are used to further improve signal transmission quality. Figure 7-12 shows circuits used for the differential line driver-receiver pair.

Detailed specifications for the incremental encoder, line driver and receiver can be found in corresponding datasheets provided in Appendix A.

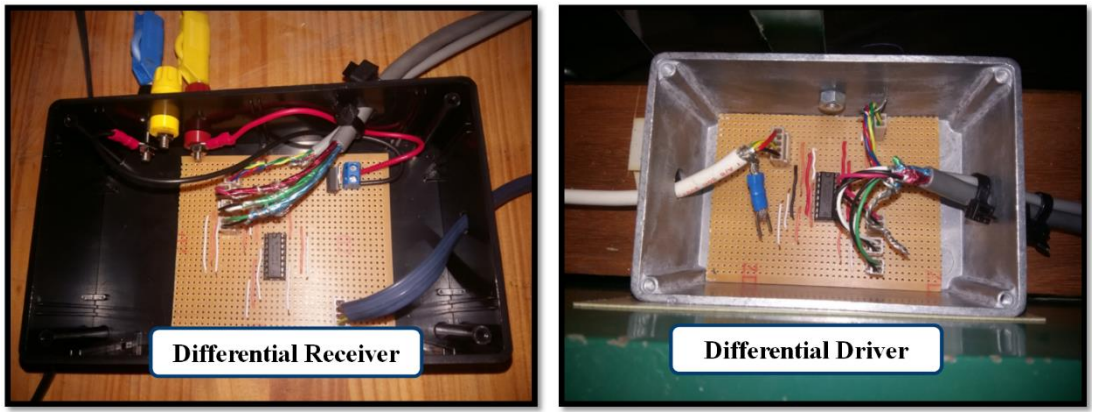

Figure 7-12: Differential line driver-receiver pair

7.2.5 System protection

All error signals, generated by the converter driver boards and controller overcurrent detection, are buffered by operational amplifiers with clamping diodes to prevent large feedback voltage to the controller I/O in the case of circuit malfunction. The buffer circuit outputs are connected to the 24V relay low voltage terminals, where the 230V high voltage terminals of the relays are further connected to contactors where switching commands are registered. This effectively isolates the low power devices

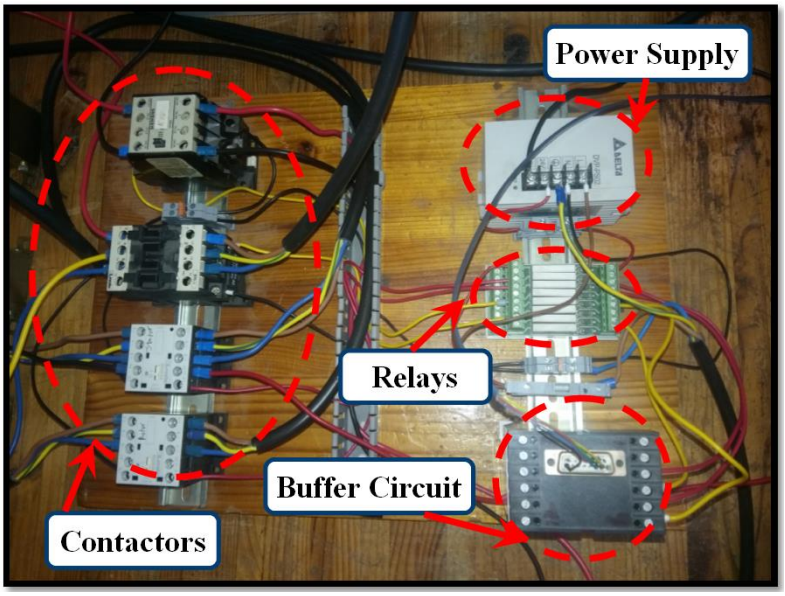

Figure 7-13: System protection circuitry

from high power components in the system. A dedicated power supply provides the operating voltage required by the relays and the buffer circuit. The system protection scheme is demonstrated in Figure 7-13, where all relevant components are labelled.

From Figure 7-13 there are four contactors, where one of them is a single phase contactor for the DC-link pre-charge operation. The rest are three-phase contactors that provides protection for the following electrical connections: Grid and three-level GSC; Grid and DFIG stator; DFIG rotor and two-level RSC.

7.2.6 DC drive

An available DC drive in the laboratory is used to control the separately excited DC machine directly coupled to the WRIM. The two-quadrant drive, essentially consisting of a thyristor stack, is responsible to provide speed and torque control for the DC machine so as to emulate wind turbine start-up and power variations respectively. The DC machine is rated at 1.5kW, therefore rated power for the 2.2kW WRIM cannot be achieved. The field of the DC machine is excited from a 220V DC supply. The thyristor DC drive enclosed in a cabinet is shown in Figure 7-14.

Figure 7-14: Thyristor DC drive

7.2.7 System parameter identification

In order to facilitate a robust controller design, it is integral to have an accurate system model where all parameters are known. Therefore experimental procedures for identifying relevant DFIG system component parameters are presented in this subsection.

7.2.7.1 DFIG circuit parameters

The DFIG circuit parameters are required for its rotor current controller design. The machine used is a three-phase, 2.2kW, 380V, 50Hz, 4-pole wound rotor induction machine as shown in Figure 7-15.

Figure 7-15: Implemented wound rotor induction machine

In order to determine the induction machine circuit parameters, standard 'No load' and 'Blocked rotor' tests are performed. In addition, an 'Open rotor' test has been carried out for the purpose of determining the effective stator to rotor turns ratio.

- No load test

Information regarding no load impedance can be obtained from the no load test for an induction machine. During the test, rated three-phase voltages at rated frequency are applied to the stator windings. The machine rotor do not have any mechanical couplings and its windings are shorted together [52]. The resulting per-phase no load equivalent circuit for the wound rotor induction machine is shown in Figure 7-16.

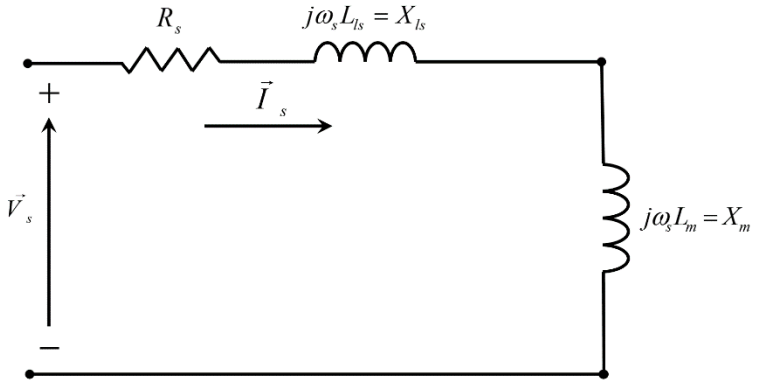

Figure 7-16: Steady-state per-phase WRIM equivalent circuit for no load test

All circuit parameters here has been defined in chapter 2. The stator resistance can be directly measured using a multimeter and is found to have the value of $R_s = 6.6\Omega$. The YOKOGAWA WT1800 power analyser is used to obtain no load test measurements shown in Table 7-2.

Table 7-2: Measured results for WRIM no load test

	Phase A	Phase B	Phase C
$V_s^{rms}(V)$	218.61	223.04	219.55
$I_s^{rms}(A)$	1.38	1.39	1.41
$P_{NL}(W)$	87.4	94	88.3
$Q_{NL}(Var)$	289.3	295.7	297.1

The total three-phase no load active and reactive power can be calculated by summing up per phase values, which results in that:

$$P_{NL}^{total} = 269.7W \qquad Q_{NL}^{total} = 882.1Var$$

The per-phase no load resistance R_{NL} and reactance X_{NL} can be calculated using an averaged stator current:

$$R_{NL} = \frac{3P_{NL}^{total}}{\sum I_{sj}^2} = 46.18\Omega$$

$$X_{NL} = \frac{3Q_{NL}^{total}}{\sum I_{sj}^2} = X_m + X_{ls} = 151.05\Omega$$

- Blocked rotor test

Information regarding leakage impedances as well as rotor resistance can be obtained from the blocked rotor test for an induction machine. During the test, the rotor is mechanically clamped to remain stationary while rated currents are supplied to the stator windings [52]. The resulting per-phase blocked rotor equivalent circuit for the wound rotor induction machine is shown in Figure 7-17.

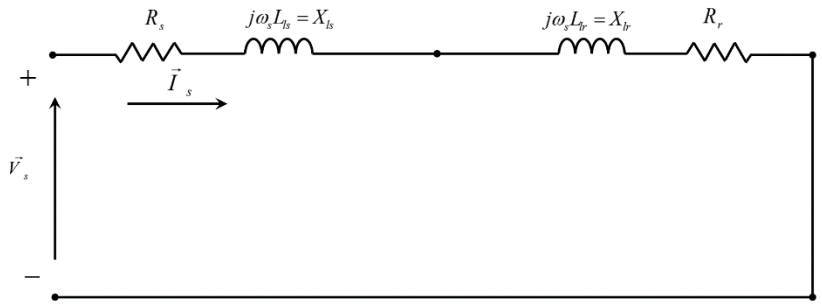

Figure 7-17: Steady-state per-phase WRIM equivalent circuit for blocked rotor test

It should be noted that all circuit parameters here has been referred to the stator as discussed in chapter 2. The YOKOGAWA WT1800 power analyser is used to obtain blocked rotor test measurements shown in Table 7-3.

Table 7-3: Measured results for WRIM blocked rotor test

	Phase A	Phase B	Phase C
$V_s^{rms}(V)$	81.94	83.74	82.33
$I_s^{rms}(A)$	3.91	3.85	3.85
$P_{NL}(W)$	178.95	177.07	179.44
$Q_{NL}(Var)$	265.65	269.04	263.8

The total three-phase blocked rotor active and reactive power can be calculated by summing up per phase values, which results in that:

$$P_{BL}^{total} = 535.46W \qquad Q_{BL}^{total} = 798.49Var$$

The per-phase blocked rotor resistance R_{BL} and reactance X_{BL} can be calculated using an averaged stator rated current:

$$R_{BL} = \frac{3P_{BL}^{total}}{\sum I_{sj}^2} = 11.94\Omega$$

$$X_{BL} = \frac{3Q_{BL}^{total}}{\sum I_{sj}^2} = X_{ls} + X_{lr} = 17.80\Omega$$

It is usually acceptable to assume that the stator and rotor reactance are the same, especially for smaller machines [52], therefore per-phase stator, rotor and magnetising reactance and their corresponding inductances for a $50Hz$ stator supply can be calculated as:

$$X_{ls} = X_{lr} = \frac{X_{BL}}{2} = 8.90\Omega$$

$$X_m = X_{NL} - X_{ls} = 142.15\Omega$$

$$X = 2\pi fL$$

$$\therefore L_{ls} = L_{lr} = \frac{X_{BL}}{4\pi f} = 0.0283H$$

$$\therefore L_m = \frac{X_m}{2\pi f} = 0.4525H$$

The per-phase rotor resistance may then be calculated as:

$$R_r = \left(\frac{X_{lr} + X_m}{X_m}\right)^2 \left(R_{BL} - R_s\right) = 6.02\Omega$$

- Open rotor test

Information regarding the induction machine stator-rotor effective turns ratio can be obtained from this test. It is important to determine this machine parameter, since it must be used for scaling the rotor current controller output, which has been referred to the stator, to actual excitation voltages required by the rotor windings. During the test, voltage is supplied to the stator windings with small increments whereas the rotor windings are open circuited. The resulting per-phase open rotor equivalent circuit for the wound rotor induction machine is shown in Figure 7-18.

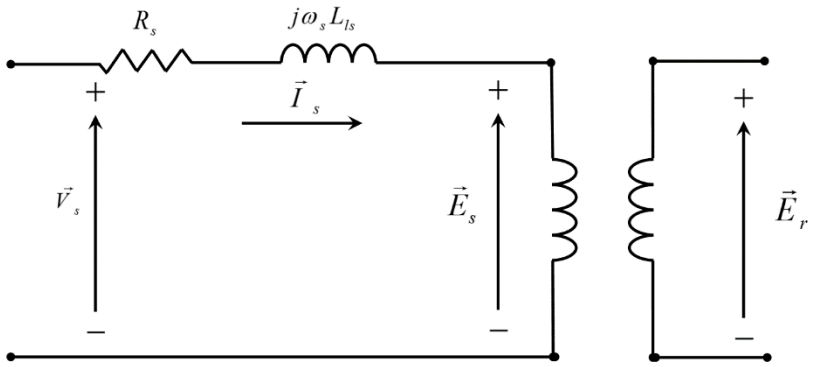

Figure 7-18: Steady-state per-phase WRIM equivalent circuit for open rotor test

For small voltages supplied, stator winding losses can be considered negligible. Therefore the ratio between stator supply voltage and induced voltage at the open rotor terminals, can be considered as a close representation of the effective-turns-ratio. Open rotor voltage measurements are gathered for different stator voltage supplied, results are shown in Table 7-4.

Table 7-4: Measured results for WRIM open rotor test

Supplied stator RMS voltage (V)	**Induced rotor RMS voltage (V)**	**Ratio ($\frac{V_s}{V_r}$)**
11.62	10.81	1.07
23.4	21.7	1.07
33.5	31.4	1.07
64.2	61.6	1.04
84.9	81.4	1.04
108.58	104.1	1.04
138.6	132.9	1.04

From the above results it is assumed that the machine has a stator-rotor effective-turns-ratio of approximately one. Therefore, the rotor current controller output does not need to be scaled.

- Summary of DFIG electrical circuit parameters

Table 7-5 is a summary of DFIG circuit parameters obtained from the test procedures presented in this section. These parameters can then be used for computing rotor current controller gains as presented in section 3.8.

Table 7-5: Summary of DFIG circuit parameters

Circuit parameter	Value
Stator Resistance	$R_s = 6.6\Omega$
Stator leakage inductance	$L_{ls} = 0.0283H$
Magnetizing inductance	$L_m = 0.4525H$
Rotor leakage inductance	$L_{lr} = 0.0283H$
Rotor resistance	$R_r = 6.02$
Effective-turns-ratio	$n = \frac{N_s}{N_r} \approx 1$

7.2.7.2 Combined machine set rotor inertia

The combined rotor inertia between WRIM and DC machine is needed for the DFIG speed controller design. This mechanical parameter can be obtained by performing a machine retardation test [66]. The procedure requires the machine to be accelerated above its no load speed. Then electrical supplies to the machine is cut-off, and hence the rotor is let free to slow down to a standstill. In the absence of an electrical supply, the dynamic model expressed in (11) for the DFIG mechanical drive train, can be written as:

$$J\frac{d\omega_m}{dt} = -T_m \tag{127}$$

Given that the rotor is not loaded, then T_m in (127) can be described as a retarding torque imposed on the drive train purely due to rotor inertia and friction. The generic deceleration form for a first order differential equation, such as the one in (127), is shown in Figure 7-19.

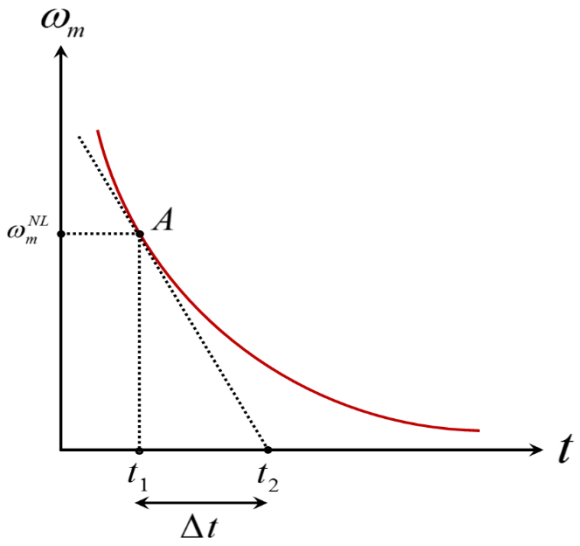

Figure 7-19: Machine deceleration curve

If we take A on the deceleration curve in Figure 7-19 as the point where machine has reached no load speed ω_m^{NL}, then (127) can be expressed with respect to this operating point as:

$$J \left. \frac{d\omega_m}{dt} \right|_{\omega_m = \omega_m^{NL}} = -T_m^{NL} \tag{128}$$

The rotor inertia J in (128) can be calculated if two variables are known:

- The tangent $\left. \frac{d\omega_m}{dt} \right|_{\omega_m = \omega_m^{NL}}$ of the deceleration curve at $t = t_1$ corresponding to no load speed.
- The no load torque T_m^{NL}.

The first can be easily calculated from the deceleration curve, whereas the no load torque is difficult to obtain. Therefore, the latter variable's relationship with mechanical power losses at no load speed should be considered:

$$P_m^{NL} = \omega_m^{NL} T_m^{NL} \tag{129}$$

Substituting (129) into (128) results in the following expression for computing the machine inertia:

$$J = -\frac{P_m^{NL}}{\omega_m^{NL} \left. \frac{d\omega_m}{dt} \right|_{\omega_m = \omega_m^{NL}}} \tag{130}$$

The mechanical losses at no load speed P_m^{NL} can be obtained using the segregation of losses method [67], by considering the power balance within an induction machine operating at no load speed. This can be expressed as:

$$P_{in} = P_{cu} + P_{iron} + P_m^{NL} \tag{131}$$

The total input power P_{in} and machine copper losses P_{cu} can be determined easily given that operating voltages and currents are known. To segregate the iron losses P_{iron} from P_m^{NL}, its linear relationship with respect to the square of the supply voltage must be used [66], which can be expressed as:

$$\begin{aligned} P_{iron} + P_m^{NL} &= f\left(V_s^2\right) = P_{in} - P_{cu} \\ P_{in} &= 3V_s I_s \\ P_{cu} &= I_s^2 R_s \end{aligned} \tag{132}$$

Therefore after performing a no load test as discussed in subsection 7.2.7.1, the stator supply voltage should be slowly decreased until machine speed drops. Measurements are taken so as to allow the computation of $P_{in} - P_{cu}$. This experiment has been carried out in the laboratory, where $P_{in} - P_{cu}$ are

calculated for each decrement in stator supply voltage. The characteristic $P_{iron} + P_m^{NL} = f\left(V_s^2\right)$ is thus graphed as shown in Figure 7-20 based on results collected.

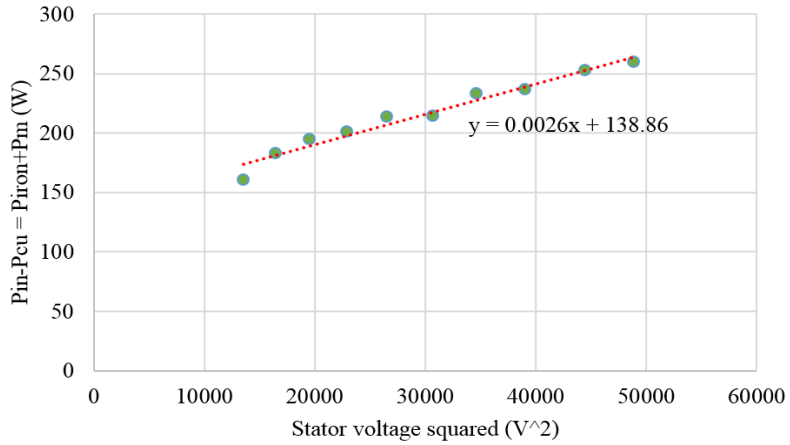

Figure 7-20: Segregation of $P_{iron} + P_m^{NL} = f\left(V_s^2\right)$

The characteristic equation $y = 0.0026x + 138.86$ shown in Figure 7-20 is a direct reflection of $P_{iron} + P_m^{NL} = f\left(V_s^2\right)$. Since no load mechanical losses do not depend on stator voltage variations, therefore the characteristic y-axis intercept 138.86 forms the numerical value for P_m^{NL}.

Finally the experimental deceleration curve, shown in Figure 7-21, is obtained by performing a retardation test on the machine set.

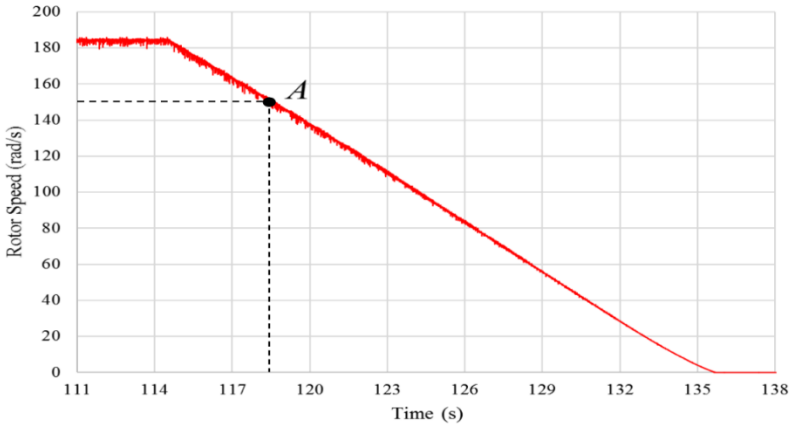

Figure 7-21: Experimental deceleration curve for the WRIM and DC machine set

The machine no load speed is determined as $154.8 rad/s$ and the tangent at point A is calculated to be $\left.\frac{d\omega_m}{dt}\right|_{\omega_m=\omega_m^{NL}} = -8.469 m/s^2$. Substituting the numerical values for $\left.\frac{d\omega_m}{dt}\right|_{\omega_m=\omega_m^{NL}}$ and P_m^{NL} into (130), the combined inertia for the experimental machine set is calculated to be:

$$J = 0.1051 \ kg.m^2$$

7.2.7.3 Grid filter circuit parameters

The three-phase grid filter used for laboratory implementation is shown in Figure 7-22. It consists of three inductors that each has an inductance of $47mH$ specified by the manufacturer, and a parasitic resistance of 0.75Ω determined by using an LCR tester. The saturation current limit for each inductor is rated at $5A$. These parameters are used for computing grid current controller gains.

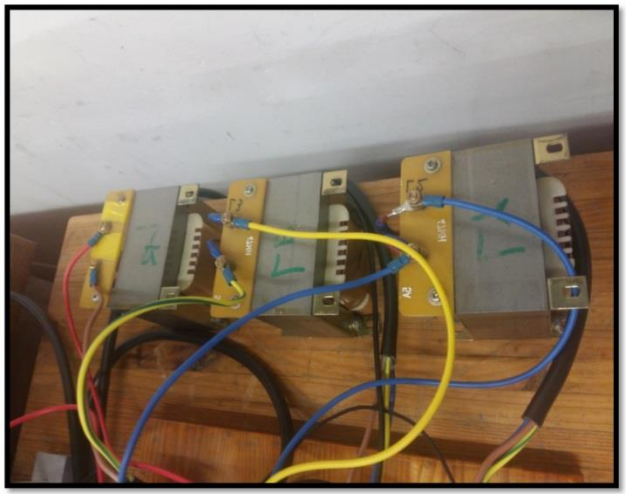

Figure 7-22: Laboratory three-phase grid filter

The gain characteristic for the grid filter can be derived from the modulus of (86) as:

$$s = j\omega$$

$$|G(j\omega)| = \frac{1}{\sqrt{L_g^2\omega^2 + R_g^2}} \tag{133}$$

The back-to-back converter switching frequency is set to $2kHz$, substituting this frequency as well as filter parameters into (133), the filter inductor signal attenuation at the switching frequency is found to be $|G(j\omega)| = 0.00169$. This means the filter is more than sufficient to eliminate switching frequency harmonics caused by converter PWM operations.

7.3 Software architecture for the developed DFIG system

Essentially four software packages are critical in the development and final implementation of the DFIG system. These packages are listed below:

- Matlab/Simulink
- LabVIEW FPGA
- Xlinx compilation tool for FPGA
- LabVIEW RT

All simulation results shown in chapter 6 has been obtained in Matlab/Simulink which forms the most crucial part within the initial system design stage.

All the controllers as well as the converter modulation algorithms are implemented on the FPGA card embedded in the PXI controller. Control signals are sent from the FPGA configurable digital I/O's to converter drivers as well as system protection circuits. The corresponding programming kit for the hardware is LabVIEW FPGA, which has a graphical coding environment similar to Simulink. To transform the graphical code in LabVIEW to actual routing maps for the FPGA logic gates, the Xlinx compilation tool must be co-installed with LabVIEW FPGA.

Measurements acquired by the LEM modules are sent to the PXI DAQ. In order to extract sampled data information from the DAQ buffers, the processing unit must be programmed to do so using LabVIEW RT. The acquired data can then be sent to the FPGA for control processing by opening referenced channels in RT. These input and output channels are respectively known as controls and indicators in the LabVIEW programming environment. The structure of data flow between different PXI hardware and their corresponding software packages are shown in Figure 7-23.

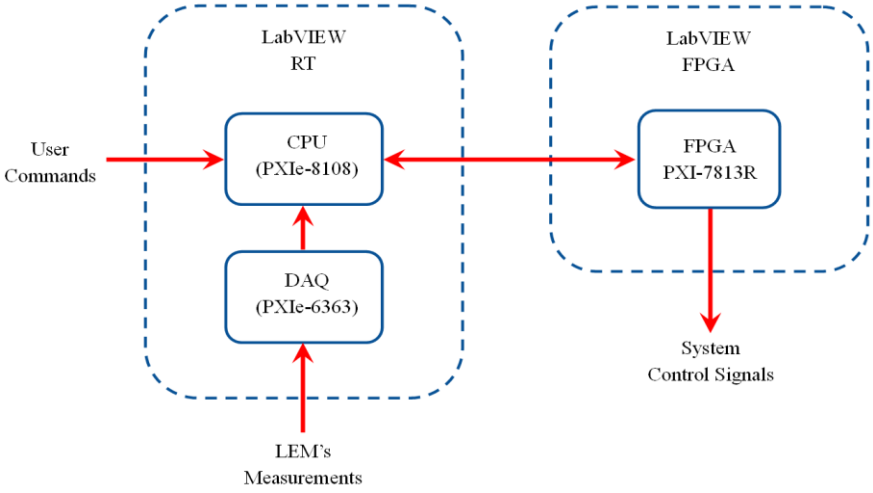

Figure 7-23: Data flow between PXI hardware and software packages

LabVIEW RT also provides powerful toolboxes for robust graphical user interface (GUI) designs. A sample of the interface designed for monitoring and control of the laboratory DFIG system is shown in Figure 7-24.

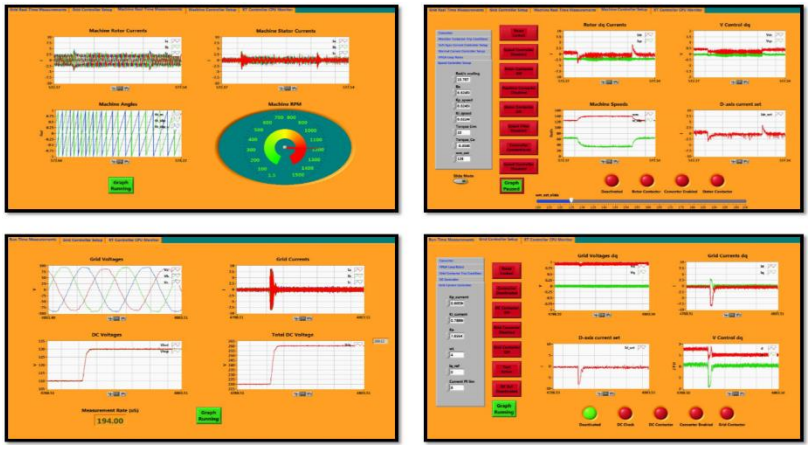

Figure 7-24: DFIG system control user interface in LabVIEW

The user interface has been designed so that an operator, without in depth knowledge about the system hardware, may navigate through system operations with relative ease. Various functionalities are included in the interface, these are listed below:

- Real-time system signal monitoring through LabVIEW scopes. These waveform charts contain a fixed number of samples, which can be exported as images or data points. In addition, run-time pausing and analysis functions such as zoom in/out may be performed.
- System control can be performed with Boolean controls. Relevant indicators signifies various system component statuses to the user.
- System settings can be altered prior to operations or directly during run-time. These settings include system protection limits, controller gains, controller references and sampling rates of various functions.
- Run-time CPU usage monitoring has been included for the precipitation and prevention of software related failures.
- Fail safe system shut down can be performed.

8. Experimental Results and Discussion

Experimental results are presented and discussed in this chapter. These results have been obtained from the laboratory setup presented in chapter 7. As the objective of this dissertation is to design and implement a DFIG test bench, experimental results are compared to the simulated results presented in chapter 6. Validation with respect to converter modulation, controller responses and overall system behaviour are thus presented.

All experimental results are extracted from LabVIEW scopes embedded in the designed user interface, with the exception of converter PWM voltage waveforms. Testing conditions for the experimental system resembles the simulations in all regards.

8.1 Converter modulation experimental validation

Before implementing the controller for the system, converter modulation for both two-level and three-level VSC's are first validated. Test conditions are kept identical to the simulations presented in section 6.5.

The DC-bus voltage is kept at $300V$ supplied by a single phase variac, where output terminals of the converters are connected to a three-phase RL load with per-phase parameters $R = 300\Omega$ and $L = 47mH$. Due to sampling frequency restriction of the PXI DAQ, the converter PWM output voltage waveforms are captured on the YOKOGAWA WT1800 power analyser. All other results are captured in LabVIEW.

8.1.1 Two-level VSC modulation results

The two-level SVPWM technique has been implemented on the FPGA to control the two-level VSC. Experimental data shown in Figure 8-1 displays the converter voltage and current outputs using the developed modulation algorithm. The testing modulation index is set to 0.8, where the fundamental rms voltage values shown on the right validates the theoretical relationship presented in (98).

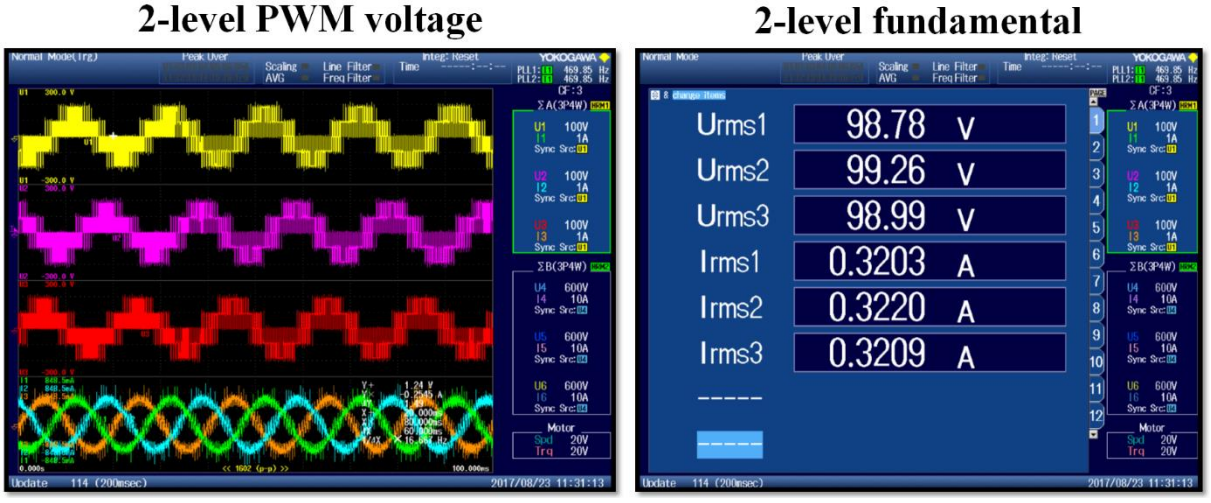

Figure 8-1: Two-level VSC modulation experimental results

8.1.2 Three-level VSC modulation results

The three-level SVPWM technique together with the DC-neutral point voltage balancing algorithm have been implemented on the FPGA to control the three-level VSC. Experimental data shown in Figure 8-2 displays three-level converter voltage and current output waveforms. The testing modulation index has been set to 0.4 then 0.8, where the fundamental rms voltage values corresponds to theoretical computation.

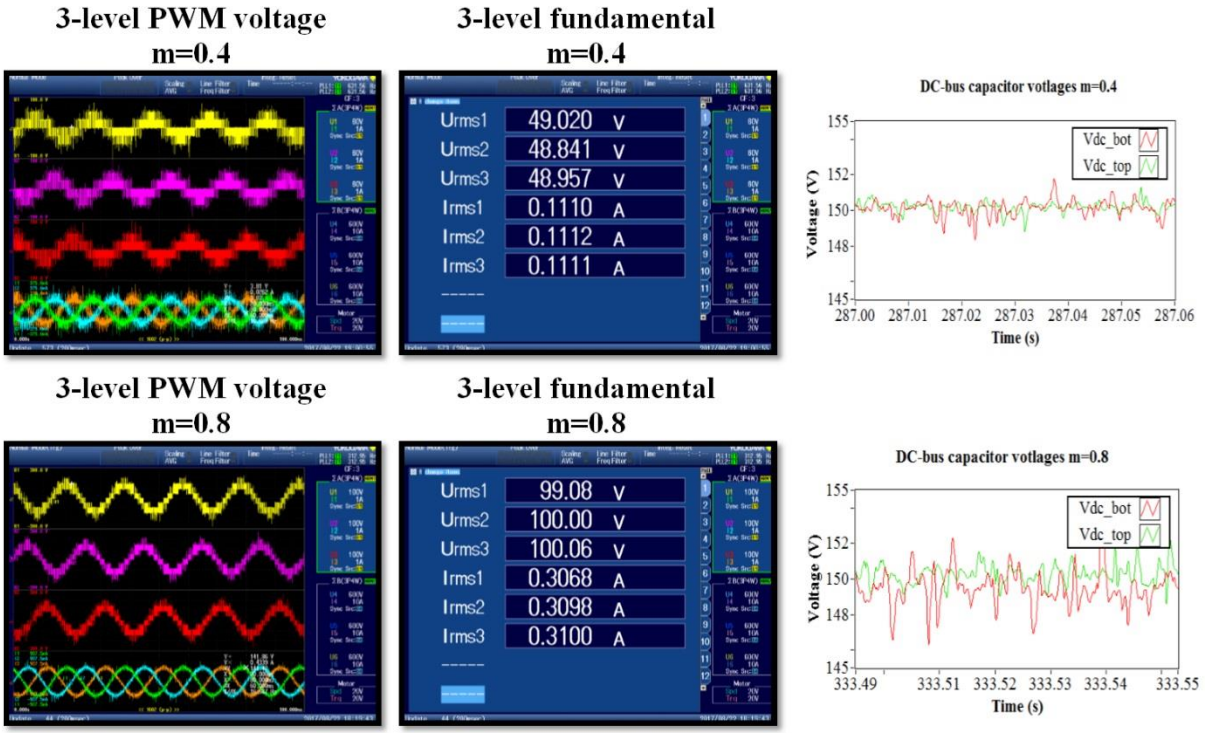

Figure 8-2: Three-level VSC modulation experimental results

The three-level VSC output waveforms here exhibit similar characteristics, for both modulation indices, when compared to the corresponding simulation results presented in subsection 6.5.2. The DC-bus capacitor voltages shows higher magnitude ripples due to measurement noises originating from the practical system. However, their balance is still achieved with loaded three-level VSC outputs.

As discussed previously, due to low modulation index operations inherent for the DFIG control, the two-level and three-level VSC's are chosen for RSC and GSC implementations respectively.

8.2 Experimental grid controller responses

The experimental tests for the GSC controller has been performed using similar operating conditions as the corresponding simulations presented in subsection 6.7.1. For the initial current controller test, the DC-bus voltage is fixed at $300V$ by using a single phase variac acting as a constant voltage source. All results obtained in this section are validated with respect to simulations performed for the GSC controller in subsection 6.7.1.

8.2.1 Current controller response

Experimental results shown in Figure 8-3 demonstrates the actual grid current control dynamics. These results are compared to simulated results shown in Figure 6-22.

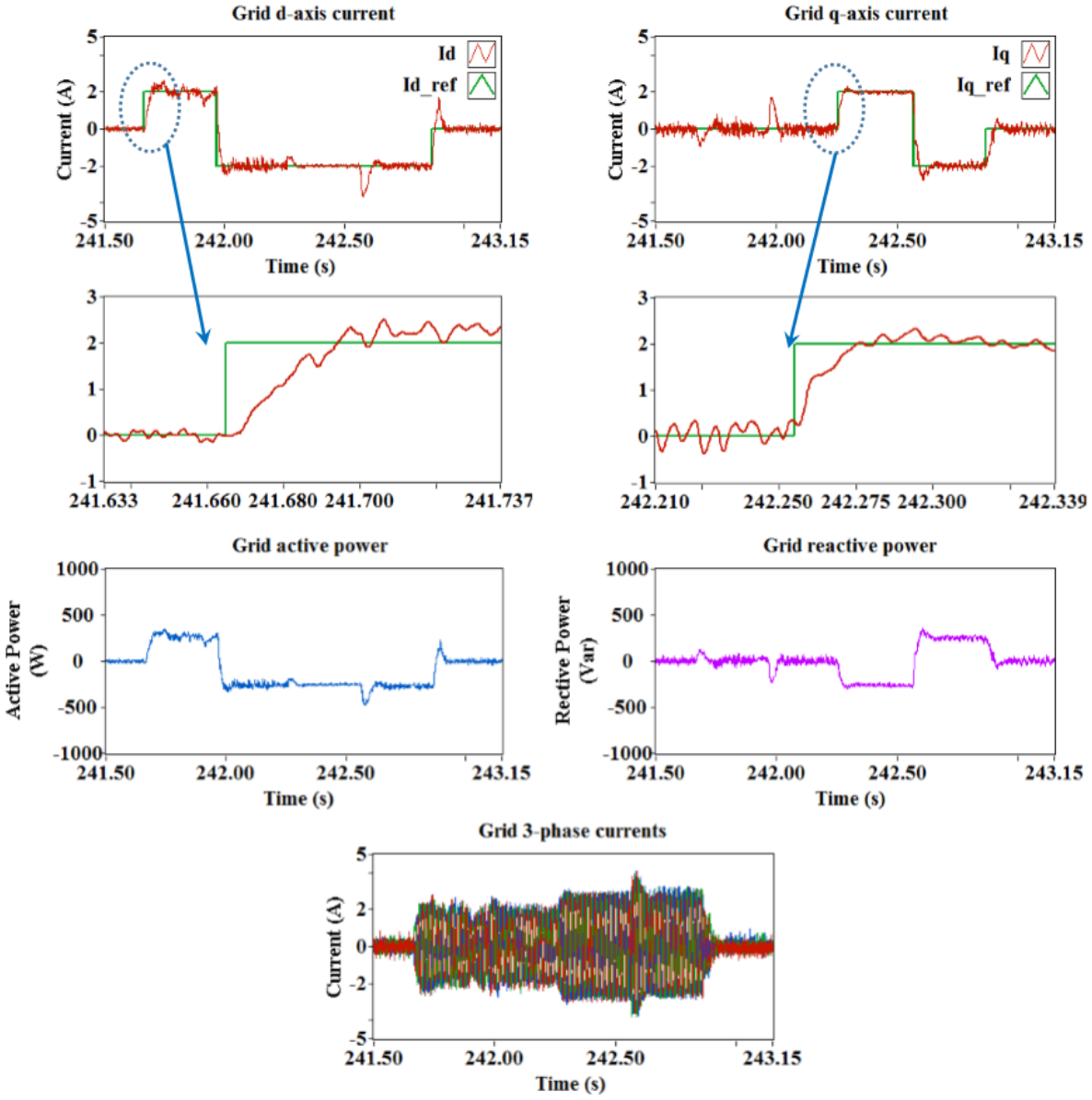

Figure 8-3: Experimental grid current control dynamics

The displayed experimental data exhibits some variations from the simulated grid current control dynamics. Small amount of overshoots can be observed in both dq-axis current step responses. This can be attributed to filter parameter variations due to changing currents, where the controller was designed assuming constant parameters. These response deviations do not pose as a serious issue as the controller gain and phase margins, shown in subsection 6.4.1, are sufficiently large to cater for minor parameter variations.

The settling times for the current steps are shown to be in the region of $0.02s$ which corresponds to the designed specification.

Experimental grid active and reactive power flow due to changes in the *dq* -axis currents shows identical dynamics as in the corresponding simulations. The changing polarities in the power flow demonstrates the three-level VSC operating in both rectifying and inverting mode. The three-phase grid current amplitude is equal to the *dq* -axis current values, which further validates the appropriateness of the grid current controller.

The correlation of simulated and experimental results indicates correctness in the filter modelling and its corresponding control design. Therefore stable operation for the grid current controller has been achieved.

8.2.2 DC-bus voltage controller response

Experimental results shown in Figure 8-4 demonstrates the actual DC-bus voltage control dynamics. These results are compared to simulated results shown in Figure 6-23.

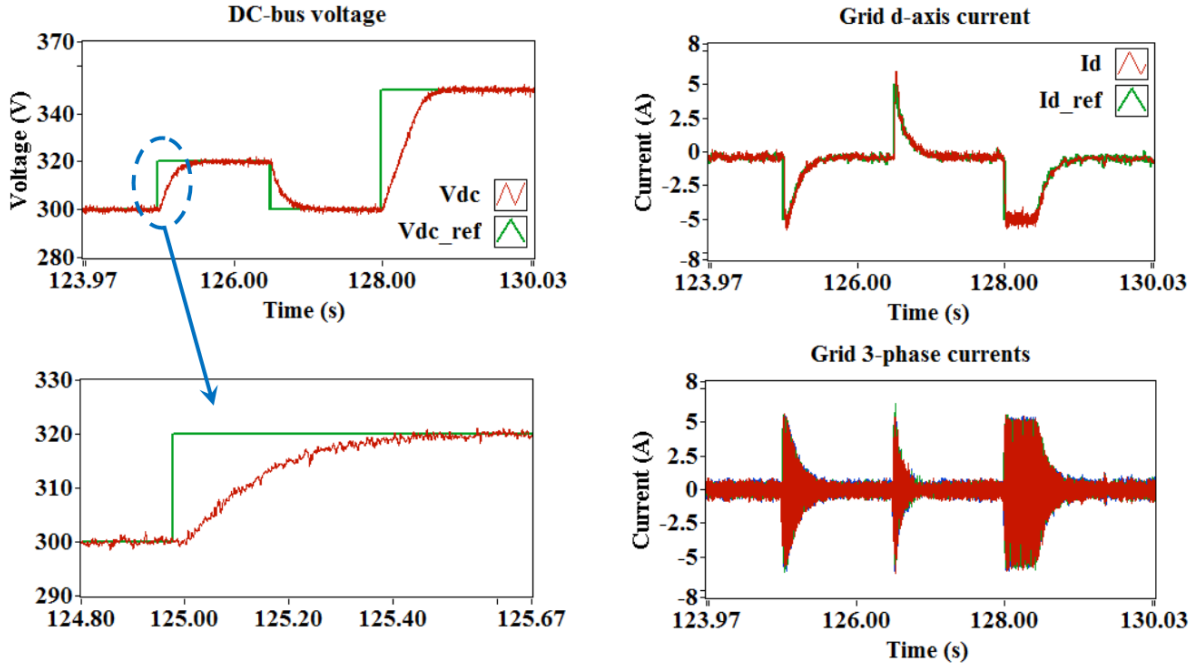

Figure 8-4: Experimental DC-bus voltage control dynamics

The displayed experimental data shows no significant variations from the simulated DC-bus voltage control dynamics. No overshoots are observed in the DC-bus voltage step responses. The settling times for the DC voltage steps are shown to be in the region of $0.5s$ which is close to the designed specification of $0.6s$. The longer settling time for a DC voltage step from $300V$ to $350V$ results from the d -axis current saturation at $t = 128s$, where the current limit is set to $5A$.

The deviation in current control dynamics, shown in the previous subsection, did not affect the DC voltage control dynamics. This is due to the much slower response time required for the outer voltage control loop compared to the inner current control loop.

The correlation of simulated and experimental results indicates correctness in the DC-link modelling and its corresponding control design. Therefore stable operation for the DC-bus voltage controller has been achieved.

8.3 Experimental implementation of DFIG soft synchronisation

The experimental tests for the DFIG soft synchronisation procedure has been performed using similar operating conditions as the corresponding simulations presented in section 6.6. All results obtained are then validated with respect to the simulation results.

8.3.1 DFIG synchronisation dynamics

Experimental results shown in Figure 8-5 demonstrates practical DFIG soft synchronisation dynamics. These results are compared to simulated results shown in Figure 6-20.

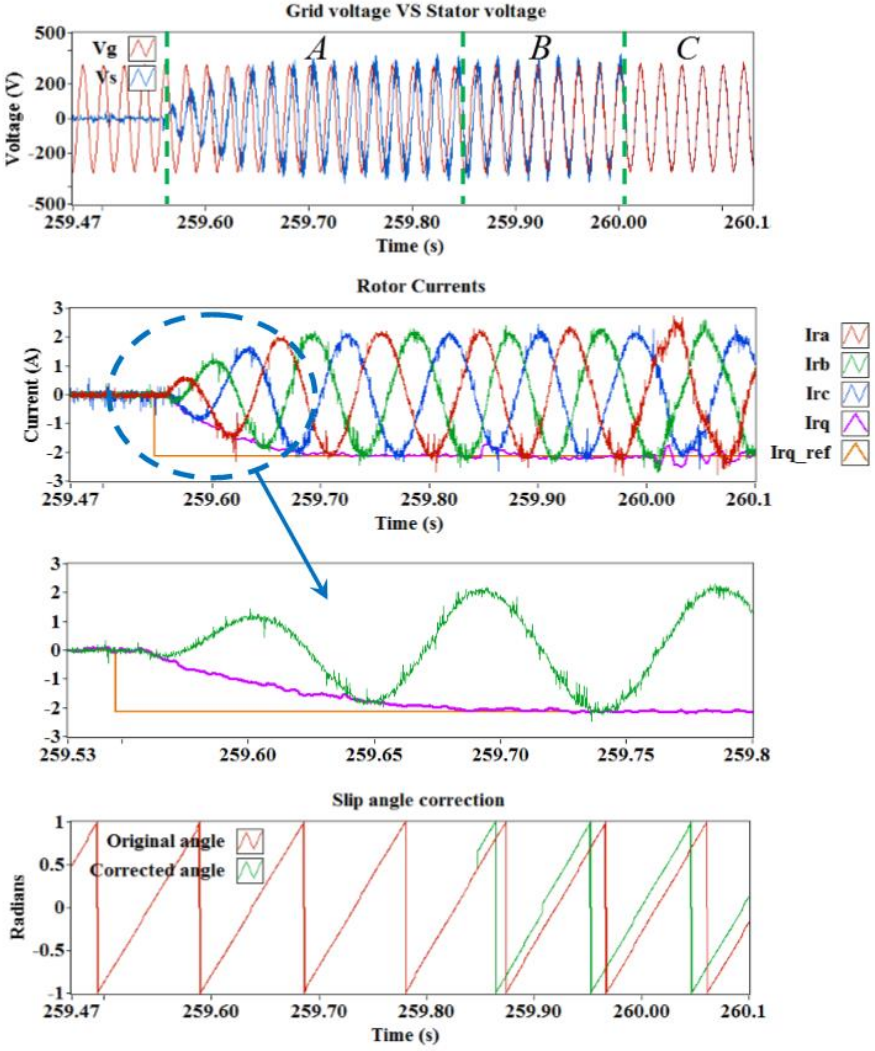

Figure 8-5: Experimental DFIG synchronization dynamics

For ease of presentation, the dynamics of the machine are separated into three operating regions with respect to the stator voltage:

A – Rotor current is set to the reference expressed in (109) and the stator voltage is induced accordingly to match grid voltage amplitude and frequency.

B – Rotor angle initial offset is approximated using (114) and added to the slip angle, whereas the stator voltage shifts to match grid voltage phase.

C – Stator contactor is closed and the machine is fully synchronised to the grid.

The above listed process coincides with the simulation results shown in Figure 6-20. The synchronisation rotor current step response is shown to have a settling time in the region of $0.16s$. This is close to the designed settling time of $0.18s$. The numerical set-point for the rotor q-axis current is approximately $-2A$, which is almost identical to the set-point shown in simulations. Therefore indicating that the machine has been correctly modelled and its parameters have been properly determined.

The slip angle correction is shown in Figure 8-5 where rotor angles were shown in simulated results. Although their respective frequencies are different, their dynamics are the same. It can be observed that the slip angle has its period synchronised to the rotor current. Note the angle shown here is in per unit with $\{-1:1\}$ representing a radian range of $\{-\pi:\pi\}$. This normalisation is done so as to reduce FPGA resource utilisation for the implementation of rotor angle related computations.

8.3.2 Stator current transients during synchronisation

The effect of feedforward error on stator current transients during synchronisation, discussed in section 5.2, is experimentally illustrated in Figure 8-6.

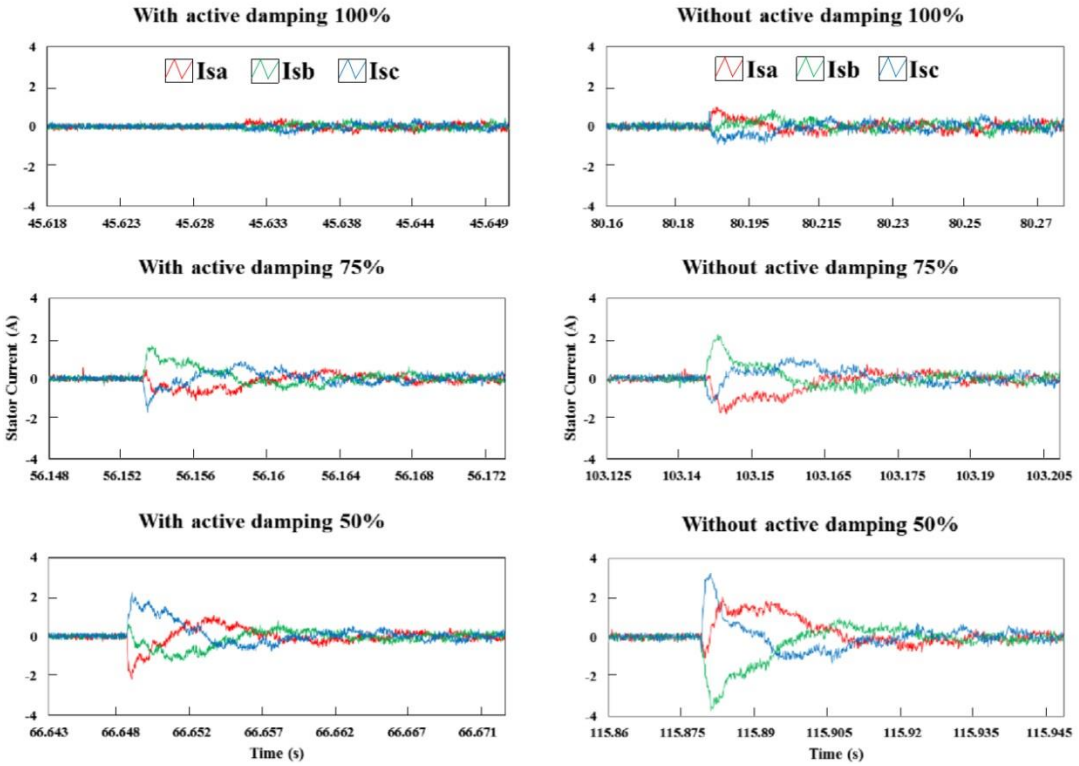

Figure 8-6: Stator current synchronization transients for IMC with and without active damping

These results are obtained for both IMC controllers with and without active damping to demonstrate the improved disturbance rejection using the first control methodology. The feedforward compensation for the rotor d-axis back-EMF component is artificially set, from 100% to 50% with 25% decrement in accuracy. Then the machine is synchronised to the grid with the existing feedforward error. It should be noted that the notion of 100% here is assumed to be accurate. However, this is more of a reference point as inaccuracy always exists in reality. The results shown in Figure 8-6 display higher stator current transients with increasing feedforward error. The resulting dynamics from both controllers are similar for lower error percentage, whaereas the active damping case displays lower peak current amplitudes and faster transient decay. In the case where the feedforward error is at 50%, the controller without active damping results in a peak curent amplitude of 3.8A which is 90% higher than that of the controller employing active damping.

8.4 Experimental DFIG controller responses

The experimental tests for the GSC controller has been performed using similar operating conditions as the corresponding simulations presented in subsection 6.7.2. Grid synchronisation for both WRIM stator and GSC are performed prior to implementing DFIG controller tests, and the DC-bus voltage is regulated

at $300V$. All results obtained in this section are validated with respect to simulations performed for the RSC controller in subsection 6.7.2.

8.4.1 Rotor current controller response

Experimental results shown in Figure 8-7 demonstrates the actual rotor current control dynamics. These results are compared to simulated results shown in Figure 6-25.

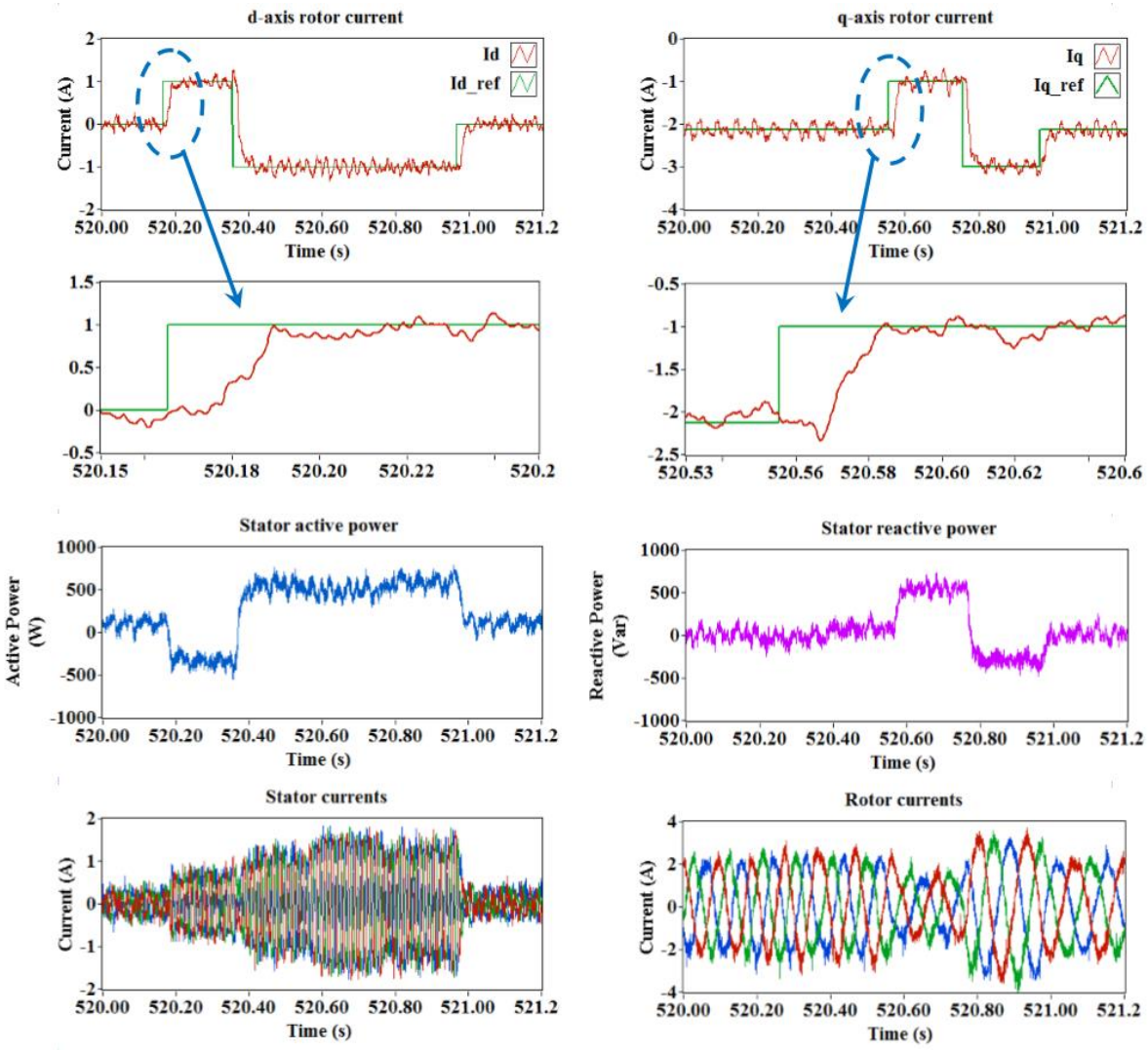

Figure 8-7: Experimental rotor current control dynamics

The displayed experimental data exhibits no significant variations from the simulated rotor current control dynamics. For the rotor current controller test, the machine speed is kept constant at 20% slip by the DC drive. However, due to the DC drive only being capable of two quadrant operations, excessive motoring torque generated by the DFIG may cause the rotor to accelerate dangerously. Therefore, rotor current step references are chosen more conservatively than that in the simulations.

No overshoots are observed in the rotor current step responses. The settling times for the current steps are shown to be in the region of $0.03s$ which corresponds to the designed specification.

Experimental stator active and reactive power flow due to changes in the dq -axis currents shows identical dynamics as in the corresponding simulations. The changing polarities in the active power flow indicates that the designed DFIG system can operate in motoring or generating modes. Three-phase stator and rotor currents shown in Figure 8-7 exhibits different frequencies which corresponds to the simulations as stator and rotor currents operate at grid and slip frequencies respectively.

The correlation of simulated and experimental results indicates correctness in the DFIG electrical circuit modelling and parameter determination. The controller design therefore produces stable operations for the DFIG rotor current control.

8.4.2 Speed controller response

Experimental results shown in Figure 8-8 demonstrates the actual DFIG speed control dynamics. These results are compared to simulated results shown in Figure 6-26.

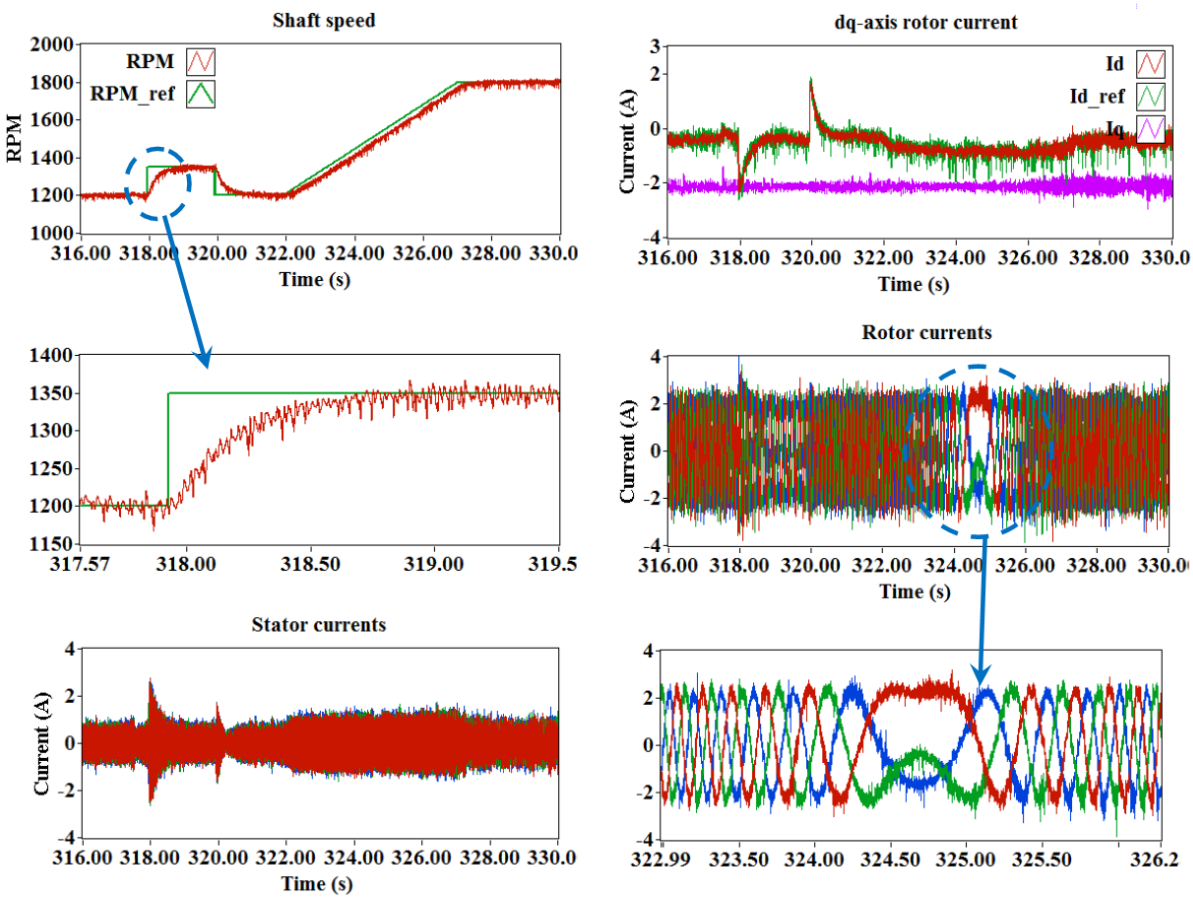

Figure 8-8: Experimental DFIG speed control dynamics

The displayed experimental data shows minor variations from the simulated DFIG speed control dynamics. Measurement noise can be observed in the captured speed waveform, which in turn causes high frequency fluctuations in the rotor d -axis current reference. However, the effect of the noise is not significant on the overall controller performance. This is the result of employing differential line driver and receiver for encoder feedback data transmission to the controller.

During the speed test, input power from the DC-machine is set to zero by limiting current output from the DC-drive, therefore all speed variations are performed through DFIG control. It can be seen that the rotor d -axis current has negative non-zero values during machine steady state conditions which implies power is drawn from the grid. This is required in order to overcome innate machine inertial and frictional load as well as drive train losses, so as to retain constant rotor speed.

No overshoots are observed in the DFIG speed step responses. The settling times for the speed steps are shown to be in the region of $1.12s$ which corresponds to the designed specification.

The rotor speed is accelerated from $1200rpm$ to $1800rpm$ between $t = 322s$ and $t = 327s$. The results shown in Figure 8-8 demonstrates that the experimental DFIG system is capable of a variable slip speed range of $\pm 20\%$. In addition, the rotor currents exhibits similar behaviours as the simulations where its frequency became zero as the machine approaches synchronous speed. It can also be seen that the rotor currents has reversed sequencing during super synchronous operations indicating a change in rotor power polarity.

The correlation of simulated and experimental results indicates correctness in the DFIG mechanical driver-train modelling and its inertia determination. The controller design therefore produces stable operations for the DFIG speed control.

8.5 Experimental DFIG system dynamics

The complete DFIG system dynamics are tested experimentally with reference to simulations shown in subsection 6.7.4. However, these tests are carried out slightly different to the simulations due to the practical limitation imposed by the DC-drive where manual control is required. Therefore, system dynamic tests are carried out in two parts:

- Input torque variation from the DC motor with machine speed regulated.
- Speed variation using DFIG control with input torque from the DC motor kept constant.

Experimental results for the constant DFIG speed test case are shown in Figure 8-9. These results are compared to simulated results shown in Figure 6-28.

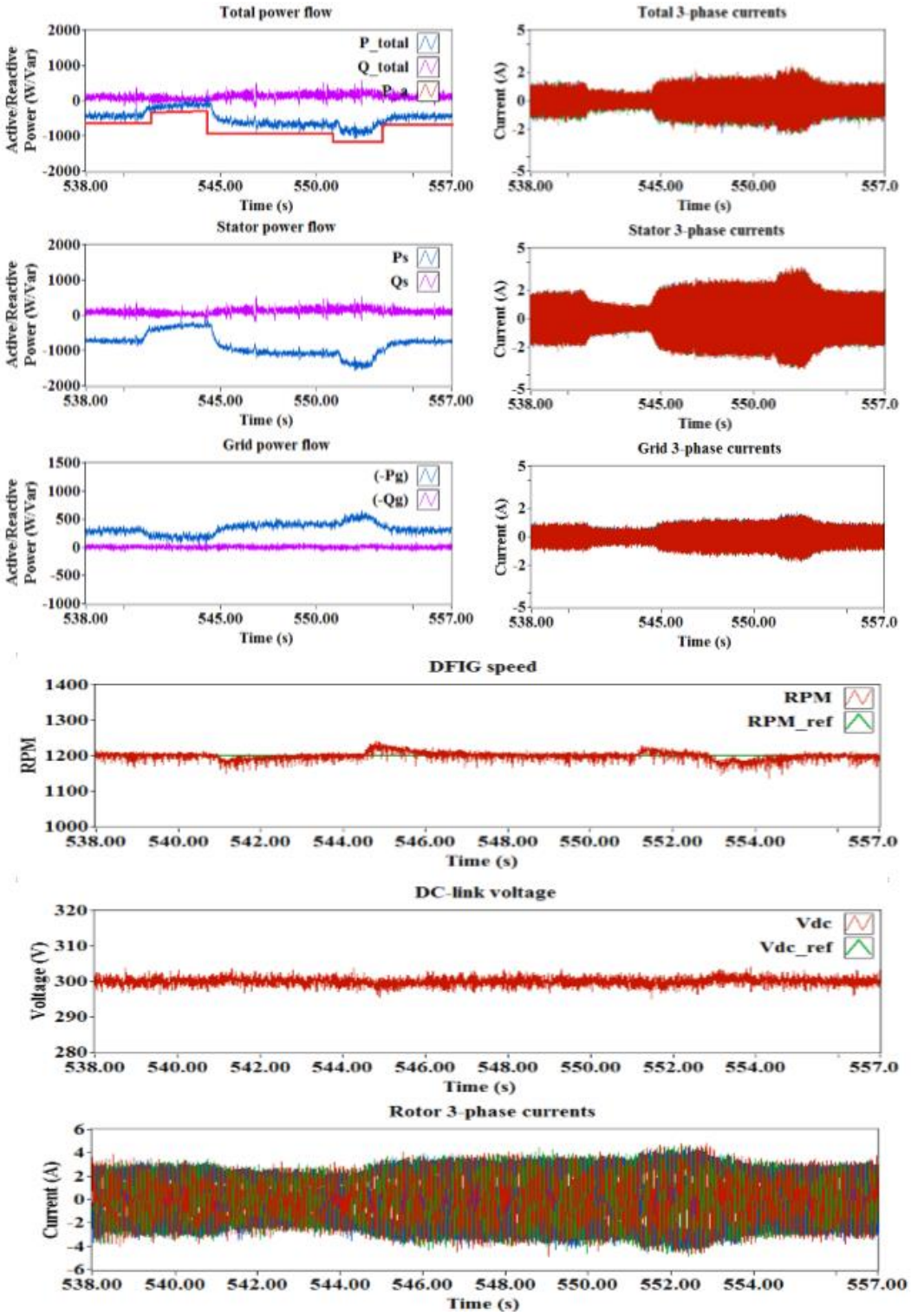

Figure 8-9: DFIG system operating at constant speed with input torque variations

The DFIG is initially operating at a constant speed of 1200 *rpm* corresponding to a 20% slip. The input torque is then varied by changing the armature voltage on the DC machine. The displayed experimental results shows similar dynamics when compared to the DFIG system simulations. Both machine speed and DC-link voltage are regulated at their respective set points with varying input torque. The grid active power is positive indicating directional flow from the grid, which is expected for DFIG sub synchronous

operations. The reference power shown is obtained by measuring DC-machine armature voltage and current. It can be seen that the total power generated by the DFIG is less than the DC input power. This can be attributed to losses that occur within the machines, converter and grid filter. In fact, the power transfer from the DFIG to the grid is shown to operate at an average of 72%.of the DC input power.

Experimental results for the constant input torque test case are shown in Figure 8-10. These results are compared to simulated results shown in Figure 6-28.

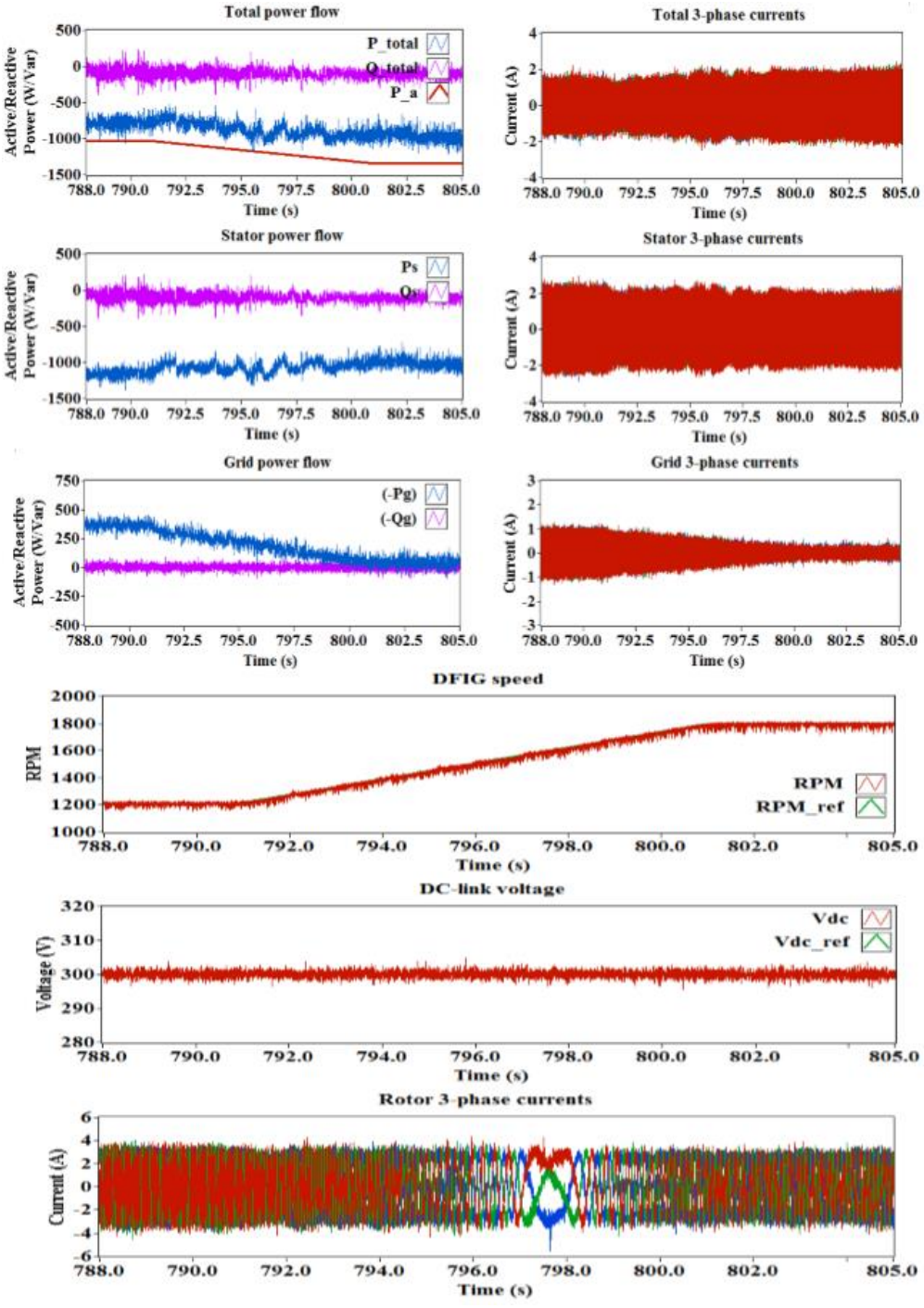

Figure 8-10: DFIG system operating at constant input torque with speed variations

In the second test case, the machine is accelerated from $1200\,rpm$ to $1800\,rpm$ corresponding to a slip range of 20% to -20%. The DC armature current is regulated at $4A$ which translates to a constant input torque of $6.3\,N.m$ from the DC machine. The displayed experimental results shows that total output power from the DFIG increases linearly with the speed which corresponds to the simulations. In addition power ripples can be observed when the machine is operating near the synchronous speed. In contrary to the simulations, the grid power did not change in polarity during DFIG super synchronous operations because of losses in the converters.

The above testing conditions for the developed DFIG system fully demonstrates its capability to operate in variable speed and power conditions. Although the system power efficiency can be improved, however, system dynamics has shown little variation from simulated behaviours. From both experimental and simulation results, it is shown that power contribution from the stator contain ripples when the DFIG is operating close to synchronous speed. Therefore prolonged synchronous operation for the DFIG should be avoided.

9. Conclusion and Recommendations

9.1 Conclusions

The design, analysis and testing of a grid-connected doubly fed induction generator system were presented in this dissertation. The following conclusions can be drawn based on the simulation and experimental results obtained:

- Models for various components of the DFIG system were accurately formulated. This is reflected in the similarities between simulated and experimental controller responses. It was shown that the control law developed for the DFIG system produces transient dynamics with no overshoots and settling times that are almost the same as design specifications.
- Space vector pulse width modulation algorithms for both two-level and three-level VSC's have been thoroughly investigated. The implementation for the three-level SVPWM on an FPGA based controller provides an indication that the algorithm adopted is indeed resource efficient. Furthermore, the DC-link voltage balancing for a three-level VSC was verified in simulation and laboratory testing. The correct operations of the system control also proves the appropriateness in the converter switching algorithms.
- A complete DFIG grid soft synchronisation algorithm developed was verified in simulation and by means of laboratory testing. The results shows very little stator current transients during the stator grid synchronisation instance. The issue of feedforward mismatch in the DFIG controller, specifically relating to synchronisation dynamics, has been investigated in simulation and experimentally. The results indicates that error in the feedforward compensation terms may produce large stator current transients during DFIG synchronisation. Further experimental testing has shown that the IMC controller design, implemented with active damping, could reduce these stator current transients assuming feedforward error exists.
- Simulation and experimental results are obtained using almost identical test conditions. The comparison between these results has shown remarkably similar characteristics. Therefore it can be concluded that the developed laboratory system has achieved correct operations, and that its dynamics are as predicted in theory.

9.2 Recommendations

Further improvements to the system and potential research that can be conducted using the testing rig are listed below:

- Bigger machines with ratings close to the converter ratings can be used.
- Proper filter design using more advanced topologies such as an LCL filter, can be implemented to improve GSC harmonic attenuation as well as reducing filter losses.

- A more advanced variable speed drive can be implemented with the DFIG system to emulate wind turbine operations.
- Abnormal grid conditions can be investigated using the developed system for DFIG fault ride-through studies. Grid unbalance compensation techniques such as dual vector control can be added to the existing control system.
- With the three-level VSC, research with respect to its effect within a DFIG system could prove to be interesting. The viability of using a three-level VSC for rotor-side control should be investigated. Attention should be paid to the effect of stator-rotor turns ratio on the RSC modulation index range.
- Different control strategies can be implemented on the DFIG system for comparative studies.

References

[1] "Renewables Gloabal Status Report, Renewable Energy Policy Network for the 21st Century (REN21)." [Online]. Available: http://www.ren21.net/gsr-2017/pages/summary/summary/. [Accessed: 08-Jun-2017].

[2] V. Yaramasu, B. Wu, P. C. Sen, S. Kouro, and M. Narimani, "High-power wind energy conversion systems: State-of-the-art and emerging technologies," *Proc. IEEE*, vol. 103, no. 5, pp. 740–788, 2015.

[3] "List of countries by carbon dioxide emissions," *wikipedia*, 2017. [Online]. Available: https://en.wikipedia.org/wiki/List_of_countries_by_carbon_dioxide_emissions. [Accessed: 08-Jun-2017].

[4] "REIPPP: All you need to know!," *Energy Intelligence*, 2016. [Online]. Available: http://www.energyintelligence.co.za/reippp-all-you-need-to-know/. [Accessed: 08-Jun-2017].

[5] "Integrated Resource Plan," *Department: Energy - Republic of South Africa*, 2016. [Online]. Available: http://www.energy.gov.za/IRP/2016/Draft-IRP-2016-Assumptions-Base-Case-and-Observations-Revision1.pdf. [Accessed: 08-Jun-2017].

[6] R. Flumerfelt and S. S. Wang, "Wind Power," *Access Science*, 2017. [Online]. Available: http://accessscience.com/content/746400. [Accessed: 08-Jun-2017].

[7] S. Müller, M. Deicke, and D. W., & Rik Doncker, "Doubly fed induction generator systems for wind turbines," *Ind. Appl. Mag. IEEE*, vol. 8, no. 3, pp. 26–33, 2002.

[8] F. Iov, M. Ciobotaru, and F. Blaabjerg, "Power electronics control of wind energy in distributed power systems," *2008 11th Int. Conf. Optim. Electr. Electron. Equip.*, pp. XXIX–XLIV, 2008.

[9] X. Jing, "Modeling and Control of a Doubly-Fed Induction Generator for Wind Turbine-Generator Systems," 2012.

[10] T. Lei, "Doubly-Fed Induction Generator Wind Turbine Modelling , Control and Reliability," University of Manchester, 2014.

[11] A. Petersson, "Analysis , Modeling and Control of Doubly-Fed Induction Generators for Wind Turbines," Chalmers University of Technology, 2003.

[12] G. Tapia, A. Tapia, and J. X. Ostolaza, "Two alternative modeling approaches for the evaluation of wind farm active and reactive power performances," *IEEE Trans. Energy Convers.*, vol. 21, no. 4, pp. 909–920, 2006.

[13] R. Pena, J. C. Clare, and G. M. Asher, "Doubly fed induction generator using back-to-back PWM converters and its application to variable-speed wind-energy generation," in *IEE Proceedings* -

Electric Power Applications, 1996, vol. 143, no. 3, p. 231.

[14] S. Breban, M. M. Radulescu, and B. Robyns, "Direct Active and Reactive Power Control of Variable-Speed Doubly-Fed Induction Generator on Micro-Hydro Energy Conversion System," *XIX Int. Conf. Electr. Mach.*, pp. 1–6, 2010.

[15] Z. Liu, O. a. Mohammed, and S. Liu, "A Novel Direct Torque Control of Doubly-Fed Induction Generator Used for Variable Speed Wind Power Generation," *2007 IEEE Power Eng. Soc. Gen. Meet.*, no. 1, pp. 1–6, 2007.

[16] R. Cárdenas, R. Peña, J. Proboste, G. Asher, and J. Clare, "Rotor current based MRAS observer for doubly-fed induction machines," *Electron. Lett.*, vol. 40, no. 12, p. 769, 2004.

[17] D. Zhi, L. Xu, and B. W. Williams, "Model-Based Predictive Direct Power Control of Doubly Fed Induction Generators," *IEEE Trans. Power Electron.*, vol. 25, no. 2, pp. 341–351, 2010.

[18] J. L. Elizondo *et al.*, "Model-based predictive rotor current control for grid synchronization of a DFIG driven by an indirect matrix converter," in *IEEE Journal of Emerging and Selected Topics in Power Electronics*, 2014, vol. 2, no. 4, pp. 715–726.

[19] H. Baesmat and M. Bodson, "Design of pole placement controllers for doubly-fed induction generators in the complex domain," *IEEE Power Energy Soc. Gen. Meet.*, vol. 2015–Septe, pp. 1–5, 2015.

[20] L. Harnefors and H.-P. Nee, "Model-based current control of AC machines using the internal model\ncontrol method," *IEEE Trans. Ind. Appl.*, vol. 34, no. 1, pp. 133–141, 1998.

[21] F. Briz del Blanco, M. W. Degner, and R. D. Lorenz, "Dynamic analysis of current regulators for AC motors using complex vectors," *IEEE Trans. Ind. Appl.*, vol. 35, no. 6, pp. 1424–1432, 1999.

[22] N. S. Nise, *Control Systems Engineering*, vol. 34, no. 8. 2005.

[23] D. Campos-Gaona, E. L. Moreno-Goytia, and O. Anaya-Lara, "Fault ride-through improvement of DFIG-WT by integrating a two-degrees-of-freedom internal model control," *IEEE Trans. Ind. Electron.*, vol. 60, no. 3, pp. 1133–1145, 2013.

[24] N. Moungkhum and W. Subsingha, "Voltage Control by DQ Frame Technique of SVPWM AC-DC Converter," *Energy Procedia*, vol. 34, pp. 341–350, 2013.

[25] K. V. Kumar, P. A. Michael, J. P. John, and S. S. Kumar, "Simulation and Comparison of Spwm and Svpwm Control for Three Phase Inverter," *ARPN J. Eng. Appl. Sci.*, vol. 5, no. 7, pp. 61–74, 2010.

[26] J. Pou, D. Boroyevich, and R. Pindado, "New feedforward space-vector PWM method to obtain balanced AC output voltages in a three-level neutral-point-clamped converter," *IEEE Trans. Ind.*

Electron., vol. 49, no. 5, pp. 1026–1034, 2002.

[27] G. Yuan, J. Chai, and Y. Li, "Vector Control and Sinchonization of Doubly Fed Induction Wind Generator System," *Power Electron. Motion Control Conf. 2004. IPEMC 2004. 4th Int.*, pp. 886–890, 2004.

[28] F. Blaabjerg, R. Teodorescu, M. Liserre, and A. V. Timbus, "Overview of control and grid synchronization for distributed power generation systems," *IEEE Trans. Ind. Electron.*, vol. 53, no. 5, pp. 1398–1409, 2006.

[29] Y. Lang, X. Zhang, D. Xu, S. R. Hadianamrei, and M. Hongfei, "Stagewise control of connecting DFIG to the grid," *IEEE Int. Symp. Ind. Electron.*, vol. 2, pp. 1129–1133, 2006.

[30] G. Iwanski and W. Koczara, "PLL grid synchronization of the standalone DFIG based wind turbine or rotary UPS," *EUROCON 2007 - Int. Conf. Comput. as a Tool*, pp. 2550–2555, 2007.

[31] G. Iwanski and W. Koczara, "Synchronization and mains outage detection for controlled grid connection of the wind driven variable speed power generation system," *2007 Int. Conf. Clean Electr. Power, ICCEP '07*, pp. 585–590, 2007.

[32] J. A. Cortajarena, J. De Marcos, P. Alvarez, F. J. Vicandi, and P. Alkorta, "Start up and control of a DFIG wind turbine test rig," *IECON Proc. (Industrial Electron. Conf.*, pp. 2030–2035, 2011.

[33] M. Dal, C. Simsek, M. C. Ceylan, and L. Akcil, "Characterisation of DFIG controlled by back to back coverters: Simulation and hardware implementation," *16th Int. Power Electron. Motion Control Conf. Expo. PEMC 2014*, no. 1, pp. 594–599, 2014.

[34] S. M. Muyeen *et al.*, "Comparative study on transient stability analysis of wind turbine generator system using different drive train models," in *IET Renewable Power Generation*, 2007, vol. 1, no. 2, pp. 131–141.

[35] L. A. C. Lopes, J. Lhuilier, A. Mukherjee, and M. F. Khokhar, "A wind turbine emulator that represents the dynamics of the wind turbine rotor and drive train," in *PESC Record - IEEE Annual Power Electronics Specialists Conference*, 2005, vol. 2005, pp. 2092–2097.

[36] J. M. Nye, J. G. de la Bat, M. A. Khan, and P. Barendse, "Design and implementation of a variable speed wind turbine emulator," in *2012 XXth International Conference on Electrical Machines*, 2012, pp. 2060–2065.

[37] D. S. L. Dolan and P. W. Lehn, "Simulation model of wind turbine 3p torque oscillations due to wind shear and tower shadow," *IEEE Trans. Energy Convers.*, vol. 21, no. 3, pp. 717–724, 2006.

[38] A. D. Hansen, F. Iov, F. Blaabjerg, and L. H. Hansen, "Review of Contemporary Wind Turbine Concepts and their Market Penetration," *Wind Eng.*, vol. 28, no. 3, pp. 247–263, 2004.

[39] a. Miller, E. Muljadi, and D. S. Zinger, "A variable speed wind turbine power control," *IEEE*

Trans. Energy Convers., vol. 12, no. 2, pp. 181–186, 1997.

[40] Y. Lei, A. Mullane, G. Lightbody, and R. Yacamini, "Modeling of the Wind Turbine With a Doubly Fed Induction Generator for Grid Integration Studies," *IEEE Trans. Energy Convers.*, vol. 21, no. 1, pp. 257–264, 2006.

[41] R. Ottersten, "On Control of Back-to-Back Converters and Sensorless Induction Machine Drives," 2003.

[42] A. Petersson, "Analysis , Modeling and Control of Doubly-Fed Induction Generators for Wind Turbines," 2005.

[43] W. Srirattanawichaikul, Y. Kumsuwan, S. Premrudeepreechacharn, and B. Wu, "A vector control of a grid-connected 3L-NPC-VSC with DFIG drives," *Electr. Eng. Comput. Telecommun. Inf. Technol. (ECTI-CON), 2010 Int. Conf.*, no. 1, pp. 1–5, 2010.

[44] S. Alepuz, S. Busquets-Monge, J. Bordonau, J. Gago, D. Gonz??lez, and J. Balcells, "Interfacing renewable energy sources to the utility grid using a three-level inverter," *IEEE Trans. Ind. Electron.*, vol. 53, no. 5, pp. 1504–1511, 2006.

[45] S. Bezkowski, T. Slivsgaard, G. Fluriach, P. Aitor, and G. Matias, "Control of grid side inverter for wind turbine," AALBORG University, 2010.

[46] A. Reznik, M. G. Simoes, A. Al-Durra, and S. M. Muyeen, "LCL Filter design and performance analysis for grid-interconnected systems," *IEEE Trans. Ind. Appl.*, vol. 50, no. 2, pp. 1225–1232, 2014.

[47] S. G. Parker, B. P. McGrath, and D. G. Holmes, "Regions of active damping control for LCL filters," *IEEE Trans. Ind. Appl.*, vol. 50, no. 1, pp. 424–432, 2014.

[48] J. G. Slootweg, S. W. H. de Haan, H. Polinder, and W. L. Kling, "General model for representing variable speed wind turbines in power system dynamics simulations," *IEEE Trans. Power Syst.*, vol. 18, no. 1, pp. 144–151, 2003.

[49] P. M. Anderson and A. Bose, "Stability Simulation Of Wind Turbine Systems," *IEEE Trans. Power Appar. Syst.*, vol. PAS-102, no. 12, pp. 3791–3795, 1983.

[50] J. F. Manwell, J. G. McGowan, and A. L. Rogers, *Wind energy explained: theory, design and application*. 2009.

[51] P. Sen, *Principles of Electric Machines and Power Electronics*, Third Edit. Wiley, 2014.

[52] P. S. Barendse, "Design and Implementation of Variable Speed Induction Generator For Wind Energy System," University of Cape Town, 2004.

[53] J. B. Ekanayake, L. Holdsworth, and N. Jenkins, "Dynamic modeling of doubly fed induction

generator wind turbines," *IEEE Trans. Power Syst.*, vol. 18, no. 2, pp. 803–809, 2003.

[54] B. Wu, Y. Lang, N. Zargari, and K. Samir, *Power Conversion and Control of Wind Energy Systems*. John Wiley & Sons.

[55] R. Odisha, "Modeling and Simulation of AC / DC Grid Side Voltage Source Converter Used in Wind Power Generation System," in *International Conference on Circuit, Power and Computing Technologies*, 2014, no. 1, pp. 484–489.

[56] G. S. Virk, "Robust process control.," *Chemical Engineering Science*, vol. 45, no. 4. Prentice-Hall, Inc., New Jersey, p. 1149, 1990.

[57] K. Hentabli, M. E. H. Benbouzid, and D. Pinchon, "CGPC with internal model structure: Application to induction motor control," *IEEE Conf. Control Appl. - Proc.*, no. 3, pp. 235–237, 1997.

[58] J. J. Craig, "Introduction to Robotics: Mechanics and Control 3rd," *Prentice Hall*, vol. 1, no. 3. p. 408, 2004.

[59] A. Khan, "Development of a Grid Emulator for Network Integration Studies," University of Cape Tonw, 2014.

[60] G. Fluriach Pla and A. Gómez Matias, "Control of grid side inverter for wind turbine," 2010.

[61] S. Li, R. Challoo, and M. J. Nemmers, "Comparative study of DFIG power control using stator-voltage and stator-flux oriented frames," in *2009 IEEE Power and Energy Society General Meeting, PES '09*, 2009.

[62] N. Celanovic and D. Boroyevich, "A fast space-vector modulation algorithm for multilevel three-phase converters," *IEEE Trans. Ind. Appl.*, vol. 37, no. 2, pp. 637–641, 2001.

[63] N. Celanovic, W. T. Baumann, F. C. Lee, and D. J. Nelson, "Space Vector Modulation and Control of Multilevel Converters," *Pace Pacing Clin. Electrophysiol.*, 2000.

[64] J. Pou *et al.*, "Fast-processing modulation strategy for the neutral-point-champed converter with total elimination of low-frequency voltage oscillations in the neutral point," *IEEE Trans. Ind. Electron.*, vol. 54, no. 4, pp. 2288–2294, 2007.

[65] G. Tapia, G. Santamaría, M. Telleria, and A. Susperregui, "Methodology for smooth connection of doubly fed induction generators to the grid," *IEEE Trans. Energy Convers.*, vol. 24, no. 4, pp. 959–971, 2009.

[66] I. D. Ilina, "Experimental Determination of Moment to Inertia and Mechanical Losses vs. Speed, in Electrical Machines," *7th Int. Symp. Adv. Top. Electr. Eng.*, no. 3, pp. 1–4, 2011.

[67] R. Babau, I. Boldea, T. J. E. Miller, and N. Muntean, "Complete parameter identification of large

induction machines from no-load acceleration-deceleration tests," *IEEE Trans. Ind. Electron.*, vol. 54, no. 4, pp. 1962–1972, 2007.

Appendix A

➢ PXI controller datasheets

PXIe-6363: http://www.ni.com/datasheet/pdf/en/ds-151

PXI-7813R: http://www.ni.com/datasheet/pdf/en/ds-98

➢ Two-level and three-level VSC related datasheets

SkimMLI200: https://www.semikron.com/dl/servicesupport/downloads/download/semikron-datasheet-skim201mli12e4-23918890/

SKHI22BR: https://www.semikron.com/dl/servicesupport/downloads/download/semikron-datasheet-skhi-22-a-b-r-l5012521/

MN74HC08: https://industrial.panasonic.com/content/data/SC/ds/ds4/MN74HC08__E_discon.pdf

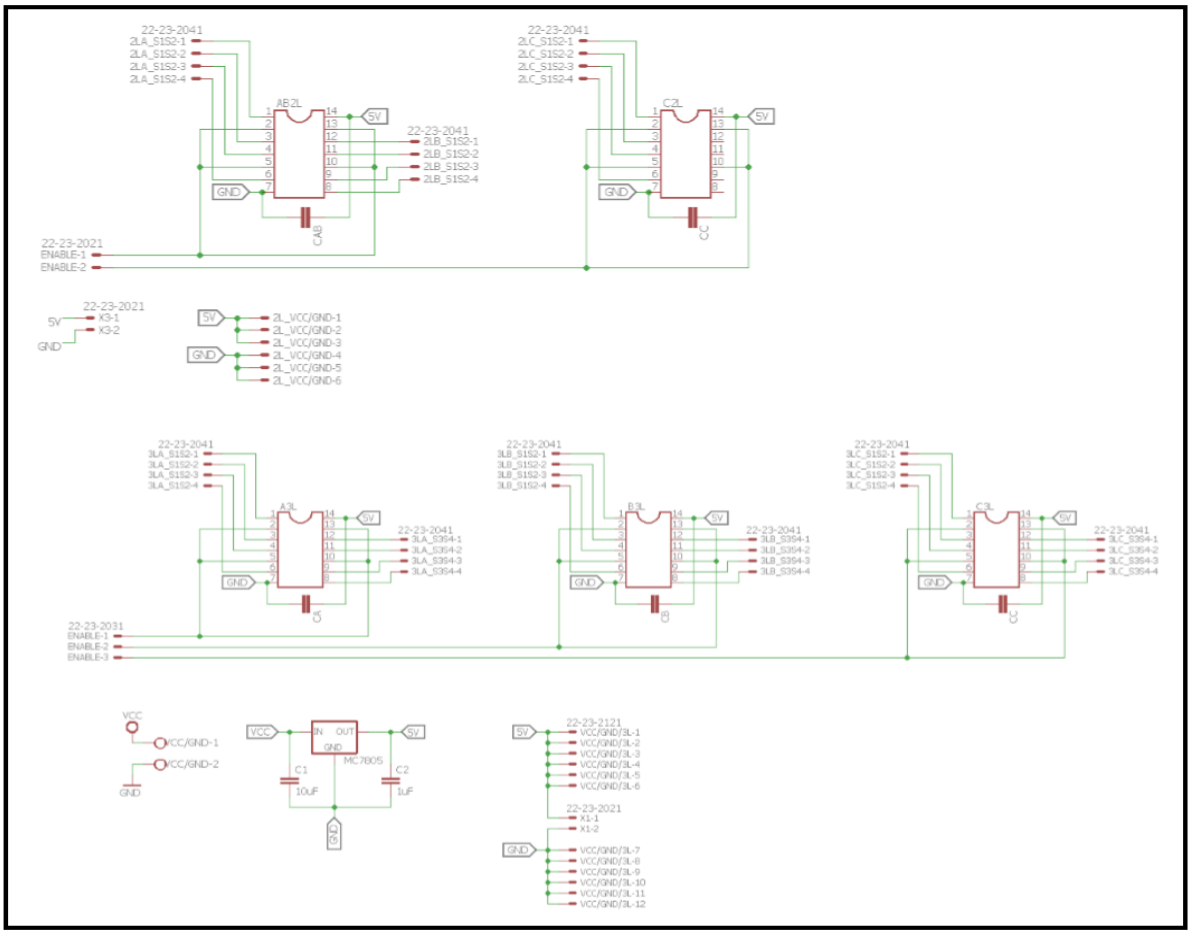

Figure A: Schematic diagram for FPGA level shifter

➢ Current and voltage transducers

LEM LV 25-P: http://www.lem.com/docs/products/lv_25-p.pdf

LEM LA 100-A: http://www.lem.com/docs/products/la_100-p_sp13.pdf

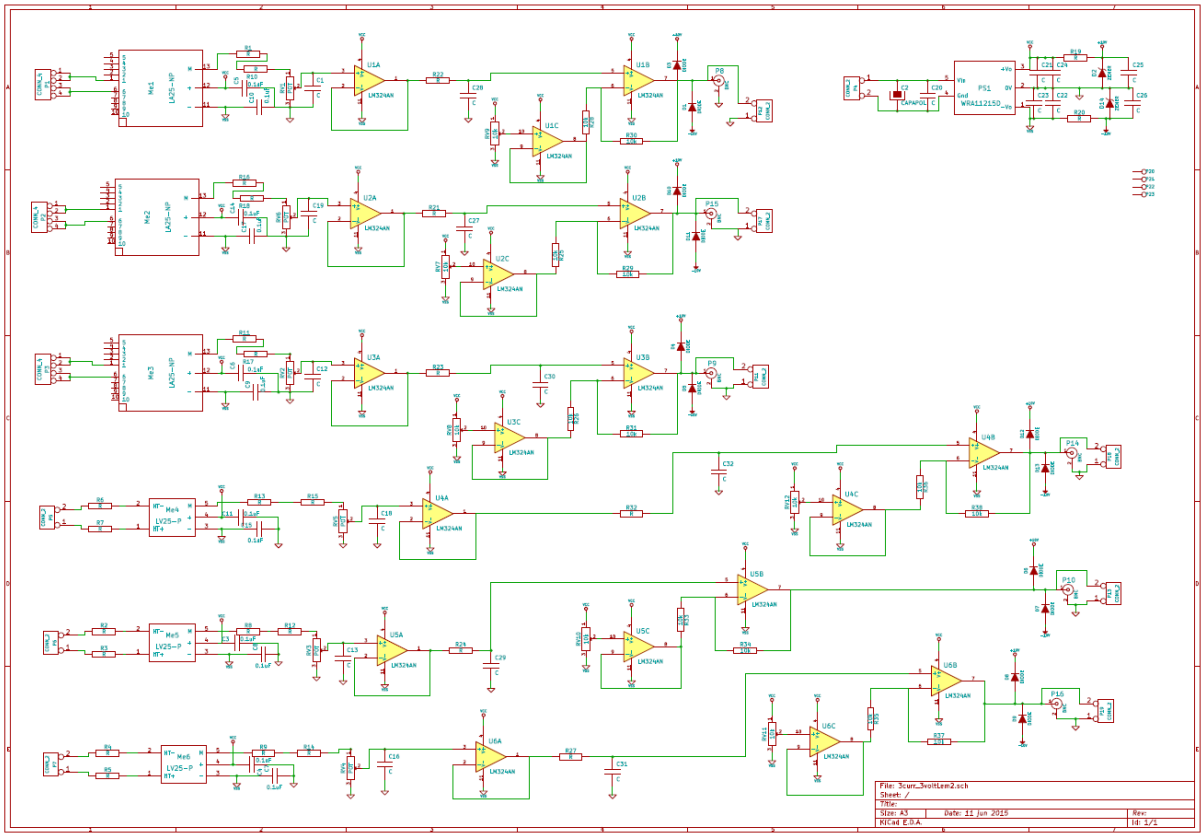

Figure B: Schematic diagram for LEM integrated circuits

➢ Incremental encoder

RS58-0/1000: http://docs-europe.electrocomponents.com/webdocs/002f/0900766b8002f9dc.pdf

AM26LS31CN: http://www.ti.com/lit/ds/symlink/am26ls31.pdf

AM26LS31ACN: http://pdf1.alldatasheet.com/datasheet-pdf/view/176863/TI/AM26LS31.html